UNIVERSITY OF OKLAHOMA

GRADUATE COLLEGE

PROBING FLAVOR CHANGING NEUTRAL HIGGS INTERACTIONS AT LHC AND FUTURE HADRON COLLIDERS

A DISSERTATION

SUBMITTED TO THE GRADUATE FACULTY

in partial fulfillment of the requirements for the

Degree of

DOCTOR OF PHILOSOPHY

By

RISHABH JAIN
Norman, Oklahoma
2020

Downloaded from SHAREOK. Persistent Handle URL: https://hdl.handle.net/11244/324838

PROBING FLAVOR CHANGING NEUTRAL HIGGS INTERACTIONS
AT LHC AND FUTURE HADRON COLLIDERS

A DISSERTATION APPROVED FOR THE
HOMER L. DODGE DEPARTMENT OF PHYSICS AND ASTRONOMY

BY THE COMMITTEE CONSISTING OF

Dr. Chung Kao, Chair

Dr. Nikola Petrov

Dr. Brad Abbott

Dr. Howard Baer

Dr. Kieran Mullen

©Copyright by Rishabh Jain, 2020

All Rights Reserved

Acknowledgement

When I started my graduate study at the University of Oklahoma, I was not sure about my capabilities as a researcher. But over the years, with the help from several significant people, I have become more confident and skillful in physics research and I would like to thank them all.

First, I would like to thank my advisor Prof. Chung Kao. This work wouldn't have been possible without his guidance. He has been extremely patient with me and has helped me in every way possible throughout my stay at The University of Oklahoma. I thank my committee members, Prof. Brad Abbott, Prof. Howard Baer, Prof. Nikola Petrov, and Prof. Kieran Mullen, for their valuable inputs and suggestions. Special thanks go to Prof. Kieran Mullen for every advice he has given me.

I would also like to thank all of my collaborators. Prof. Amarjit Soni, I had some outstanding conversations with him for one of our projects. Dr. Masaya Kohda, his valuable comments and advice has helped me improve my critical thinking. Special thanks go to Prof. George Wei-Shu Hou, not only for giving me a golden opportunity to work with him as a postdoctoral research associate, but also for his significant help in understanding particle theory.

I want to thank our department chair, Prof. Phillip Gutierrez, for collaboration in a physics project. He has given me some great insight in collider phenomenology with Monte Carlo simulations.

As a high energy theorists, it is also essential to expand our knowledge beyond the realms of your research area. I want to thank Prof. Kuver Sinha and Prof. John Stupak, for starting the journal club, which has given us a platform to expand our knowledge and improve our communication skills. I thank them for inviting me to work on an exciting project with the detector MATHUSLA; I hope we can

finish this year.

In addition, I want to thank all the office staff, Cindy, Joyce, Ashley, Debi, and Amanda, to run the office smoothly and keep our life simple. I would also like to thank Abby Young and Jessica Reynolds for helping me clear the steps needed to make progress in the graduate program.

Occasionally, graduate student life might be callous for all of us; we need people to help us get through tough times. I want to thank my wife; she has been a great support to me. She has encouraged me, given me advice, and has kept me calm. I am grateful to all of my Indian friends: Soumya, Hora, Shivani, Dibyashree, Varsha, Gaurav, Mahesh, Saloni, Diken, Anvit, and Saikat, for all the parties and trips, that has helped me recharge several times. I would also like to thank additional friends: Dylan, Daniel, Huaike, Akbar, Shahram, Delaram, Javad, Robert, and Alex. I will miss those tea-time conversions that I had with all of them. I cannot end this without giving thanks to my big brother Brent Mccoy; he has helped me to go through the first few years of my Ph.D. I learned a lot from him. Thank you to Baris Altunkaynak, our former post-doc, for developing all of the essential codes and models used in this work.

In the end, I want to thank my family and my in-laws back in India, for supporting me and showing faith in me. I can go on for 100 pages, and it will still not be enough to cover all the people, so thank you again. I look forward to seeing you all in the future.

Table of Contents

1 Introduction **1**

1.1 Structure of Standard Model 1

1.1.1 Leptons 3

1.1.2 Antiparticles 5

1.1.3 Quarks, Meson, and Baryons 6

1.1.4 Vector Bosons 9

1.1.5 Quantum Electrodynamics (QED) 10

1.1.6 Quantum Chromodynamics (QCD) 11

1.1.7 Electroweak Interactions and Higgs Mechanism 13

1.1.8 Flavor Symmetry and GIM Mechanism 23

1.1.9 Recent Flavor Anomalies 25

1.2 Introduction to General Two Higgs Doublet Model 27

1.2.1 Modified Higgs Potential 28

1.2.2 Corrections to the Yukawa Sector and FCNH 32

2 Discovery Channels and Analysis Strategies **35**

2.1 Discovery Channels 35

2.1.1 Motivation for $\phi^0 \to \tau\mu$ 35

2.1.2 Motivation for $t \to ch^0$ 36

2.2 Analysis Tools and Strategies 39

2.2.1 Integration Method 39

2.2.2 Phase Space Integration and Event Generation 41

2.2.3 Traditional Cut Based Optimization 47

2.2.4 Machine Learning with Advantages and Improvements . . 49

3 Probing Flavor Changing Neutral Current with Leptons 52

3.1 Constraints on Relevant Parameters 52

3.2 Higgs Signal and Physics Background 57

3.2.1 Higgs Signal 58

3.2.2 Standard Model Backgrounds 60

3.2.3 Realistic Acceptance Cuts 61

3.3 Discovery Potential 63

3.3.1 Discovery Reach for Pseudo-scalar 63

3.3.2 Discovery Reach for Heavy Scalar 65

4 Probing Flavor Changing Neutral Current with Charm and Top 71

4.1 $h^0 \to W^+W^-$ 71

4.1.1 The Higgs Signal and Physics Background 71

4.1.2 The Higgs Signal in Top Decay 72

4.1.3 The Physics Background 76

4.1.4 Mass Reconstruction 77

4.1.5 Realistic Acceptance Cuts 80

4.1.6 Discovery Potential at the LHC 80

4.2 $h^0 \to \tau^+\tau^-$ 86

4.2.1 Higgs Signal 86

4.2.2 The Physics Background 87

4.2.3 Realistic Acceptance Cuts 88

4.2.4 Mass Reconstruction 89

4.2.5 Important Mass Cuts 92

4.2.6 Discovery Potential 94

4.3 Combined Estimates at Parton Level 98

5 Conclusion and Future Work 101

REFERENCES **106**

Appendix A **116**

Appendix B **119**

List of Figures

1.1 Standard Model (by Eric Drexler, Wikipedia) 2

1.2 Higgs potential with (a) $\mu^2 > 0$, and, (b) $\mu^2 < 0$. 19

1.3 Higgs potential after symmetry breaking. 20

1.4 Two contributions to $K_L^0 \to \mu^+\mu^-$. 24

1.5 One loop contributions for $t \to ch^0$ decay. 25

1.6 Higgs potential in gTHDM, with $m_H = m_A = m_{H^\pm} = 300$ GeV,$\cos\beta - \alpha = 0.1$, and $\lambda_6 = \lambda_7 = 0$ is shown in (a) and the Higgs potential when ϕ_2^0 is very close to 0 is shown in (b). 31

2.1 The predicted values for $R(D)$ and $R(D*)$ from 2HDM-II (right) and (left) from 2HDM-III for different values of $r_\tau = |\rho^{\mu\tau}/\rho^{e\tau}| = 1.6$(orange triangle),2(cyan quadrangle) 2.7(open pink quadrangle) and 4(green$\times$) Iguro. et. al (Nucl. Phys. B. 2017.10.014). 37

2.2 Impact of ρ_{tt} and ρ_{tc} on the ratio of Y_B/Y_B^{obs} Fuyuto. et. al (Phys. Lett. B. 2017.11.073). 39

2.3 Invariant mass distribution for the data (points with error bars) shown together with the simultaneous fit result to $h^0 \to ZZ^* \to 4\ell$ candidates (continuous line). The background component of the fit is also shown (filled area). Aaboud. et al (ATLAS-Collaboration: Phys. Lett. B .2018.07.050). 47

2.4 Mass distributions for $pp \to H^0, A^0 \to 4\ell + 2\tilde{Z}_1^0$ and the most dominant backgrounds. 48

3.1 Constraints on the $(\rho_{tt}, \rho_{\tau\mu})$ plane with $\rho_{\mu\tau} = \rho_{\tau\mu}$ for (a) $M_{H^0} = M_{A^0} = M_{H^\pm} = 150$ GeV and (b) 300 GeV, both assuming $\cos(\beta - \alpha) = 0.1$, $\rho_{\tau\tau} = \kappa_\tau$ and $\rho_{bb} = \kappa_b$. Dashed lines indicate $\mathcal{B}(\tau \to \mu\gamma) = 1 \times 10^{-9}$ for a future sensitivity. See the main text for details. 56

3.2 Branching ratios for $H^0 \to XX$ w.r.t M_H. Including all the dominant two body decays, with $\rho_{\tau\mu} = 0.01$. We have set $\lambda_5 = 0$ and $1 \leq \tan\beta \leq 10$. 58

3.3 Branching Ratios for A $\to$ all dominant two body decays w.r.t M_A, setting $\rho_{\tau\mu} = 0.01$. 58

3.4 Cross-section of backgrounds as a function of M_H at $\sqrt{s} = 14$ TeV. 63

3.5 Discovery range at the LHC and future hadron colliders with $\sqrt{s} =$ 14 TeV (green dark shading), 27 TeV (intermediate shading) and 100 TeV (light shading) for $pp \to A^0 \to \tau\mu + X$ in the $(M_A, \tilde{\rho}_{\tau\mu})$ plane. We require 5σ significance for 3000fb^{-1}. Top (bottom) row is for leptonic (hadronic) τ-lepton decay for $\tilde{\rho}_{tc} = 0.1$[(a) and (c)] and $\tilde{\rho}_{tc} = 0.5$[(b)and(d)]. 65

3.6 Cross-section (in fb) of $pp \to H^0 \to \tau\mu \to e\mu + X$ (blue solid) at (a) $\sqrt{s} = 14$ TeV, (b) 27 TeV and (c) 100 TeV, as a function of λ_5 with $M_H = 300$ GeV, $\rho_{\tau\mu} = 0.01$, $\tan\beta = 1$, $\cos(\beta - \alpha)$, and $\tilde{\rho}_{tc} = 0.1$. Also shown are the total background (maroon dotdash), the predominant background from $pp \to W^+W^- + X$ (magenta dash), and the 5σ signal significance (green dash) with integrated luminosity $\mathcal{L} = 3000\ fb^{-1}$ or $300\ fb^{-1}$. We also present results for (d) $\tilde{\rho}_{tc} = 0.5$ at $\sqrt{s} = 100$ TeV. 66

3.7 Discovery regions at the LHC and future hadron colliders with the $\sqrt{s} = 14$ TeV (green dark shading), 27 TeV (intermediate shading) and 100 TeV (light shading) for $pp \to H^0 \to \tau\mu + X$ in the $(M_H, \tilde{\rho}_{\tau\mu})$ plane. We require at least 5σ significance for 3000fb^{-1}. Top (bottom) row is for leptonic (hadronic) τ-lepton decay with $\lambda_5 = -1$[(a) and (c)] and $\lambda_5 = 0$[(b) and (d)]. 68

4.1 Feynman diagram for $pp \to t\bar{t} \to bjj\, ch^0 + X \to bjj\, c\ell^+\ell^-\nu\nu X$, where $\ell = e$ or μ. 72

4.2 Invariant mass distributions ($d\sigma/dM$) of $j_1 j_2$ (green dotdash), and $bj_1 j_2$ (blue solid), for the Higgs signal in pp collisions, $d\sigma/dM(pp \to t\bar{t} \to tch^0 \to tcWW \to bjjc\ell^+\ell^- + \not{E}_T + X$ (fb/GeV), with basic cuts defined in Eq 4.17. Also shown are the invariant mass distributions $d\sigma/dM_{j_1 j_2}$ (magenta dot) and $d\sigma/dM_{bj_1 j_2}$ (red dash) for the dominant physics background from $t\bar{t}jj$. 78

4.3 Cluster transverse mass distributions ($d\sigma/dM_T$) of $\ell^+\ell^-$ (green dotdash) and $c\ell^+\ell^-$ (blue solid) for the Higgs signal in pp collisions, $d\sigma/dM_T(pp \to t\bar{t} \to tch^0 \to tcWW \to bjjc\ell^+\ell^- + \not{E}_T + X$ (fb/GeV), with basic cuts defined in Eq 4.17, as well as $|M_{jj} - m_W| \leq 0.15 \times m_W$ and $|M_{bjj} - m_t| \leq 0.20 \times m_t$. Also shown are the cluster transverse mass distributions $d\sigma/dM_T(\ell\ell, \not{E}_T)$ (magenta dot) and $d\sigma/dM_T(c\ell\ell, \not{E}_T)$ (red dash) for the dominant physics background from $t\bar{t}jj$. 79

4.4 The cross-section in fb of $pp \to t\bar{t} \to tch^0 \to bjjc\ell^+\ell^- + \not{E}_T + X$ at $\sqrt{s} = 13$ TeV and 14 TeV as a function of $\tilde{\rho}_{tc}$, along with total (magenta dotdash) and most dominant (red dash) background after applying all the cuts, tagging and mistagging efficiencies, and higher order QCD corrections. The blue dash line and green dash line shows the minimum cross-section needed for 5σ significance at $\mathcal{L} = 36fb^{-1}$ and $3000fb^{-1}$ respectively for the center of mass energy of 13 TeV. Where as for 14 TeV, we present $\mathcal{L} = 3ab^{-1}$ (green dash) only. The ATLAS-Limit-2019 is shown as a black dash vertical line. 81

4.5 Similar to Fig. **4.4**, but for (a) $\sqrt{s} = 27$ TeV, and (b) 100 TeV. . 82

4.6 The 5σ discovery contours at the LHC in the plane of $[\cos(\beta-\alpha), \tilde{\rho}_{tc}]$ for (a) $\sqrt{s} = 13$ TeV and (b) $\sqrt{s} = 14$ TeV. (c) $\sqrt{s} = 27$ TeV and (d) $\sqrt{s} = 100$ TeV. For $\mathcal{L} = 300fb^{-1}$ (dash) and $\mathcal{L} = 3000fb^{-1}$ (dot). Also shown is the ATLAS-2018 limits on $\lambda_{tc} = \tilde{\rho}_{tc}\cos(\beta-\alpha)$ (dotdash) set the shaded region above this curve is excluded at 95% CL. 84

4.7 The 5σ discovery contours at the LHC in the plane of $[\cos(\beta-\alpha), \tilde{\rho}_{tc}]$ for (a) $\sqrt{s} = 13$ TeV and (b) $\sqrt{s} = 14$ TeV. (c) $\sqrt{s} = 27$ TeV and (d) $\sqrt{s} = 100$ TeV. For $\mathcal{L} = 300fb^{-1}$ (dash) and $\mathcal{L} = 3000fb^{-1}$ (dot). Also shown is the new ATLAS-2019 limits. $\lambda_{tc} = \tilde{\rho}_{tc}\cos(\beta-\alpha)$ (dotdash) set the shaded region above this curve is excluded at 95% CL. 85

4.8 Feynman diagram for the signal. 86

4.9 Invariant mass distributions for $m_{bj_1j_2}$ and $m_{j_1j_2}$ from parton level events (left) and detector level events (right). 89

4.10 Invariant mass distribution for $M_{col}(\tau\tau)$ and $M_{col}(c\tau\tau)$ with the collinear approximation, from parton level events (a) and detector simulations (b). 90

4.11 Cluster transverse mass distributions from parton level events (a) and detector simulations (b). 91

4.12 Invariant mass of two leptons,from parton level events (a) and detector simulations (b). 91

4.13 Energy of the charm in the top rest frame from parton level events (a) and detector simulations (b). 92

4.14 N_{SS} as a function of λ_{tc} for parton level events at $\sqrt{s} = 13$ TeV. . 94

4.15 BDT response from samples after (a) Set1, and, (b) Set2 pre-selection cuts. 97

4.16 Statistical significance estimate as a function of $\lambda_{tc}/\sqrt{2}$ for the two set of pre selection cuts at $\sqrt{s} = 13$ TeV for integrated luminosity $\mathcal{L} = 36.1$, 160 and 300 fb^{-1}, Here red (dashed) vertical line is the current limits set by ATLAS-2019. 98

4.17 Combined estimates of N_{SS} for $t \to ch^0$ decay channel, after including both $h^0 \to \tau^+\tau^-$ and $h^0 \to WW^*$ at parton level. 99

5.1 The observed and median expected 95% CL upper limits on $\sigma(gg \to H^0) \times (H^0 \to \mu\tau)$, for the $\mu\tau_h$ (upper) and $\mu\tau_e$ (lower) channels, for 0-jet (left) and 1-jet (right) categories. The dashed line shows the transition between the two investigated mass ranges, Sirunyan. et. al (CMS-HIG-18-017). 103

A.1 Points showing the breaking of vacuum stability (left) and perturbativity (right) of the gTHDM Higgs potential in [λ_5 - $\tan\beta$] plane. 117

A.2 Allowed region of parameter space for different M_H for $G_{hhhh} < 12.56(4\pi)$ 117

A.3 Allowed region of parameter space for different M_H but for $G_{hhhh} < 23.64$ 118

B.1 K-factor as a function of $M^0_\phi, \phi^0 = H^0, A^0$ for (a) $pp \to H^0 + X$, and (b) $pp \to A^0 + X$, from $gg \to \phi^0$, with several values of collider energy ($\sqrt{s}$). 119

B.2 Goodness of the fitting function for K-factors as function of scalar masses. On the right we present for heavy scalar and left for pseudo scalar 120

List of Tables

1.1 Fermion Masses, PDG-2016. 3

1.2 Meson octet. 6

1.3 Baryon decuplet, with charge = Q×e, e is the charge of one electron. 7

1.4 Summary of the history of most of the Standard Model particles. *Actually H Yukawa predicted a pion, it was mis-understood for a muon. 10

1.5 Weak quantum numbers of fermions. 15

1.6 NFC Models in 2HDM. 33

1.7 Yukawa Couplings of SM Higgs in NFC models. 33

2.1 Cut based optimization. 49

2.2 Cut Based optimization vs BDT. 51

3.1 Cross section of p p $\rightarrow H^0 \rightarrow W^+W^- + X$at $\sqrt{s} = 13$ TeV and ATLAS limits at $\sqrt{s} = 13$ TeV. 53

3.2 Branching fractions for different τ-lepton decays considered. . . . 59

3.3 Cross section at NNLO in pb for $pp \rightarrow \phi^0 + X$ from gluon fusion at the LHC with $\sqrt{s} = 13$ TeV. 60

3.4 Cuts. 61

3.5 Cross-sections of all the backgrounds for both leptonic and hadronic channel in fb at $\sqrt{s} = 14$, 27, and 100 TeV. With $M_{\phi^0} = 125.1$ GeV. 63

3.6 Number of events for signal and backgrounds for different M_H at $\sqrt{s} = 14$, 27, and 100 TeV for leptonic channel with $\rho_{\tau\mu} = 0.005$. 69

3.7 Number of events for signal and backgrounds for different M_H at $\sqrt{s}$ = 14, 27, and 100 TeV for hadronic τ-lepton decays, with $\rho_{\tau\mu} = 0.005$. 70

4.1 Cross-section of Higgs signal in fb. 81

4.2 Cross-section in fb for dominant physics background processes with K factors and tagging efficiencies. 82
4.3 Selection rules for parton level events. 93
4.4 Selection rules for detector simulations. 93
4.5 Cross-section of background and signal in fb after applying cuts defined in Table **4.3**. 94
4.6 Cross section of signal and backgrounds in fb. 95
4.7 Statistical significance for three values of integrated luminosities, with the current limits ATLAS limit on $\lambda_{tc} = 0.064$. 95
4.8 Cross-section for signal and background in fb, after applying Set-1 and Set-2 cuts. 96
4.9 Statistical significance at the current ATLAS limits for λ_{tc} =0.064 from the two samples. 97
4.10 Comparison between traditional cut-based vs BDT. 98
4.11 Statistical significance for $h^0 \to WW^*$ and $h^0 \to \tau\tau$ at $\sqrt{s} = 13$ TeV for $\lambda_{tc} = 0.064$. We have also shown the combined estimates of both the channels. 99

Abstract

In this dissertation, we discuss the prospect of discovering flavor changing neutral Higgs (FCNH) interactions with quarks and leptons at current and future hadron colliders. Particularly, we have looked for $t \to ch^0$ and $\phi^0 \to \tau^{\pm}\mu^{\mp}$, where ϕ^0 could be a CP-even scalar $\left[h^0 \text{ (lighter), } H^0 \text{ (heavier)}\right]$ or a CP-odd pseudo-scalar (A^0). A general two Higgs doublet model (gTHDM) is used to simulate $t \to ch^0$ and $\phi^0 \to \tau^{\pm}\mu^{\mp}$ decays. The LHC measurements of the light Higgs boson (h^0) favor the decoupling limit of gTHDM, in which the couplings of h^0 approach Standard Model values. In this limit, FCNH couplings of the light Higgs boson h^0 are naturally suppressed by a small mixing parameter $\cos(\beta-\alpha)$, while the FCNH couplings of heavier neutral Higgs bosons H^0, andA^0 are sustained by $\sin(\beta-\alpha) \sim 1$. Promising results are found for the LHC collision energies $\sqrt{s} = 13$ TeV and 14 TeV. In addition, we study the discovery potential of future pp colliders, with $\sqrt{s} = 27$ TeV and 100 TeV. For $\phi^0 \to \tau^{\pm}\mu^{\mp}$, we evaluate the production rate of physics background from dominant processes ($\tau^+\tau^-, WW, ZZ, Wq, Wg, t\bar{t}$) with realistic acceptance cuts and tagging efficiencies. For $t \to ch^0$, where top is coming from top pair production, we consider $h^0 \to WW^* \to \ell^+\ell^- + \not{E}_T$ and $h^0 \to \tau^+\tau^- \to \ell^+\ell^- + \not{E}_T$ and another top decaying hadronically to a b quark and two light jets. For this report we have studied $h^0 \to WW^*$ and $h^0 \to \tau^+\tau^-$ separately. Our analysis suggests a reach of 5σ or better, with integrated luminosity $\mathcal{L} = 3\ ab^{-1}$ and $\sqrt{s} = 13$, 14 and 27 TeV for $\lambda_{tc} \leq 0.064$, under the current ATLAS limits for both light Higgs decay mode separately. For $h^0 \to WW^*$ we have also presented the discovery potential at 100 TeV.

Chapter 1

Introduction

1.1 Structure of Standard Model

The Standard Model (SM) of particle physics describes the spectrum of the elementary particles and their interactions. The SM is a quantum field theory with gauge group symmetry where particles are classified based on their quantum properties and their interactions with other particles. As a model it describes our current understanding of particles making up the visible Universe and has been the most successful single model to date; explaining nearly every experimental observation that has been made in particle physics. The SM was first given this name by Abraham Pais and Sam Treiman in 1975 [1]. But collectively, the development of the SM is the culmination of decades of work from several great particle physicists from all over the world. It combines three fundamental interactions, electromagnetic, weak, and strong interactions, into one particle physics model.

SM particles form two broad categories, matter particles called quarks and leptons form the fermions and the interaction mediators form the gauge bosons. A more technical categorization will be, fermions are particles with spin (2n+1)/2, with n = 0,1,2.. and they follow the Fermi-Dirac statistics [2, 3], formulated by Enrico Fermi and Paul Dirac. Fermions follow the Pauli-exclusion principle, which means two fermions cannot have the same set of quantum numbers. Bosons have integer spins and they follow the Bose-Einstein statistics [4], pioneered by Satyendra Bose and Albert Einstein and do not follow the Pauli-exclusion principle.

There are two different types of fermions: leptons and quarks. Leptons, which

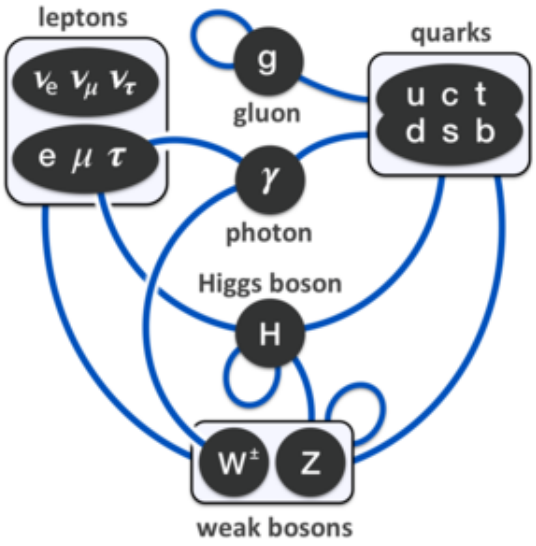

Figure 1.1: Standard Model (by Eric Drexler, Wikipedia)

consist of the electron (e), the muon (μ) , the tau-lepton (τ) and the electron-neutrino (ν_e),the muon-neutrino (ν_μ) the tau-neutrino (ν_τ). Each of these particles and their corresponding neutrino form a generation of the leptons bringing our total count of generations to three. Each of these pairs called doublets, also have matching antiparticle and antineutrino pairs but for simplicity, Fig. **1.1** above only shows the matter particles and not the antimatter particles. Quarks like leptons, also form three generations consisting of: {up(u), down(d)}, {charm(c), strange(s)}, and {top(t), bottom(b)} quarks as I, II and III generations respectively. The primary difference between each generations is that; the higher the generation the heavier the particles, as shown in Table. **1.1**, from PDG-2016 [5]:

Leptons	Mass(GeV/c^2)	Quarks	Mass(GeV/c^2)
ν_e	$< 1 \times 10^{-8}$	u	0.0022 ± 0.0006
e	$0.000511 \pm 3.1 \times 10^{-11}$	d	0.0047 ± 0.0005
ν_μ	$< 1.6 \times 10^{-4}$	c	1.27 ± 0.03
μ	$0.1056 \pm 2.4 \times 10^{-8}$	s	0.096 ± 0.008
ν_τ	$< 1.8 \times 10^{-2}$	t	$173.2 \pm 0.51 \pm 0.71$
τ	1.776 ± 0.00012	b	4.66 ± 0.04

Table 1.1: Fermion Masses, PDG-2016.

For bosons, there are 8 gluons(g), which are the mediators of strong interactions, 3 mediators of weak interactions, the $W^\pm$ and Z bosons; and finally a photon (γ) for electromagnetic interactions. At last but certainly not least, we have the Higgs boson as the physical spin-0 particle from the Higgs mechanism that generates mass for all elementary particles. We will discuss this in full detail in the subsequent sections.

1.1.1 Leptons

Leptons are different from quarks because:

- They exist independently in nature,
- They carry integer multiple of charge "e",
- They only interact through photons, $W^\pm$ and Z bosons
- They are light (except for the τ-lepton which is heavier than a charm quark).

Leptons received their name from a Greek word "leptos," meaning thin, delicate, lightweight. The first lepton was discovered in 1897 [6], by the British physicist J.J

Thompson, through cathode ray experiments. He called the particles "corpuscles," the particle he discovered was later given its name "electron" by G.F Fitzgerald, J Larmor, and H.A Lorenz [7].

The muon was discovered by Carl D Anderson and Seth Nedder at Caltech in 1936 [8]. These two pioneering physicists were studying cosmic radiation when they stumbled upon a particle that had a wider arc than an electron would when passed through the same magnetic field. This suggest the particle has the same charge as the electron but heavier. The new particle was initially called a mesotron and was misunderstood for a pion (π) [9]. Yung Su Tsai predicted the τ-lepton in 1971 [10], and was later discovered in a series of experiments performed at SLAC from 1974-77 [11, 12].

Neutrinos are a special set of particles that were initially introduced to conserve energy in the nuclear beta decay experiments in 1930. These nuclear beta decays were showing signs of missing energy, because only two particles were observed: a daughter nucleus and an electron. Just like any other two-body decays, we would expect electrons to have fixed energy. But, instead their energy showed a distribution [9] and not a sharp peak. Following this discovery Pauli presented an idea of an invisible neutral particle, which he named "neutron", and the following year Enrico Fermi presented his theory of beta decay by including the Pauli particle, which he called "neutrino" [13]. What was actually observed is now identified as an anti-neutrino.

Later in the 1950s, 1960s, and 1970s, it became evident that there are three kinds of neutrinos because of an upcoming new idea of lepton number conservation; more specifically, electron number, muon number, and tau-lepton number conservation. With e^- and ν_e both having the electron number 1 and same for other generations [9]. Antiparticles, however, carry the opposite lepton number as their matter cousins, e.g. -1 is the electron number for the positron and its

neutrino pair. One of the limitations of the SM that leads us to believe there is something more to the picture is that there is no strong reason why this symmetry should exist.

1.1.2 Antiparticles

In 1927 Paul Dirac was troubled by the fact that for every positive energy solution coming from the relativistic energy equation, i.e., $E^2 - p^2c^2 = m^2c^4$ for electrons, there were negative energy solutions as well [14]. To explain this, he postulated that the negative energy solutions form a sea of negative energy states filled with the electrons. When we supply enough energy to knock one of the electrons from the sea of the negative energy states, its absence will be seen as a net positive charge. In 1931 C Anderson [15] and his group discovered the positron, a twin of the electron, with the same mass but opposite charge. Dirac's interpretation was later redefined as an existence of anti-electron or positron carrying a positive charge and having the same positive energy by Feynman and Stueckelburgh in 1940 [16, 17]. In the following decades, nearly every SM particle and antiparticle were discovered.

The standard notation for an antiparticle is put a bar on top of the matter particle or particle symbol. For example, an anti-proton is denoted as $\bar{p}$ and an anti-neutrino $\bar{\nu}$. Charged leptons are an exception to this rule, they are denoted by e^+, μ^+, τ^+ for anti-electron, anti-muon and anti-tau-lepton, respectively. Here we can construct a "C" operator, called the charge conjugation operator [9], which, when applied to any particle state, converts it into its respective antiparticle,

$$C|p\rangle = |\bar{p}\rangle. \tag{1.1}$$

This was the beginning of merging quantum mechanics and special relativity,

which predicted matter/antimatter symmetry. However, this also introduced some additional questions because the current state of the Universe is matter dominated. The only way to reconcile this observation was to introduce an asymmetry.

1.1.3 Quarks, Meson, and Baryons

Quarks are the fermions which do not exist freely in nature. Instead, they either form confined states or decay before those confined states can be formed. They carry charges in the multiples of 1/3 of e, which is the electric charge of one electron. Their existence was first postulated by Gell-Mann [18] and Zweig [19] independently in 1964 to explain why mesons and baryons fit in octets and decuplets.

qq	Q	S(strange)	Meson
$(u\bar{u}$ - $d\bar{d})/\sqrt{2}$	0	0	π^0
$u\bar{d}$	1	0	π^+
$d\bar{u}$	-1	0	π^-
$(u\bar{u} + d\bar{d} - 2s\bar{s})/\sqrt{6}$	0	0	η
$u\bar{s}$	1	1	K^+
$d\bar{s}$	0	1	K^0
$s\bar{u}$	-1	-1	K^-
$s\bar{d}$	0	-1	$\bar{K}^0$
$(u\bar{u} + d\bar{d} + s\bar{s})/\sqrt{3}$	0	0	η‘

Table 1.2: Meson octet.

They suggested that mesons and baryons are composed of more elementary particles, which later became known as quarks. They suggested that there are three types (or flavors) of quarks u, d, and s (up, down, and strange) that combine into the mesons and baryons that Gell-Mann and Zweig were studying. A meson

is a quark and an antiquark-confined state and a baryon is a composite state of three quarks or antiquarks. The up quark carries a charge of $2e/3$, whereas down and strange quark carry a -1$e/3$ charge. With this information we can construct the baryon decuplet and meson octet [9, 20] by just combining the three flavors as shown in Table. **1.2** for the mesons and Table. **1.3** for the baryons [9, 20]. In the table below Q is the charge operator, with the actual charge of any particle being $Q \times e$ and S denoting how many strange quarks are in the confined states.

qqq	Q	S	Baryon
uuu	2	0	Δ^{++}
uud	1	0	Δ^{+}
udd	0	0	Δ^{0}
ddd	-1	0	Δ^{-}
uus	1	-1	Σ^{*+}
uds	0	-1	Σ^{*0}
dds	-1	-1	Σ^{*-}
uss	0	-2	Ξ^{*0}
dss	-1	-2	Ξ^{*-}
sss	-1	-3	Ω^{-}

Table 1.3: Baryon decuplet, with charge = Q$\times e$, e is the charge of one electron.

Similarly, neutron and protons are made up of udd and uud. To understand the difference between them and the Δ particles, we have to define a new quantum number, which we will discuss in a bit. First, let's discuss a more intrinsic property of the quarks, known as color. The Pauli exclusion principle forbids any fermion of the same quantum numbers to co-exist, however, in the baryonic state, we have three up quarks with the same quantum numbers. In order to account for this

seemingly impossible phenomenon a new quantum number, called color, specific to quarks was introduced. There are three color for quarks: red, blue, and green. In the example presented above, the quarks in the uuu baryonic state carries a different color. Similarly, antiquarks carry either minus red, minus blue, or minus green. As we have seen with normal color, when you mix red, green, and blue, it gives a white or colorless state. This aligns with the observation that all naturally occurring particles are colorless. This quantum property only allows for a state containing either three quark (qqq) or antiquarks ($\bar{q}\bar{q}\bar{q}$), a pair of quark and antiquarks ($q\bar{q}$). In the late 1960s and 1970, deep inelastic experiments at SLAC and CERN indicated that, like an atom, a proton also has a substructure containing three lumps; this was the first evidence for the quark model. Later in 1974, the J/ψ [21, 22] meson was discovered indicating the presence of a fourth quark called charm. B mesons were discovered in 1977 at SLAC [23], which are bound states of b (bottom) quark. The heaviest quark "top" was discovered at Tevatron by CDF and D$\emptyset$ in 1995 at Fermilab [24]. This discovery completed the three generations of quarks just like the leptons.

Discovery of the three new quarks c, b, and t opened up the discovery of more mesons and baryons formed from their combinations in addition to the previously known quarks. The only quark that has not been found in a bound meson or a baryon state is the top quark as its mass and instability cause it to decay before forming such a state.

Another physical observation that lead to the discovery of a new quantum number is that protons and neutrons have roughly the same mass but different charge. The new quantum number that was introduced is isospin with the proton having an isospin of 1/2 and neutron having an isospin of -1/2. Isospin is a different property than the spin. The primary difference between the proton and a Δ^+ are their isospins, which are 1/2 and 3/2, respectively. Similarly, the Δ^0 and the

neutron have isospin of -3/2 and -1/2, respectively.

1.1.4 Vector Bosons

Vector gauge bosons are spin 1 particles and the mediator of interactions. The photon is the carrier of electromagnetic interactions. Photon was first proposed by Planck in 1900 [25], to explain the UV catastrophe [26]. UV divergent results were obtained when statistical mechanics was used for explaining the spectrum of electromagnetic radiation emitted from the black body. Planck suggested that if the light is quantized, with each quantum carrying an energy $E = h\nu$, he can explain the black body spectrum [25]. However, Planck proposed this quantization of light specifically for the black body radiation. Later, Albert Einstein modified Planck's proposal by postulating that quantization of light is light's intrinsic property. He used his postulate to explain the photoelectric effect [26, 27] successfully. He called them "light quantum," which was later named "photon" by Gilbert Lewis. The presence of the photon was confirmed via two different experiments, one by Millikan in 1916 [9, 28] that confirmed Einstein's explanation for the photoelectric effect and later by A.H Compton in 1923 via Compton scattering [29].

Just like the photon with the electomagnetic interactions, the $W^{\pm}$ and Z boson are the carriers of weak interactions. In 1933 when Enrico Fermi proposed his theory for nuclear beta decay [9, 13, 26], he assumed point interactions; however, this approach fails at very high energies, which suggested that theory with a mediator was needed. Glashow, Weinberg, and Salam proposed their electroweak interaction theory [30] including $W^{\pm}$ and Z as a mediator of weak interactions. We will discuss this in Sec 1.1.7. Using their model, they estimated the mass of

Particle	Year	Predicted by	Discovered by
e^-	1897	JJ Thompson	JJ Thompson
μ^-	1937	H.Yukawa*	Anderson & Neddermeyer
τ^-	1974-77	Yung Su Tsai	SLAC
u,d and s	1968	Gell Mann & Zweig	SLAC
c	1974	Glashow, Iliopoulos and Maiani	SLAC
b	1977	Kobayashi and Masakawa	E288 exp,Fermilab
t	1995	Kobayashi and Masakawa	CDF & DØ
W & Z	1983	Glashow,Weinberg and Salam	SPS exp, CERN
h^0	2012	Higgs/Englert	ATLAS and CMS

Table 1.4: Summary of the history of most of the Standard Model particles. *Actually H Yukawa predicted a pion, it was mis-understood for a muon.

$W^{\pm}$ and Z to be,

$$M_W = 82 \pm 2 \text{ GeV/c}^2, \quad M_Z = 92 \pm 2 \text{ GeV/c}^2 .$$

In January 1983, the UA1 group at CERN discovered the $W^{\pm}$ boson [31], and 5 months later, they announced the discovery of the Z boson [32] as well. They measured their masses to be,

$$M_W = 81 \pm 5 \text{ GeV/c}^2 , \quad M_Z = 95.2 \pm 2.5 \text{ GeV/c}^2 .$$

These experiments presented the SM's triumph, making it the most successful theory explaining particle and particle interactions to date. In Table. **1.4**, we summarize the discoveries of all the SM elementary particles.

1.1.5 Quantum Electrodynamics (QED)

QED is the simplest gauge invariant theory, as it only consists of one gauge field. It follows U(1) gauge symmetry, and it describes the interaction of a photon with the fermions. Fermions are charged under a U(1) gauge group, which is

popularly referred as electric charge. The simplest gauge invariant Lagrangian $\mathcal{L}$ [20, 30] is given as,

$$\mathcal{L} = -\frac{1}{4}F_{\mu\nu}F^{\mu\nu} + \bar{\psi}(i\gamma^{\mu}D_{\mu} - m)\psi\,. \tag{1.2}$$

Here, $F_{\mu\nu}$ is the electromagnetic field tensor,

$$F_{\mu\nu} = \partial_{\mu}A_{\nu} - \partial_{\nu}A_{\mu}\,, \tag{1.3}$$

and, D_{μ} is the covariant derivative, given as,

$$D_{\mu} = \partial_{\mu} + ieQA_{\mu}\,. \tag{1.4}$$

Where e is the unit of electric charge and Q is the charge operator. Above Lagrangian is invariant under the local gauge transformations,

$$\psi(x) \to U(x)\,\psi(x), \quad A_{\mu}(x) \to A_{\mu}(x) + \frac{1}{e}\partial_{\mu}\alpha(x)\,, \tag{1.5}$$

where U(x) = $\exp(-i\,e\,Q\alpha(x))$, because a photon (A_{μ}) is massless.

1.1.6 Quantum Chromodynamics (QCD)

Quantum chromodynamics is a non-abelian gauge theory of strong interactions between quarks and gluons. SU(3) is the gauge group and gluons are the gauge bosons. Quarks are charged under SU(3), carrying a color charge. There are three types of colored quarks, forming a triplet under the fundamental representations of the gauge group. There are eight gluons, and they form the octet as the adjoint representation of the SU(3) gauge group. The generalized form of the

Lagrangian [20, 30] is,

$$\mathcal{L} = -\frac{1}{4}F_a^{\mu\nu}F_{a\mu\nu} + \bar{\psi_j}(i\gamma_\mu D_{jk}^\mu - m_{jk})\psi_k \,. \tag{1.6}$$

Where the indices, a, represents the color, and takes a = 1,...,8. Whereas, i and j are the sum over different quarks and takes i, j = 1,2,3 values. The covariant derivative acting on the quark field [30] is:

$$D_{jk}^\mu = \delta_{jk}\partial^\mu + ig_s(T_a)_{jk}G_a^\mu \,. \tag{1.7}$$

Where G_a^μ are the gluon fields, T_a are the SU(3) generators, represented by Gell-mann matrices, and g_s is the strong coupling. The Gluon field tensor is given as [30]:

$$F_a^{\mu\nu} = \partial^\mu G_a^\nu - \partial^\nu G_a^\mu - g_s f_{abc}G_b^\mu G_c^\nu \,. \tag{1.8}$$

Where f_{abc} are the structure constants of the SU(3) gauge group, following the Lie algebra of the group generators [30]:

$$[T_a, T_b] = if_{abc}T_c \,. \tag{1.9}$$

This Lagrangian is also invariant under the infinitesimal local gauge transformations:

$$\psi(x) \to [1 - ig_s\alpha_a(x)T_a]\psi(x) \,, \tag{1.10}$$

$$G_a^\mu(x) \to G_a^\mu(x) + \partial^\mu\alpha_a(x) + g_s f_{abc}\alpha_b G_c^\mu \,. \tag{1.11}$$

1.1.7 Electroweak Interactions and Higgs Mechanism

The electromagnetic interactions are the most common form of interactions, and we witness their impact in our day to day life. Strong interactions binds the nuclei. Weak interactions are responsible for the nuclear beta decays and nuclear fusion. They are the only source of parity violation (P) and charge conjugation + parity (CP) violation in the SM.

Weak interactions follow the SU(2) gauge group symmetry, which has the isospin $\tau = 1/2$ fields transforming as the isospin doublets of SU(2) gauge group. Similar to QED, gauge invariance requires symmetry under the infinitesimal local gauge transformation:

$$\psi(x) \rightarrow [1 - ig\alpha(x) \cdot \tau]\psi(x)\,. \tag{1.12}$$

Where $\alpha(x)$ is an infinitesimal vector in the isospin space and $\tau = \{\tau_1, \tau_2, \tau_3\}$ are the generators of the SU(2) symmetry transformation. The τ_i, follows Lie algebra,

$$[\tau_i, \tau_j] = i\epsilon_{ijk}\tau_k\,. \tag{1.13}$$

The gauge group is non-abelian. The matrix representation of τ_i is $\frac{1}{2}\sigma_i$, here σ_i are the Pauli matrices. The gauge invariance follows a similar form as that in the QED, but here the covariant derivative is given as [30],

$$D_\mu = \partial_\mu + igW_\mu \cdot \tau\,. \tag{1.14}$$

W_μ are the Yang-Mills fields and for gauge invariance of the Lagrangian they transform as,

$$W_\mu \rightarrow W_\mu + \partial_\mu\alpha(x) + g\alpha(x) \times W_\mu\,. \tag{1.15}$$

The $\alpha(x) \times W_\mu$ appears because W_μ is an SU(2) vector and the cross product of any two vectors $\vec{a}$ and $\vec{b}$ can be written as:

$$\vec{a} \times \vec{b} = \sum_i \sum_j \sum_k \epsilon_{ijk} a_j b_k$$

and here ϵ_{ijk} is also the structure constant of the SU(2) gauge group.

For every τ_i there is a gauge field $W_{i\mu}$ and the complete gauge invariant Lagrangian describing the weak interaction is,

$$\mathcal{L} = -\frac{1}{4} W_{i\mu\nu} W^{i\mu\nu} + \bar{\psi}(i\gamma^\mu D_\mu)\psi \,, \tag{1.16}$$

where $W_{i\mu\nu} = \partial_\mu W_{i\nu} - \partial_\nu W_{i\mu} - g f_{ijk} W_{j\mu} W_{k\nu}$.

Weak interactions have a peculiar property, mainly they only interact with the left handed fermions. To incorporate this left handedness of the weak interactions, a left handed $SU(2)_L$ gauge symmetry is applied to the left handed fermions. Where the left and right handed fermions are given as,

$$\psi_L = \frac{1}{2}(1 - \gamma_5)\psi, \qquad \psi_R = \frac{1}{2}(1 + \gamma_5)\psi \,. \tag{1.17}$$

Now the fermion mass term is no longer gauge invariant under the $SU(2)_L$ gauge transformations, as $m\bar{\psi}\psi = m(\bar{\psi}_R\psi_L + \bar{\psi}_L\psi_R)$.

An additional $U(1)_Y$ gauge symmetry is introduced whose quantum number is the weak hypercharge, Y. Weak hypercharge, Y plays, an important role in unifying the electromagnetic interaction with the weak interaction. The weak hypercharge is specified according to the formula [20, 30]:

$$Q = \tau_3 + \frac{1}{2} Y \,. \tag{1.18}$$

Right handed fermions transform under this new $U(1)_Y$ gauge group only, whereas left handed fermions transforms under the $SU(2)_L \times U(1)_Y$ gauge group, this structure can incorporate the left-handedness of the weak interactions. Now the weak quantum numbers for the fermions are given in Table. **1.5**, where $e_{R,L}$ = charged leptons, ν_L = neutrinos, u_R = up type quarks and d_R = down type quarks.

	τ	τ_3	Y	Q
ν_L	$\frac{1}{2}$	$\frac{1}{2}$	-1	0
e_L	$\frac{1}{2}$	$-\frac{1}{2}$	-1	-1
u_L	$\frac{1}{2}$	$\frac{1}{2}$	$\frac{1}{3}$	$\frac{2}{3}$
d_L	$\frac{1}{2}$	$-\frac{1}{2}$	$\frac{1}{3}$	$-\frac{1}{3}$
e_R	0	0	-2	-1
u_R	0	0	$\frac{4}{3}$	$\frac{2}{3}$
d_R	0	0	$-\frac{2}{3}$	$-\frac{1}{3}$

Table 1.5: Weak quantum numbers of fermions.

With the introduction of new $U(1)_Y$ gauge symmetry along with $SU(2)_L$ a new gauge field B_μ, was introduced along with the $W_{i\mu}$ field. All of these gauge fields have to be massless under the gauge transformations. The new gauge invariant Lagrangian is:

$$\mathcal{L} = -\frac{1}{4} W_{i\mu\nu} W^{i\mu\nu} - \frac{1}{4} B_{\mu\nu} B^{\mu\nu} + \bar{\psi} i \gamma^\mu D_\mu \psi \,. \qquad (\mathbf{1.19})$$

Here $B_{\mu\nu} = \partial_\mu B_\nu - \partial_\nu B_\mu$ and the covariant derivative is:

$$D_\mu = \partial_\mu + i g W_\mu \cdot \tau + i g^{'} \frac{1}{2} B_\mu Y \,. \qquad (\mathbf{1.20})$$

We can expand $W_\mu \cdot \tau = W^+ \tau^+ + W^- \tau^- + W_3 \tau_3$, here $W^\pm = (W_1 \pm i W_2)/\sqrt{2}$ are the famous $W^\pm$ bosons and $\tau^+(\tau^-)$ are raising(lowering) operators defined

as $\tau^{\pm} = (\tau_1 \pm i\tau_2)/\sqrt{2}$. The electromagnetic and weak interaction is unified by equating the $i(gW_{3\mu}\tau_3 + g^{'}\frac{1}{2}B_{\mu}Y)$ with $ieQA_{\mu}$ and then performing a rotation on $W_{3\mu}$ and B_{μ} to the physical neutral fields A_{μ} and Z_{μ},

$$\begin{pmatrix} W_{3\mu} \\ B_{\mu} \end{pmatrix} = \begin{pmatrix} \cos\theta_w & \sin\theta_w \\ -\sin\theta_w & \cos\theta_w \end{pmatrix} \begin{pmatrix} Z_{\mu} \\ A_{\mu} \end{pmatrix} , \qquad (\mathbf{1.21})$$

here θ_w is the weak mixing angle or the Weinberg angle. Using the above mixing matrix and equations for electroweak unification, we get,

$$g \sin\theta_w = g^{'} \cos\theta_w = e \, . \qquad (\mathbf{1.22})$$

So we can write the electroweak interaction Lagrangian as,

$$-\mathcal{L} = eJ^{\mu}A_{\mu} + \frac{1}{2}(J_L^{+\mu}W_{\mu}^{+} + J_L^{-\mu}W_{\mu}^{-}) + g_z J_Z^{\mu} Z_{\mu} \, . \qquad (\mathbf{1.23})$$

Where,

$$\begin{aligned} J_{em}^{\mu} &= \bar{\psi}\gamma^{\mu}Q\psi \, , \\ J_L^{\pm\mu} &= \sqrt{2}\bar{\psi}\gamma^{\mu}\tau_L^{\pm}\psi \, , \\ J_Z^{\mu} &= \bar{\psi}\gamma_{\mu}[\tau_{3L} - x_w Q]\psi \, , \end{aligned}$$

here $g_z \sin\theta_w \cos\theta_w = e$, and $x_w = \sin^2\theta_w$.

This model for the electroweak interaction is invariant under the SU(2) gauge transformations if and only if the $W^{\pm}, Z$ bosons, and all the fermions are massless.

Higgs Mechanism and Mass of Vector Bosons

Gauge symmetry is the heart of any quantum field theory. But, with the discovery of massive $W^{\pm}$ and Z gauge fields, the electroweak Lagrangian is no longer symmetric under the gauge transformation described in Eq 1.15. One way out of this problem is ignorance, which means forcefully keeping the mass terms, but that would make the theory non-renormalizable; in other words, it cannot predict any observable at very high energies like the GUT scale ($\sim 10^{16}$ GeV). Another way would be to introduce a "Hidden symmetry" and then spontaneously break this symmetry to generate the mass of the vector bosons. Let's give this idea a technical explanation. To introduce the mass terms for the vector bosons $W^{\pm}$ and Z, we introduce a scalar doublet ϕ [33],

$$\phi = \begin{pmatrix} \phi^{+} \\ \phi^{0} \end{pmatrix} . \tag{1.24}$$

The doublet above follows the self-interaction Lagrangian of the Higgs field is given as,

$$\mathcal{L}_{(\phi)} = \partial^{\mu}\phi^{\dagger}\partial_{\mu}\phi - V(\phi) , \tag{1.25}$$

here,

$$V(\phi) = \frac{1}{2}\mu^{2}\phi^{\dagger}\phi + \frac{1}{4}\lambda|\phi^{\dagger}\phi|^{2} . \tag{1.26}$$

$V(\phi)$ do not have a global minimum at $|\phi^{0}| = 0$, if $\mu^{2} < 0$, as shown in Fig. **1.2**(b). Instead, it has a global minimum at $\phi^{0} = \pm v$, where $v = \sqrt{-\mu^{2}/\lambda}$. For the convergence of the perturbative expansion, we should expand the above Higgs potential around v. In other words, it means that the Higgs field has a non zero vacuum expectation value (VEV). This way of choosing a particular VEV $\phi^{0} = v$ makes the Higgs potential asymmetric in the weak isospin - hypercharge space,

which "spontaneously breaks" the $\mathrm{SU}(2)_L \times \mathrm{U}(1)_Y$ gauge symmetry.

We can redefine the scalar doublet as [30],

$$\phi(x) = \exp(i\frac{\varepsilon(x)\cdot\tau}{2v}) \begin{pmatrix} 0 \\ (v+h(x))/\sqrt{2} \end{pmatrix} . \qquad (\mathbf{1.27})$$

Such that $h(x)$ and $\varepsilon(x)_i$ $(i = 1, 2, 3)$ have zero VEV. A finite gauge transformation under the $\mathrm{SU}(2)_L$ given by $\alpha(x) = \varepsilon(x)/v$ the phase factor of $\phi(x)$ can be eliminated from appearing in the Lagrangian by redefinition of the scalar fields. When we substitute this into $V(\phi)$, it is no longer symmetric under a Z_2 transformation of $h(x)$, i.e. $h(x) \to -h(x)$ as shown in Fig. **1.3**.

At this point it is important to state the Goldstone theorem, which says that: *"mass-less spin-0 particles appear in a theory whenever a continuous symmetry is spontaneously broken"*.

The massless Goldstone bosons represents the ground state excitation's [30, 34] of the Higgs field. When the Higgs mechanism breaks the local gauge symmetry, three massless Goldstone bosons are eaten away in the scalar-sector, and they reappear as three massive gauge bosons which are $W^{\pm}$ and Z [30, 34].

We can express the covariant derivative on the scalar doublet in terms of the physical A, $W^{\pm}$, and Z fields [30],

$$D_\mu = \partial_\mu + ieQA_\mu + i\frac{1}{\sqrt{2}}g(\tau^+W_\mu^+ + \tau^-W_\mu^-) + ig_Z(\frac{1}{2}\tau_3 - x_wQ)Z_\mu \,. \qquad (\mathbf{1.28})$$

In the Unitary gauge, where $\phi(x)$ only has the neutral component,

$$\phi(x) = \frac{1}{\sqrt{2}} \begin{pmatrix} 0 \\ v+h(x) \end{pmatrix}, \qquad (\mathbf{1.29})$$

for convenience we write $H(x) \to H$, the covariant derivative from Eq 1.28, when operated on $\phi(x)$ from Eq 1.29 gives,

$$D_\mu \phi = \frac{1}{\sqrt{2}} \begin{pmatrix} \frac{1}{\sqrt{2}} i g W_\mu^+ (v+h) \\ \partial h - \frac{1}{2} i g_z Z_\mu (v+h) \end{pmatrix} . \tag{1.30}$$

Expanding the Lagrangian with this covariant derivative after replacing $\partial_\mu \to D_\mu$ in Eq 1.25 we get,

$$\begin{aligned} \mathcal{L}_\phi &= \frac{1}{2}(\partial h)^2 + \frac{1}{4} g^2 v^2 W^+ W^- + \frac{1}{8} g_z^2 v^2 Z Z \\ &+ \frac{1}{4} g^2 h^2 W^+ W^- + \frac{1}{8} g_z^2 h^2 Z Z + \frac{1}{2} g^2 v h W^+ W^- + \frac{1}{4} g_z^2 v h Z Z \\ &- (\frac{1}{2}\mu^2 (v+h)^2 + \frac{1}{4}(v+h)^4) . \end{aligned}$$

The mass terms for $W^\pm$ and Z bosons are $M_W = \frac{1}{2} g v$ and $M_Z = \frac{1}{2} g_z v$. $\mathcal{L}_\phi$ does not have any mass term for photons, or even an interaction term between photons and the Higgs boson, so even with this mechanism the photon stays massless.

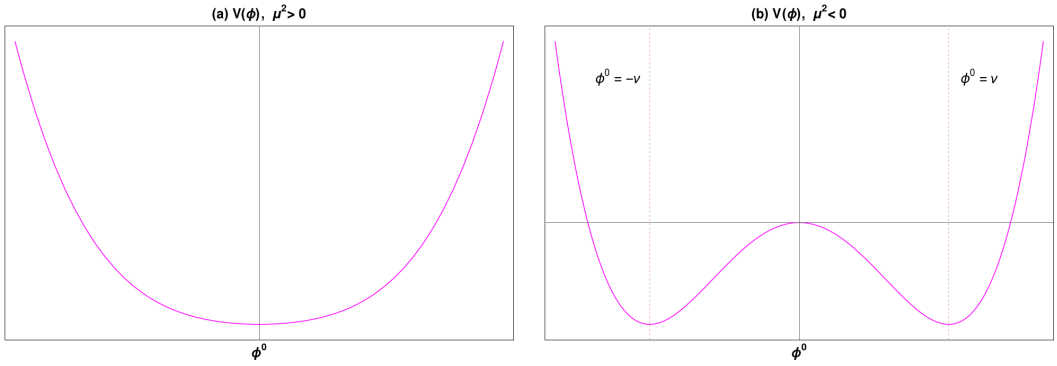

Figure 1.2: Higgs potential with (a) $\mu^2 > 0$, and, (b) $\mu^2 < 0$.

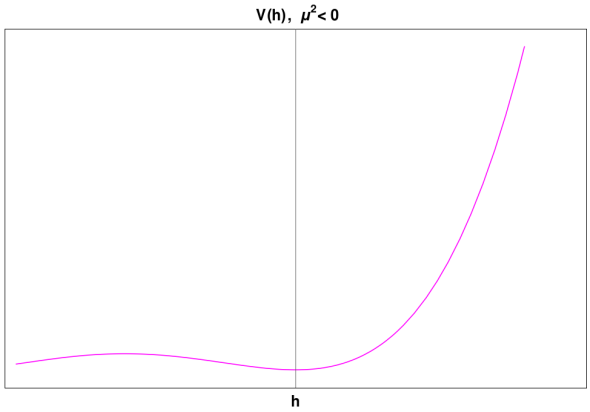

Figure 1.3: Higgs potential after symmetry breaking.

Mass Generation for Fermions

In the SU(2)$_L\times$ U(1)$_Y$ electroweak model, a fermion mass term $m(\bar{\psi}_L\psi_R+\bar{\psi}_R\psi_L)$ breaks the gauge symmetry. When the Higgs doublets spontaneously breaks the electroweak symmetry, it also breaks the SU(2)$_L\times$ U(1)$_Y$ gauge symmetry for the fermions, which generates the mass terms for the fermions.

For leptons, we can write there interaction with the doublet in the following form [30],

$$\mathcal{L}_{Y\ell} = -y_\ell\left[(\bar{\nu}_\ell,\bar{\ell})_L\begin{pmatrix}\phi^+\\ \phi^0\end{pmatrix}\ell_R + \bar{\ell}_R(\phi^-,\phi^0)\begin{pmatrix}\nu_\ell\\ \ell\end{pmatrix}_L\right]. \qquad \textbf{(1.31)}$$

Substituting Eq 1.29 here, we get,

$$\mathcal{L}_{Y\ell} = -\frac{y_\ell}{\sqrt{2}}v(\bar{\ell}_L\ell_R+\bar{\ell}_R\ell_L) - \frac{y_\ell}{\sqrt{2}}h(\bar{\ell}_L\ell_R+\bar{\ell}_R\ell_L)\,, \qquad \textbf{(1.32)}$$

here ℓ = electron, muon and tau-lepton. The mass of leptons is given as $m_\ell = y_\ell v/\sqrt{2}$. The y_ℓ is popularly known as the Yukawa couplings and the Lagrangian describing these interactions is known as the Yukawa Lagrangian.

For quarks, the masses are generated by the Yukawa couplings with the Higgs

doublet. The weak eigenstates of quarks in the unbroken gauge group are,

$$Q_{jL} \equiv \begin{pmatrix} u_j \\ d_j \end{pmatrix}_L , u_{jR}, d_{jR}, \quad j = 1, 2, 3 \,.$$

The most general $\mathrm{SU}(2)_L \times \mathrm{U}(1)_Y$ invariant Yukawa Lagrangian for the quarks is [30],

$$\mathcal{L}_{YQ} = -\sum_{i=1}^{3}\sum_{j=1}^{3}\left[\tilde{Y}_{ij}\bar{u}_{iR}\tilde{\phi}^{\dagger}Q_{jL} + Y_{ij}\bar{d}_{iR}\phi^{\dagger}Q_{jL}\right] + \mathrm{H.c.}\,, \qquad (\mathbf{1.33})$$

here,

$$\tilde{\phi} = i\tau_2\phi^* = \begin{pmatrix} \phi^{0*} \\ -\phi^- \end{pmatrix} .$$

After spontaneous symmetry breaking of the gauge symmetry, we get the mass terms of up-type and down-type quarks as,

$$(\bar{u}_1, \bar{u}_2, \bar{u}_3)_R \mathcal{M}_u \begin{pmatrix} u_1 \\ u_2 \\ u_3 \end{pmatrix} + \mathrm{H.c}\,,$$

$$(\bar{d}_1, \bar{d}_2, \bar{d}_3)_R \mathcal{M}_d \begin{pmatrix} d_1 \\ d_2 \\ d_3 \end{pmatrix} + \mathrm{H.c.}\,.$$

Where, $\mathcal{M}_{uij} = \frac{v}{\sqrt{2}}\tilde{Y}_{ij}$ and $\mathcal{M}_{dij} = \frac{v}{\sqrt{2}}\tilde{Y}_{ij}$ are quark mass matrices and they are not hermitian. The above Yukawa matrices can be transformed to diagonal matrices by a unitary transformation, that takes the quarks from the interaction basis to

the physical mass basis in the broken phase.

$$\begin{pmatrix} u_1 \\ u_2 \\ u_3 \end{pmatrix}_{L,R} = U_{L,R} \begin{pmatrix} u \\ c \\ t \end{pmatrix} \quad , \quad \begin{pmatrix} d_1 \\ d_2 \\ d_3 \end{pmatrix}_{L,R} = D_{L,R} \begin{pmatrix} d \\ s \\ b \end{pmatrix} , \tag{1.34}$$

and the mass matrices transforms as,

$$U_R^{-1} \mathcal{M}_u U_L = \begin{pmatrix} m_u & 0 & 0 \\ 0 & m_c & 0 \\ 0 & 0 & m_t \end{pmatrix} ,$$

$$D_R^{-1} \mathcal{M}_d D_L = \begin{pmatrix} m_d & 0 & 0 \\ 0 & m_s & 0 \\ 0 & 0 & m_b \end{pmatrix} .$$

The weak eigenstates u_i and d_i are the linear mixture of the mass eigenstates u, c t and d, s, b with different relations for left and right chirality. Rewriting the Yukawa Lagrangian in the broken phase and mass basis for quarks, we get:

$$\mathcal{L}_{YQ} = -\frac{1}{\sqrt{2}} \left[\kappa_{q_u} \bar{q_u} q_u h + \kappa_{q_d} \bar{q_d} q_d h + \kappa_{q_u} v \bar{q_u} q_u + \kappa_{q_d} v \bar{q_d} q_d \right] .$$

Where $q_u = u, c, t$, $q_d = d, s, b$, $\kappa_{q_u} = \sqrt{2} m_u / v$ and $\kappa_{q_d} = \sqrt{2} m_d / v$. The diagonalization of the mass matrix removes any mixing between the mass eigenstates and the weak eigenstates in the fermion mass basis. Another outcome of this mixing between the weak eigenstates and the mass eigenstates is on the charged-current

weak interaction. We encounter:

$$(\bar{u}_1, \bar{u}_2, \bar{u}_3)_L \gamma^\mu \begin{pmatrix} d_1 \\ d_2 \\ d_3 \end{pmatrix}_L = (\bar{u}, \bar{c}, \bar{t})_L U_L^\dagger D_L \gamma^\mu \begin{pmatrix} d \\ s \\ b \end{pmatrix}_L .$$

We define, $V \equiv U_L^\dagger D_L$, this matrix is also known as the CKM matrix (Cabibo (C), Kobayashi (K) and Maskawa (M)).

1.1.8 Flavor Symmetry and GIM Mechanism

Flavor refers to different types of charged fermions. Conservation of the flavor quantum number plays a crucial role in restricting several interactions at tree level in the SM. Every charged lepton and quark consists of a flavor quantum number, which is conserved in every tree level neutral SM interactions. For the charged interactions, due to CKM mixing, we see flavor changing charged interactions involving the $W^\pm$ boson and quarks.

Let's consider the following decays, $\mu^- \to e^- \bar{\nu}_e \nu_\mu$, here μ^- carries a muon flavor quantum number L_μ= 1, similarly e^- and $\bar{\nu_e}$ carries an electron flavor quantum number $L_e = 1$ and -1 respectively. For this decay process, on the LHS we have $L_\mu = 1$, $L_e = 0$ and on the RHS, we have $L_e = 1(e^-) + -1(\bar{\nu}_e) = 0$ and $L_\mu = 1(\nu_\mu)$. Hence the flavor quantum number remains conserved for this muon decay. This flavor symmetry forbid processes like, $\mu \to e\gamma$, $\tau \to \mu\gamma$, at tree-level in the SM.

We have also witnessed this symmetry in the previous section with the Higgs boson interactions with the fermions. The diagonalization of the mass matrix of the quarks removed any possible off-diagonal interaction couplings or in other words flavor changing neutral Higgs (FCNH) couplings at tree level for quarks. For leptons there weren't any either.

Another interesting feature of the SM is that, even at one loop level these FCNH interactions are suppressed due to the GIM mechanism, postulated by Glashow, Iliopoulos and Maiani in the early 1970s [35]. This mechanism led to the prediction of the charm quark. GIM mechanism was introduced to explain the suppression of $K_L^0 \to \mu^+\mu^-$ decays in the SM. At that time only u, d, and s quarks were known, with only $u \Leftrightarrow d'$ transition, where d' was introduced as a mixed state of d and s quarks, given as,

$$d' = d\cos\theta_c + s\sin\theta_c,$$

here θ_c is the quark mixing angle, also known as the Cabibo angle [20]. In the SM the Feynman diagram responsible for, $K_L^0 \to \mu^+\mu^-$ transition is given in Fig. **1.4**, with only contribution coming from the u quarks. That prediction was in excess of the observed [20, 35],

$$\frac{\Gamma(K_L^0 \to \mu^+\mu^-)}{\Gamma(K_L^0 \to \text{allmodes})} = 2.6 \times 10^{-9}.$$

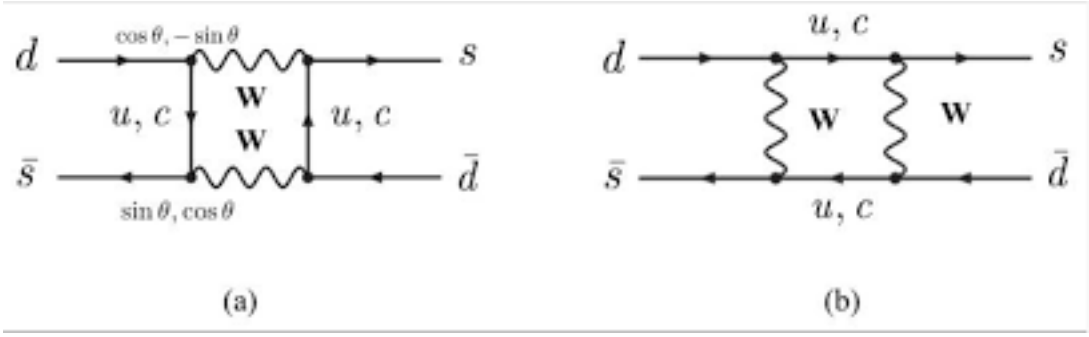

Figure 1.4: Two contributions to $K_L^0 \to \mu^+\mu^-$.

But, with the introduction of a charm quark, the two diagrams destructively interfere and suppress each other's contributions. In the modern interpretation of GIM mechanism, Cabibbo angle is a part of the CKM mixing matrix. Following,

the Wolfenstein parametrization of the CKM mixing matrix [36], we get,

$$\sum_{j}^{3} V_{ij} V_{jk}^{*} = 0\,. \tag{1.35}$$

This particular property of the CKM, also known as the CKM unitarity [37], suppresses the flavor violating decays like $t \to ch^0$ or $t \to c\gamma$ at the one-loop level in the SM. Let's elaborate on this with an example of $t \to ch^0$ decay. The Feynman diagrams contributing to this channel from the SM is shown in Fig. **1.5**.

If we assume $m_d = m_s = m_b$, then the scattering amplitudes for the three diagrams can be written as,

$$\mathcal{M} = \mathcal{M}_d + \mathcal{M}_s + \mathcal{M}_b \propto V_{td} V_{dc}^{*} + V_{ts} V_{sc}^{*} + V_{tb} V_{bc}^{*}\,.$$

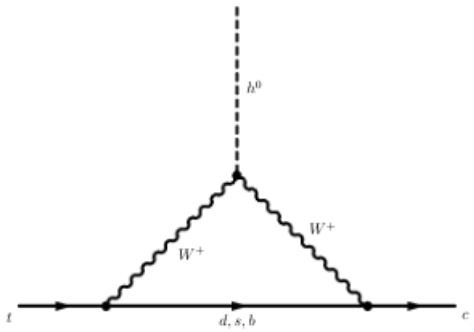

Figure 1.5: One loop contributions for $t \to ch^0$ decay.

Following Eq 1.35, $\mathcal{M} \sim 0$. Since, $m_b \neq m_s \neq m_d$, the decay width for $t \to ch^0 \propto \mathcal{O}(10^{-14})$ [38–40], in the SM.

1.1.9 Recent Flavor Anomalies

In the SM, $W \to e\nu_e$ and $W \to \mu\nu_\mu$ decays or $Z \to e^+e^-$ and $Z \to \mu^+\mu^-$ decays have the same probability. This is termed as the Lepton Flavor Universality

(LFU). Several experimental collaborations like the BABAR, BELLE, LHCb have been testing LFU, especially in the B meson decays. Global analysis of B decays hint at a violation of LFU.

For $b \to s\ell^+\ell^-$ decays, the ratio of $\mathcal{B}$ branching fractions of two different flavor final states,

$$R_K \equiv \frac{\mathcal{B}(B^+ \to K^+\mu^+\mu^-)}{\mathcal{B}(B^+ \to K^+e^+e^-)} \qquad R_{K^{*0}} \equiv \frac{\mathcal{B}(B^0 \to K^{*0}\mu^+\mu^-)}{\mathcal{B}(B^0 \to K^{*0}e^+e^-)}, \tag{1.36}$$

is $\simeq 1$ [41], if LFU holds. However the current measurements of R_K by LHCb is [42],

$$R_K = 0.745^{+0.09}_{-0.07} \pm 0.036,$$

which deviates from the SM prediction by 2.6σ. $R_{K^{*0}}$ is in good agreement with the SM for most part, but shows some deviations in the low q^2 regions. The current measurements for $R_{K^{*0}}$ are [43],

$$R_{K^{*0}} = \begin{cases} 0.66^{+0.11}_{-0.07} \pm 0.03 : 0.045 \leq q^2 \leq 1.1 \,, \mathrm{GeV}^2/\mathrm{c}^4 \\ 0.69^{+0.11}_{-0.07} \pm 0.05 : 1.1 \leq q^2 \leq 6 \ \mathrm{GeV}^2/\mathrm{c}^4. \end{cases}$$

Flavor anomalies are also present in the charge current transitions, especially in $b \to c\ell\nu_\ell$ decays. The rates of B meson decays to τ and μ is expected to be different, because of the large $\tau - \mu$ mass difference. To measure and test LFU, the following observables are measured,

$$R_D \equiv \frac{\mathcal{B}(B \to D\tau\nu_\tau)}{\mathcal{B}(B \to D\ell\nu_\ell)} \qquad R_{D^{(*)}} \equiv \frac{\mathcal{B}(B \to D^{(*)}\tau\nu_\tau)}{\mathcal{B}(B \to D^{(*)}\ell\nu_\ell)}\,, \tag{1.37}$$

with $\ell = e, \mu$. The measured values of R_D and $R_{D^{(*)}}$ exceeds the SM expectations [44] by 2.3 and 3.0 standard deviations, resulting in a combined deviation of

3.8σ [45, 46],

$$\begin{aligned} R_D &= 0.407 \pm 0.039 \pm 0.024(\text{exp}), \qquad R_D = 0.299 \pm 0.003,\ (\text{th})\,, \\ R_{D^{(*)}} &= 0.304 \pm 0.013 \pm 0.007(\text{exp}), \qquad R_{D^*} = 0.258 \pm 0.005\ (\text{th}). \end{aligned}$$

All of these deviations suggests that the flavor symmetry of the SM is not an exact symmetry of nature.

1.2 Introduction to General Two Higgs Doublet Model

The minimal scalar sector of the SM, with only one $\text{SU}(2)_L$ doublet, has been extremely successful in explaining most of the experimental results. At the same time there are some tensions; like the flavor anomalies of the previous section, no particle candidate for dark matter, and the excessive CP violation in the Universe (matter dominated Universe) to name a few. An extended scalar sector with one additional Higgs doublet can provide the following:

(i) Modifications of 125 GeV Higgs boson properties

(ii) New scalar states

(iii) Extra sources of CP violation.

One of the key modifications is the introduction of tree-level off-diagonal couplings in the Yukawa sector which leads to an enhancement in the flavor changing neutral Higgs (FCNH) interactions.

1.2.1 Modified Higgs Potential

The most general gauge invariant Higgs potential for the two Higgs doublet extension of the SM is given by [47],

$$\begin{aligned} V_{THDM} &= m_{11}^2\phi_1^\dagger\phi_1 + m_{22}^2\phi_2^\dagger\phi_2 - [m_{12}^2\phi_1^\dagger\phi_2 + \text{H.c.}] \\ &+ \frac{1}{2}\lambda_1(\phi_1^\dagger\phi_1)^2 + \frac{1}{2}\lambda_2(\phi_2^\dagger\phi_2)^2 + \lambda_3(\phi_1^\dagger\phi_1)(\phi_2^\dagger\phi_2) + \lambda_4(\phi_1^\dagger\phi_2)(\phi_1^\dagger\phi_2) \\ &+ \left\{\frac{1}{2}\lambda_5(\phi_1^\dagger\phi_2)^2 + [\lambda_6(\phi_1^\dagger\phi_1) + \lambda_7(\phi_2^\dagger\phi_2)]\phi_1^\dagger\phi_2 + \text{H.c.}\right\}. \end{aligned}$$

Here ϕ_1 and ϕ_2 denote complex Y = 1, $\text{SU}(2)_L$ doublet scalar fields. In general, $m_{12}^2, \lambda_{5,6,7}$ can be complex, where as the rest of the couplings are real. The doublets can be expressed as,

$$\phi_1 = \begin{pmatrix} \phi_1^+ \\ \phi_1^0 \end{pmatrix}, \qquad \phi_2 = \begin{pmatrix} \phi_2^+ \\ \phi_2^0 \end{pmatrix}.$$

After electroweak symmetry breaking (EWSB), there are two possibilities, (I) Both the doublets have a non zero VEV, v_i (i = 1, 2), and, (II) Only one has a non zero VEV, v = 246.1 GeV. Case I, is the Yukawa basis [47] and Case II is the Higgs basis as used in the Ref. [48]. Under case I the doublets are defined as,

$$\phi_1 = \begin{pmatrix} \phi_1^+ \\ \frac{1}{\sqrt{2}}(\phi_1^0 + v_1 + i\text{Im}\phi_1^0) \end{pmatrix}, \qquad \phi_2 = \begin{pmatrix} \phi_2^+ \\ \frac{1}{\sqrt{2}}(\phi_2^0 + v_2 + i\text{Im}\phi_2^0) \end{pmatrix}.$$

Here $v_1^2 + v_2^2 = v^2$, are the two VEVs ($\tan\beta \equiv v_2/v_1$). Which also satisfies:

$$\begin{pmatrix} v_1 \\ v_2 \end{pmatrix} = \begin{pmatrix} \cos\beta & -\sin\beta \\ \sin\beta & \cos\beta \end{pmatrix} \begin{pmatrix} v \\ 0 \end{pmatrix}. \qquad \textbf{(1.38)}$$

We perform a rotation by an angle β to diagonalizes the mass matrix of ϕ^+ and Imϕ^0,

$$\begin{pmatrix} \phi_1^+ \\ \phi_2^+ \end{pmatrix} = \begin{pmatrix} \cos\beta & -\sin\beta \\ \sin\beta & \cos\beta \end{pmatrix} \begin{pmatrix} G^+ \\ H^+ \end{pmatrix},$$
$$\begin{pmatrix} \mathrm{Im}\,\phi_1^0 \\ \mathrm{Im}\,\phi_2^0 \end{pmatrix} = \begin{pmatrix} \cos\beta & -\sin\beta \\ \sin\beta & \cos\beta \end{pmatrix} \begin{pmatrix} G^0 \\ A^0 \end{pmatrix}.$$

To diagonalize the mass matrix of the real parts, ϕ_1^0 and ϕ_2^0 we rotate the mass matrix by an angle α,

$$\begin{pmatrix} \phi_1^0 \\ \phi_2^0 \end{pmatrix} = \begin{pmatrix} \cos\alpha & -\sin\alpha \\ \sin\alpha & \cos\alpha \end{pmatrix} \begin{pmatrix} H^0 \\ h^0 \end{pmatrix}. \tag{1.39}$$

After EWSB we have five scalar states, two neutral scalars H^0 and h^0, two charged scalars $H^\pm$ and one pseudoscalar A^0. Whereas, $G^\pm$ and G^0 are the three Goldstone bosons, that are eaten up by $W^\pm$ and Z^0. With these rotations we can express the two doublets [47],

$$\phi_1 = \begin{pmatrix} G^+ c_\beta - H^+ s_\beta \\ \frac{1}{\sqrt{2}}(H^0 c_\alpha - h^0 s_\alpha + v c_\beta + i G^0 c_\beta - i A^0 s_\beta) \end{pmatrix}, \tag{1.40}$$

$$\phi_2 = \begin{pmatrix} G^+ s_\beta + H^+ c_\beta \\ \frac{1}{\sqrt{2}}(H^0 s_\alpha + h^0 c_\alpha + v s_\beta + i G^0 s_\beta + i A^0 c_\beta) \end{pmatrix}, \tag{1.41}$$

here $s_{\beta,\alpha} = \sin\beta,\ \sin\alpha$, and $c_{\beta,\alpha} = \cos\beta,\ \cos\alpha$. We can derive the mass matrix by substituting Eq 1.40 and Eq 1.41 in the Higgs potential, V_{THDM}. m_{11}^2 and m_{22}^2

can be eliminated using the potential minimum conditions given as [47],

$$m_{11}^2 = m_{12}^2 t_\beta - \frac{1}{2}\left\{\lambda_1 c_\beta^2 + \lambda_{345} s_\beta^2 + 3\lambda_6 s_\beta c_\beta + \lambda_7 s_\beta^2 t_\beta\right\}, \quad (\mathbf{1.42})$$

$$m_{22}^2 = m_{12}^2 t_\beta^{-1} - \frac{1}{2}\left\{\lambda_2 s_\beta^2 + \lambda_{345} c_\beta^2 + 3\lambda_7 s_\beta c_\beta + \lambda_6 c_\beta^2 t_\beta^{-1}\right\}. \quad (\mathbf{1.43})$$

Using the above conditions the mass matrix for the charged scalar and pseudoscalar [a],

$$\begin{pmatrix} m_{H^\pm}^2 \\ m_A^2 \end{pmatrix} = \begin{pmatrix} \left\{\frac{1}{2}(\lambda_4+\lambda_5)v^2 + \frac{m_{12}^2}{s_\beta c_\beta}\right\} \\ \frac{m_{12}^2}{s_\beta c_\beta} - \lambda_5 v^2 \end{pmatrix}. \quad (\mathbf{1.44})$$

Following the same ideology the mass matrix for the neutral scalars (h^0 and H^0) is given as,

$$\mathcal{M}^2 = \begin{pmatrix} \lambda_1 v^2 c_\beta^2 + m_{12}^2 t_\beta & -m_{12}^2 + \lambda_{345} v^2 c_\beta s_\beta \\ -m_{12}^2 + \lambda_{345} v^2 c_\beta s_\beta & \frac{m_{12}^2}{t_\beta} + \lambda_2 v^2 s_\beta^2 \end{pmatrix}, \quad (\mathbf{1.45})$$

with $\lambda_{345} = \lambda_3 + \lambda_4 + \lambda_5$. This matrix can be diagonalized by performing a rotation of α, this gives the mass terms for the neutral scalars m_h^2 and m_H^2 to be,

$$\begin{aligned} m_H^2 &= s_\alpha^2\left\{(m_A^2+\lambda_5 v^2)c_\beta^2 + \lambda_2 v^2 s_\beta^2\right\} + c_\alpha^2\left\{(m_A^2+\lambda_5 v^2)s_\beta^2 + \lambda_1 v^2 c_\beta^2\right\} \\ &- c_\alpha s_\alpha s_{2\beta}\left\{m_A^2 - (\lambda_3+\lambda_4)v^2\right\}, \end{aligned}$$

$$\begin{aligned} m_h^2 &= c_\alpha^2\left\{(m_A^2+\lambda_5 v^2)c_\beta^2 + \lambda_2 v^2 s_\beta^2\right\} + s_\alpha^2\left\{(m_A^2+\lambda_5 v^2)s_\beta^2 + \lambda_1 v^2 c_\beta^2\right\} \\ &- c_\alpha s_\alpha s_{2\beta}\left\{m_A^2 - (\lambda_3+\lambda_4)v^2\right\}. \end{aligned}$$

Figure. **1.6** (a), shows how the Higgs potential would look like in gTHDM in the

[a] For most of our analysis we have kept $\lambda_6 = \lambda_7 = 0$, this is also related to preserving Z_2 symmetry,which is keeping the Higgs potential invariant under the following transformations, $\phi_1 \to \phi_1$ and $\phi_2 \to -\phi_2$

$[\phi_1^0, \phi_2^0]$ plane. We can see multiple bumps, which are the signs of non zero VEVs. In Fig. **1.6** (b) we set $\phi_2 \to 0$, and observe that the Higgs potential converges to the SM Higgs potential.

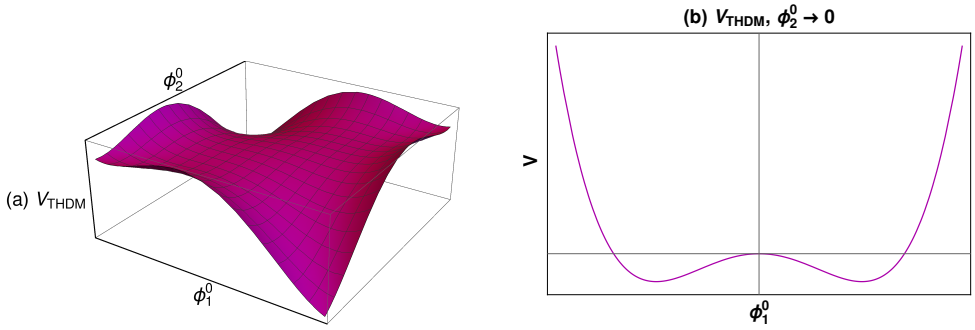

Figure 1.6: Higgs potential in gTHDM, with $m_H = m_A = m_{H^\pm} = 300$ GeV,$\cos\beta - \alpha = 0.1$, and $\lambda_6 = \lambda_7 = 0$ is shown in (a) and the Higgs potential when ϕ_2^0 is very close to 0 is shown in (b).

In the Higgs basis, only one doublet takes a VEV we can rewrite the Higgs potential as [48],

$$\begin{aligned} V_{THDM} &= M_{11}^2 \Phi_1^\dagger \Phi_1 + M_{22}^2 \Phi_2^\dagger \Phi_2 - [M_{12}^2 \Phi_1^\dagger \Phi_2 + \text{H.c.}] \\ &+ \frac{1}{2}\Lambda_1 (\Phi_1^\dagger \Phi_1)^2 + \frac{1}{2}\Lambda_2 (\Phi_2^\dagger \Phi_2)^2 + \Lambda_3 (\Phi_1^\dagger \Phi_1)(\Phi_2^\dagger \Phi_2) + \Lambda_4 (\Phi_1^\dagger \Phi_2)(\Phi_1^\dagger \Phi_2) \\ &+ \left\{ \frac{1}{2}\Lambda_5 (\Phi_1^\dagger \Phi_2)^2 + [\Lambda_6 (\Phi_1^\dagger \Phi_1) + \Lambda_7 (\Phi_2^\dagger \Phi_2)] \Phi_1^\dagger \Phi_2 + \text{H.c.} \right\}. \end{aligned}$$

With doublets Φ_i defined as,

$$\Phi_1 = \begin{pmatrix} G^+ \\ \frac{1}{\sqrt{2}}(H_1 + v + iG^0) \end{pmatrix}, \qquad \Phi_2 = \begin{pmatrix} H^+ \\ \frac{1}{\sqrt{2}}(H_2 + iA^0) \end{pmatrix}.$$

An important observation here is that in this basis $\tan\beta$ is either 0 or ∞, or in other words not defined. Which makes $\tan\beta$ an unphysical parameter in the gTHDM [49]. Hence we won't be using this as a part of our independent parameters.

1.2.2 Corrections to the Yukawa Sector and FCNH

In the gTHDM we can express the interaction of the doublets with the fermions in the most generic basis as,

$$\mathcal{L} = \tilde{Y}^k_{ij}\bar{u}_{iR}\tilde{\phi}^\dagger_k Q_{jL} + Y^k_{ij}\bar{d}_{iR}\phi^\dagger_k Q_{jL} + \text{H.c.}\,. \tag{1.46}$$

Where i, j are sum over different flavors of charged fermions and k is the sum over both the doublets. Here we have two Yukawa matrices, Y^1 and Y^2. If we diagonalize any one matrix through a rotation of θ to mass basis Y'^k,

$$Y'^k = R(\theta)Y^k R^\dagger(\theta).$$

However, there is no symmetry in the gTHDM that could force both the matrices to diagonalize simultaneously.

We perform a rotation of angle β on Y^1 and Y^2 to put them in the mass basis from the generic basis i.e.,

$$\begin{pmatrix} Y^1 \\ Y^2 \end{pmatrix} = \begin{pmatrix} \cos\beta & -\sin\beta \\ \sin\beta & \cos\beta \end{pmatrix} \begin{pmatrix} \kappa^F \\ \rho^F \end{pmatrix}\,. \tag{1.47}$$

The κ^F matrices are diagonal and fixed by fermion masses, $\kappa^F = \sqrt{2}m_F/v$ with $v \simeq 246$ GeV, while ρ^F matrices are in general not diagonal. With a bit of algebra, we get the following Lagrangian [50],

$$\begin{aligned}\frac{-1}{\sqrt{2}}\sum_{F=U,D,E}\bar{F}\Big\{\left[\kappa^F s_{\beta-\alpha} + \rho^F c_{\beta-\alpha}\right]h^0 + \left[\kappa^F c_{\beta-\alpha} - \rho^F s_{\beta-\alpha}\right]H^0 - i\,\text{sgn}(Q_F)\rho^F A^0\Big\}P_R F \\ -\bar{U}\left[V\rho^D P_R - \rho^{U\dagger}V P_L\right]DH^+ - \bar{\nu}\left[\rho^E P_R\right]EH^+ + \text{H.c.}\,.\end{aligned} \tag{1.48}$$

Here $s_{(\beta-\alpha)} = \sin(\beta-\alpha)$, $c_{(\beta-\alpha)} = \cos(\beta-\alpha)$, and $P_{L,R} = (1 \mp \gamma_5)/2$. U, D and E stands for up-type quarks, down-type quarks and charge leptons, respectively. We have derived the above interaction Lagrangian without putting any symmetries to restrict the interaction of the two doublets with the fermions. An outcome of that is the presence of tree-level FCNH couplings coming from off-diagonal terms in the ρ^F matrix. This is in clear contradiction with the flavor symmetry of the SM and as a result a natural flavor conservation (NFC) scheme was proposed by Pashchos-Glashow-Weinberg [51]. In the NFC scheme, we impose some additional symmetries to avoid the mixing of the two doublets in the Yukawa sector. Following the NFC scheme, we have Type I, Type II, Lepton Specific and Lepton Flipped models of the THDM. Table. **1.6**, describes which doublet is allowed to interact with the up quarks, down quarks and charged leptons following [52]. In Table. **1.7**, we present the effective factors multiplied to κ^F. All the off-diagonal terms of ρ^F are zero in these models.

Model	u_R^i	d_R^i	e_R^i
Type I	ϕ_2	ϕ_2	ϕ_2
Type II	ϕ_2	ϕ_1	ϕ_1
Lepton-specific	ϕ_2	ϕ_2	ϕ_1
Flipped	ϕ_2	ϕ_1	ϕ_2

Table 1.6: NFC Models in 2HDM.

Yukawa	Type I	Type II	Lepton-Specific	Flipped
κ_h^u	$\cos\alpha/\sin\beta$	$\cos\alpha/\sin\beta$	$\cos\alpha/\sin\beta$	$\cos\alpha/\sin\beta$
κ_h^d	$\cos\alpha/\sin\beta$	$-\sin\alpha/\cos\beta$	$\cos\alpha/\sin\beta$	$-\sin\alpha/\cos\beta$
κ_h^ℓ	$\cos\alpha/\sin\beta$	$-\sin\alpha/\cos\beta$	$-\sin\alpha/\cos\beta$	$\cos\alpha/\sin\beta$

Table 1.7: Yukawa Couplings of SM Higgs in NFC models.

However, these versions of the THDM have struggled to simultaneously explain the deviations in the measurements of R_D and R_{D^*}. In addition, they have also failed to explain the deviations in the low q^2 region for R_K and $R_{K^{*0}}$. With the current constraints, even the gTHDM struggles to explain all of the above anomalies, but it does a better job as suggested in [53]. Apart from these anomalies, the SM flavor symmetry still holds in most of the scenarios to current experimental precision. One way to suppress this tree-level flavor changing couplings in the gTHDM is by choosing $\cos\beta - \alpha \sim 0$, which will remove the off-diagonal interactions for h^0, which is commonly identified with the SM Higgs boson; this is known as the decoupling limit [47]. A correct definition of the decoupling limit is to decouple the additional Higgs scalar from interacting with the vector bosons at tree level. In the gTHDM the Higgs to vector boson coupling is given as [47],

$$g_{hVV} = g_{SM}\sin(\beta-\alpha), \quad g_{HVV} = g_{SM}\cos(\beta-\alpha). \tag{1.49}$$

Where, V = $W^{\pm}$, Z and $g_{SM} = g$ from Eq 1.28. g_{hVV} is the h^0 coupling to vector bosons in the gTHDM, and g_{HVV} is the H^0 coupling to the vector bosons. For the rest of this dissertation, we will keep $\cos(\beta-\alpha) \sim 0$. Complementary to this is that the off-diagonal terms for H^0 survives because of $\rho^F \sin\beta - \alpha$ and for A^0 there is no factor of $\sin(\beta-\alpha)$ or $\cos\beta-\alpha$ with the ρ^F. In this dissertation, we have performed collider phenomenological studies for $\phi^0 \to \tau\mu$ with $\phi^0 = A^0, H^0$ and we have kept $m^0_H, m^0_A > m^0_h$, which suppresses the production cross-section of both the heavier states, we present a detailed study in Chapter 3, with our predictions. Chapter 4 is for the FCNH with the third generation of quarks, i.e., $t \to ch^0$.

Chapter 2

Discovery Channels and Analysis Strategies

The main goal of this dissertation is to present the discovery reach for two kinds of FCNH channels, i.e., $t \to ch^0$, and $\phi^0 \to \tau\mu$. Here t = top quark, c = charm quark, and h^0 is the SM-Higgs, whereas ϕ^0 refers to the Heavy scalar (H^0), and pseudoscalar (A^0) from the gTHDM. In Chapter 3, we discuss the discovery reach for $\phi^0 \to \tau\mu$ in much more detail. In Chapter 4, we present the discovery reach of $t \to ch^0$ for two different SM-Higgs decay channels.

2.1 Discovery Channels

2.1.1 Motivation for $\phi^0 \to \tau\mu$

In 2015 CMS [54] reported a 2.4σ excess in the $h^0 \to \tau\mu$ channel, sparking our interest to look for this FCNH channel. Unfortunately, the excess disappeared with the Run-2 data [55], and CMS put a limit on the branching fraction $\mathcal{B}(h^0 \to \tau\mu) < 0.25\%$ with 1σ standard deviation. This can be treated as a blessing in disguise, if you study this decay mode with the additional Higgs scalars from gTHDM. In the decoupling limit, $\cos(\beta-\alpha) \simeq 0$ (which means $\sin(\beta-\alpha) \simeq 1$) so the off-diagonal terms in the ρ^F matrix for H^0 survives, which can be confirmed from the following interaction Lagrangian:

$$-\sqrt{2}\mathcal{L}_{\tau\mu} = \bar{\psi}_\mu \left\{ \rho_{\tau\mu} \cos(\beta-\alpha) h^0 + \rho_{\tau\mu} \sin(\beta-\alpha) H^0 - i\gamma_5 \rho_{\tau\mu} A^0 \right\} P_R \psi_\tau + \text{H.c.}, \tag{2.1}$$

here $P_R = (1+\gamma_5)/2$.

The off diagonal terms for h^0 almost vanishes, which explains the null results

from the CMS experiment. In Chapter 3, we present a detailed study of $\phi^0 \to \tau\mu$ for $150 < m_H, m_A < 500$ GeV, where $m_H(m_A)$ are the mass of scalar (pseudoscalar). We keep all the experimental constraints coming from $\tau \to \mu\gamma$, $\mu \to e\gamma$ and from the B-mixing measurements to choose an experimentally favourable parameter space.

2.1.2 Motivation for $t \to ch^0$

In Sec 1.1.8, I mentioned that $t \to ch^0$ is highly suppressed at 1-Loop level because of the CKM unitarity, but the current limits from the ATLAS-experiment [56],

$$\mathcal{B}(t \to ch^0) \leq 1.1 \times 10^{-3}, \tag{2.2}$$

is nearly 10 orders of magnitude higher than the theoretical estimate from the SM, which is of the order $\mathcal{O}(10^{-14})$ [38–40]. The gTHDM extension of the SM has tree-level flavor off-diagonal Yukawa terms in the ρ^F matrix, which can enhance this decay at tree level and can come close to the experimental limits. We can write the interaction Lagrangian for this process [50], from Eq 1.48, as,

$$-\sqrt{2}\mathcal{L}_{tch} = \left\{\rho_{tc}\cos(\beta-\alpha)\bar{\psi}_c P_R \psi_t h^0 + \rho_{ct}\cos(\beta-\alpha)\bar{\psi}_t P_R \psi_c\right\} + \text{H.c.}\,.$$

Another experimental motivation comes from the flavor anomalies in the $R(D)$ and $R(D^*)$ measurements as discussed in Sec.1.1.9. These flavor anomalies suggest that there might be some extra flavor violation present in nature that is absent in the SM. Even the NFC models that we discussed in Sec 1.2.2 haven't been able to provide an explanation for these anomalies, as pointed in Ref. [57]. A more unconstrained Yukawa sector is required and the gTHDM seems to provide that. As pointed in Ref. [53], that for $\rho_{tc} \simeq +1$ and non zero $\rho_{\tau\tau}$ with $m_H^+ = 500$ GeV,

the current measurements of $R(D)$ and $R(D^*)$ anomalies can be explained up to 1σ as shown in Fig. **2.1**.

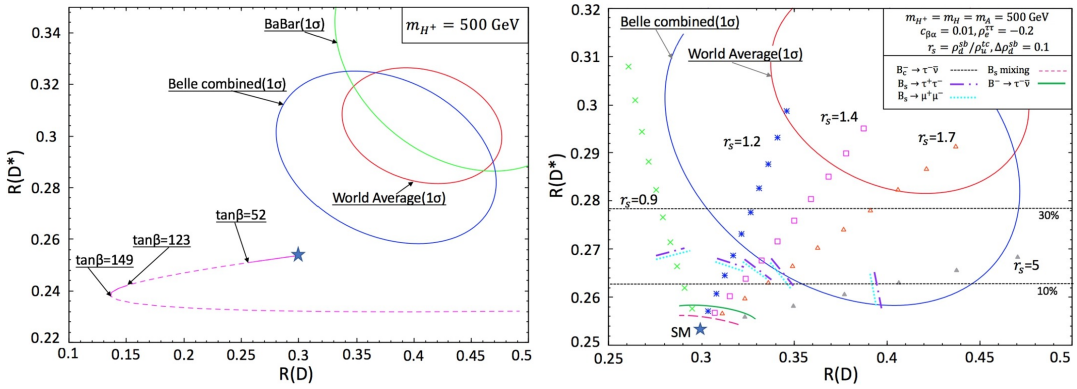

Figure 2.1: The predicted values for $R(D)$ and $R(D*)$ from 2HDM-II (right) and (left) from 2HDM-III for different values of $r_\tau = |\rho^{\mu\tau}/\rho^{e\tau}| = 1.6$(orange triangle),2(cyan quadrangle) 2.7(open pink quadrangle) and 4(green×)
Iguro. et. al (Nucl. Phys. B. 2017.10.014).

Interestingly, the SM satisfies all the Sakharov conditions [58] but not in the amount required for a successful electroweak baryogenesis. The electroweak baryogenesis is one of the models that can potentially explain the matter-antimatter asymmetry of the Universe. The Sakharov conditions are:

1) C and CP violation

2) Baryon number violations

3) Interactions out of thermal equilibrium.

A detailed discussion on how the SM satisfies the Sakharov conditions is out of the scope of this dissertation, please see Ref. [59] for more details. We will briefly discuss one requirement: CP violation in the SM. In the SM, CP violation comes from the CKM phase [59, 60]. CP violation was first observed in neutral kaon (K^0) decays [61]. From Table. **1.2** we get $K^0 = d\bar{s}$, and it was pointed out by

Gell-Mann and Pais that K^0 is not an eigenvector of CP [62], i.e.

$$P|K^0\rangle = -|K^0\rangle\,, \tag{2.3}$$

$$C|K^0\rangle = |\bar{K}^0\rangle\,, \tag{2.4}$$

$$CP|K^0\rangle = -|\bar{K}^0\rangle\,. \tag{2.5}$$

They defined two CP eigenstates by linear combination of K^0 and $\bar{K}^0$, which is given as [9],

$$|K_1\rangle = \frac{1}{\sqrt{2}}(|K^0\rangle - |\bar{K}^0\rangle), \qquad (\mathrm{CP-even}) \tag{2.6}$$

$$|K_2\rangle = \frac{1}{\sqrt{2}}(|K^0\rangle + |\bar{K}^0\rangle), \qquad (\mathrm{CP-odd})\,, \tag{2.7}$$

K_1 decays to two pions and the K_2 decays to three pions. Both the K_1 and K_2 were observed in 1956 at Brookhaven National Laboratory [63], with K_2 having a longer lifetime than K_1. In 1964, Cronin and Fitch counted the number of events with three pion decays. They used the difference in the lifetimes of the two kaons to setup their experiment. After performing their counting experiment they found that out of 22700 three pion events there were 57 two pion events [61]. This was a clear indication of CP-violation in the SM, with CKM acting as the source. But CKM just cannot provide enough CP-violation required to explain the matter-antimatter asymmetry [59].

In gTHDM, the extra top Yukawa couplings, especially ρ_{tt} and ρ_{tc}, can provide additional sources of CP violation. In addition to CP violation, ρ_{tc} can also drive the electroweak baryogenesis as mentioned in Ref. [64]. Figure. **2.2** presents their results, which shows the impact on Y_B from ρ_{tt} and ρ_{tc}, where Y_B is:

$$Y_B = \frac{n_B}{s}\,, \tag{2.8}$$

here n_B is the baryon number density and s is the entropy density. Y_B^{obs} is the present value of the baryon number density as observed by Planck, $Y_B^{obs} = 8.59 \times 10^{-11}$ [65]. They showed that for small values of ρ_{tt}, ρ_{tc} of $\mathcal{O}(1)$ can drive electroweak baryogenesis as shown in Fig. **2.2**.

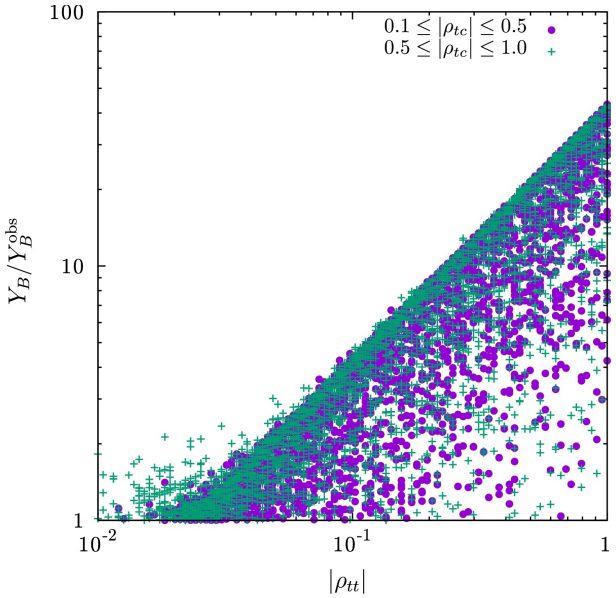

Figure 2.2: Impact of ρ_{tt} and ρ_{tc} on the ratio of Y_B/Y_B^{obs} Fuyuto. et. al (Phys. Lett. B. 2017.11.073).

In light of collider phenomenology, studying ρ_{tc} through the $t \to ch^0$ decay is quite promising. In Chapter 4 we present a collider study for this decay channel for two different h^0 decays, namely WW^* and $\tau^+\tau^-$.

2.2 Analysis Tools and Strategies

2.2.1 Integration Method

The biggest challenge is calculating the cross-section of the signal and the backgrounds. Our discovery channels have 4-8 outgoing particles, which gives us an integral of dimensions ranging from 10 to 22. Performing a definite integral

analytically is nearly impossible. We use Monte-Carlo (MC) [66] integration to perform these multidimensional integrals. MC uses random numbers generated from a probability distribution to estimate the value of the definite integral. There are different ways to sample these random numbers, to name a few,

- Uniform sampling [67],
- Stratified Sampling [68],
- Importance Sampling [69].

MC integration calculates the integrating function for a set of random numbers sampled using one of the above ways. It tries to estimate the correct value of the integral with each iteration, by improving the sampling of random numbers and minimizing the variance.

Consider a multidimensional integral,

$$I = \int_{\Omega} f(x) dx \,, \tag{2.9}$$

where Ω is an N-dimensional hyper volume. The integral above takes an expectation value of E for the random variable X, which is an N-dimensional random variable with a uniform distribution. The Monte-Carlo expectation of the integral is [66]:

$$E = \frac{1}{n} \sum_{i=1}^{n} f(x_i) \,, \tag{2.10}$$

here x_i is an independent set of random numbers taken from X and n is the total number of sets. By the law of large numbers, the larger the number of sets the

better the estimate. The variance for the above E is [66],

$$\sigma^2(f) = \int (f(x) - I)^2 dx \approx \frac{1}{n} \sum_{i=1}^{n} \left(f\left(x_i\right) - E\right)^2 = \frac{1}{n} \sum_{i=1}^{n} f\left(x_i\right)^2 - E^2 = \widehat{\sigma^2(f)}\,. \tag{2.11}$$

An important thing to note here is that the error $= \sqrt{\sigma^2(f)} \propto n^{-1/2}$, not on the dimension N of the integral, which is the biggest advantage of using MC methods for multidimensional integrals over the other numerical integration as the scale of their error increases with the dimension of integrals.

For variance reduction, we use an algorithm known as VEGAS, which performs MC integration and uses importance sampling for reducing the variance iteratively. The VEGAS algorithm was introduced by G.P Lepage in the following paper [70] in 1978. It is an adaptive multidimensional MC integration algorithm, which samples points from a probability distribution estimated using the integrating function. The main idea is to sample those random numbers where the contribution from the function is concentrated the most.

The VEGAS algorithms approximate the probability distribution function (pdf) by making several estimates of the function $f(x)$ inside the integration domain and then creates a distribution. This estimated distribution is used as an input for the estimation of the pdf for the next iteration. Asymptotically this procedure converges to the desired distribution, which in turn gives a pretty accurate estimate of the integral.

2.2.2 Phase Space Integration and Event Generation

For our analysis, our integral for the differential cross-section takes the following form [26, 34],

$$d\sigma = \frac{|\mathcal{M}|^2}{2E_a 2E_b |v_a - v_b|} d\Phi_N\,, \tag{2.12}$$

where $d\sigma$ is the differential cross-section for any particle physics scattering/production process. Here $|\mathcal{M}|^2$ carries the information of the particle interactions, couplings, and propagators involved in the process. $|\mathcal{M}^2|$ is the square of the scattering amplitude of initial colliding particles to final state particles. E_a and E_b are the energies of the colliding particles, and $d\Phi_N$ is the phase space integral given as:

$$d\Phi_N(p_\alpha, p_1, p_2, ...p_N) = \prod_i^N \frac{d^3p_i}{(2\pi)^3 2E_i}(2\pi)^4\delta^4(p_a + p_b - \sum_1^N p_i)\,, \tag{2.13}$$

as mentioned above, we are dealing with a multidimensional integral. We perform MC integration using the VEGAS algorithm from GP Lepage, implemented in FORTRAN. We rewrite the momentum of each final state particle in terms of the random numbers between 0 and 1. Our next step is known as the phase space reduction. We can rewrite an N-dimensional phase space integral as:

$$d\Phi_N(p_\alpha, p_1, p_2, .., p_N) = (2\pi)^{-1} d\Phi_{N-1}(p_\alpha, p_{12}, .., p_N) \times d\Phi_{12}(p_{12}, p_1, p_2) dM_{12}^2\,, \tag{2.14}$$

here $d\Phi_{12}$ is a 2-dimensional phase space integral, representing a process with two outgoing particles in the final state, given as:

$$d\Phi_{12} = \frac{d^3p_1}{(2\pi)^3 2E_1}\frac{d^3p_2}{(2\pi)^3 2E_2}(2\pi)^4\delta^4(p_{12} - p_1 - p_2) \tag{2.15}$$

and $p_{12}^2 = (p_1 + p_2)^2 = -M_{12}^2$. This integral can be simplified with the help of the Dirac delta function $\delta^4(p_{12} - p_1 - p_2)$, which was introduced by Paul Dirac [9] and it has the following property:

$$\int_{-\infty}^{\infty} \delta(x - a)F(x) = F(a)\,. \tag{2.16}$$

After performing the integration we get,

$$d\Phi_{12} = (2\pi)^{-2} \frac{\lambda^{1/2}(s_{12}, m_1^2, m_2^2)}{8 s_{12}} d\Omega_1 \,, \qquad \textbf{(2.17)}$$

here $\lambda(x, y, z) = x^2 + y^2 + z^2 - 2xy - 2yz - 2xz$, $s_{12} = p_{12}^0$ and m_i are the masses of the outgoing particle labeled as i. $d\Omega_1$ is an integration over the solid angle, which is equal to 4π, and we can also replace it with $d\Omega_2$ if we integrate d^3p_1 first using the Dirac delta function. Using the above 2-dimensional phase space integration, and with the help of Eq 2.14, we can simplify N-dimensional phase space integration in an iterative manner.

To explain what I mean by iterative manner, lets take the case of 4 particle final states, i.e. a process with 4 outgoing particles. We can express the $d\Phi_N$, using Eq 2.13, as,

$$d\Phi_4(p_\alpha, p_1, p_2, p_3, p_4) = (2\pi)^{-1} d\Phi_3(p_\alpha, p_{12}, p_3, p_4) \times d\Phi_{12}(p_{12}, p_1, p_2) dM_{12}^2 \,, \quad \textbf{(2.18)}$$

here p_a and p_b are the momenta of the colliding particles and p_i $(i = 1 - 4)$ are the momentum of the final state particles, with $p_{12} = p_1 + p_2$. We can again rewrite $d\Phi_3$ from the above equation using Eq 2.14, as

$$d\Phi_3(p_\alpha, p_{12}, p_3, p_4) = (2\pi)^{-1} d\Phi_2(p_\alpha, p_{12}, p_{34}) \times d\Phi_{34}(p_{34}, p_3, p_4) dM_{34}^2 \,, \qquad \textbf{(2.19)}$$

here $p_{34} = p_3 + p_4$. We can follow the same steps to simplify any dimensional phase space.

After this, our next step is to figure out $|\mathcal{M}|^2$. Now, this depends on the process and the underlying theory. Most of the processes that we deal with contain multiple Feynman diagrams, ranging from 10 to more than 100,000 diagrams at tree level. Each diagram corresponds to a $\mathcal{M}$, which is extremely time-consuming to calculate.

Secondly, there is also a possibility of missing some diagrams. To overcome this problem, we use Madgraph [71] to generate all the possible tree-level Feynman diagrams and then use HELAS subroutines (HELicity Amplitude Subroutines) [72] to create the matrix elements to calculate $\mathcal{M}$. These matrix elements for $\mathcal{M}$ are summed over the spins of the outgoing particles as well as the incoming particles and averaged over the spins, colors, and helicities of the incoming particles. We perform MC integration over phase space to estimate the cross-section using the VEGAS algorithm, as discussed before, and generate MC events for any process at the parton level[a].

I have used a code that combines VEGAS routines and the matrix elements generated from the HELAS subroutines and performs the steps we followed for the phase-space reduction.

While performing the MC integration for any process, importance sampling generates random numbers in the most probable region. Usually, some processes can have certain divergences, especially with the QCD processes. We could have infrared (integral $\to \infty$ when $|\vec{p}| \to 0$) or collinear divergences (When the angular separation between two outgoing particles $\to 0$). These divergences would blow up our estimates for the cross-section. We apply some basic cuts to remove those points from the phase-space. These cuts are applied on the following variables,

a) Transverse momentum of the outgoing particles ($p_T^2 = p_x^2 + p_y^2$, and the z-axis is along the beam length)

b) Pseudo rapidity η, which is given as, $\eta = -\ln \tan \theta/2$.

c) $\Delta R_{ij} = \sqrt{(\Delta\eta)_{ij}^2 + (\Delta\phi)_{ij}^2}$, Here $\Delta\phi_{ij}$ and $\Delta\eta_{ij}$ is the difference in azimuthal angle and pseudorapidity, respectively between the two outgoing particles i and j. This quantity measures the angular separation between two particles.

[a]Parton means free quarks or gluons, hence parton level means when the quarks and gluons are in the free state after pp collisions

Till now, we have only been able to perform tree-level or leading order (LO) calculations. For a realistic phenomenological study; it is important to include the higher-order corrections. We use K factors (K), which are defined as follows,

$$K = \frac{\sigma_{\rm NLO}(\sigma_{\rm NNLO})}{\sigma_{\rm LO}}\,, \tag{2.20}$$

where $\sigma_{\rm NLO}(\sigma_{\rm NNLO})$ is the cross-section after including the higher-order corrections to tree level estimates; NLO(NNLO) stands for next to leading order (next to next leading order). We use some special packages to calculate $\sigma_{\rm NLO}$, that will be discussed in Chapter 3 and 4.

After estimating the cross-sections, we can estimate how many events for that process can (ideally) be observed at the detector, using [73],

$$N = \sigma \times \mathcal{L} \tag{2.21}$$

here $\mathcal{L}$ is known as the integrated luminosity, which is the integral of luminosity with respect to time and has dimensions of the number of events per unit area. The integrated luminosity depends upon the properties of the two colliding beams. If we assume that the two beams densities are uncorrelated and collide head-on, the luminosity can be expressed as [73]:

$$\mathcal{L} = 2N_1N_2fN_b \iiint \int_{-\infty}^{+\infty} \rho_{1x}(x)\rho_{1y}(y)\rho_{1s}\left(s-s_0\right)\rho_{2x}(x)\rho_{2y}(y)\rho_{2s}\left(s+s_0\right)dxdydsds_0\,, \tag{2.22}$$

where $\rho_i(x)$, are the time-dependent density functions of the colliding beams. To a good approximation, we can assume a Gaussian distribution for all the densities, and upon integration, we get [73],

$$\mathcal{L} = \frac{N_1 N_2 f N_b}{4\pi\sigma_x\sigma_y} \tag{2.23}$$

above is a well-known expression of the luminosity of two Gaussian beams. Here N_1 and N_2 are the number of particles per bunch, f is the revolution frequency, N_b is the number of bunches and σ_x, σ_y are the bunch lengths in x and y directions (transverse plane). We have assumed that both the bunches have the same lengths.

The next step is to generate events for the signal and the backgrounds. For this dissertation, we have followed two approaches:

- (I) Generating events at the parton level and then applying naive Gaussian smearing on the momentum of the outgoing particles.

- (II) Generating events at the parton level using Madgraph, and passing those events into Pythia [74] , to simulate hadronization[a] with parton showering for the outgoing quarks, and then passing that sample to Delphes [75] to model detector response. Here we have to deal with the detector triggering efficiencies and resolutions, along with a sophisticated smearing of the momenta of the outgoing particles. We also get additional jets and leptons produced during parton showering.

We employ two methods to improve the signal to background ratio, namely a) Traditional cut based method and b) Machine learning optimization.

For case (I), we have mainly relied on optimizing cuts using a traditional cut-based approach. We discuss this in the next section.

[a] A quark cannot exist freely in nature, so whenever a quark is generated from the collision of protons, they form composite states like hadrons or mesons

2.2.3 Traditional Cut Based Optimization

Traditional cut based optimization uses the overlapping distributions to decide the cut window. In simple words, it is just a trial and error method with only one rule: preserve as much signal while removing most of the backgrounds. We select cuts based on the distribution of different variables, which conveys the signal's uniqueness under consideration or the topology of the signal. These variables are mainly reconstructed mass distributions, for example, the reconstructed mass of four leptons from, $pp \to h^0 \to ZZ^* \to 4\ell$ process. Since the Higgs width is small, the invariant mass of four leptons $m_{4\ell}$ has a sharp peak around the Higgs mass, as shown in Fig. **2.3** taken from Ref. [76].

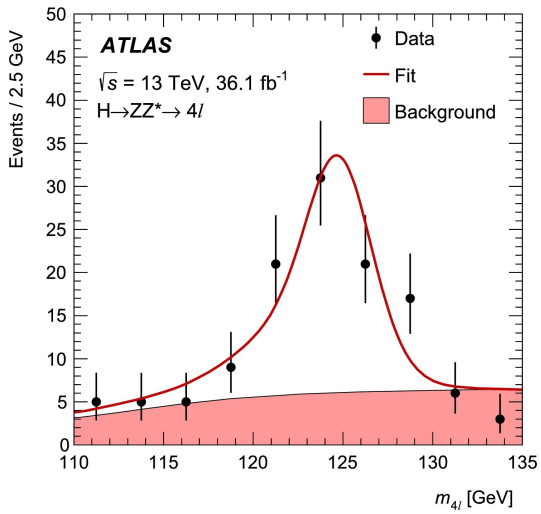

Figure 2.3: Invariant mass distribution for the data (points with error bars) shown together with the simultaneous fit result to $h^0 \to ZZ^* \to 4\ell$ candidates (continuous line). The background component of the fit is also shown (filled area). Aaboud. et al (ATLAS-Collaboration: Phys. Lett. B .2018.07.050).

Here we can apply a cut on the invariant mass $|m_{4\ell} - m_H| < 10$ GeV to remove most of the background while preserving the signal. Other than the usual mass cuts, we can also apply cuts on the missing transverse energy, especially for the signals with dark matter particles in the final state. Here in this section, we take

an example from one of our upcoming papers [77]. In this project, we studied $pp \to H^0, A^0 \to 4\ell + 2$ neutralinos ($\tilde{Z}_1^0$), where neutralinos, have a mass ~ 100 GeV and act as a source of missing transverse energy. We applied the following set of cuts (using trial and error method), based on the distributions shown in Fig. **2.4**:

- $400 \leq M_T(\ell_1, \ell_2, \ell_3, \ell_4) \leq 940$ GeV,
- $140 \leq M(\ell_1, \ell_2, \ell_3, \ell_4) \leq 340$ GeV,
- $|M(\ell_1\ell_2) - M_Z| \leq 10$ GeV,
- $10 \leq M(\ell_3, \ell_4) \leq 75$ GeV.

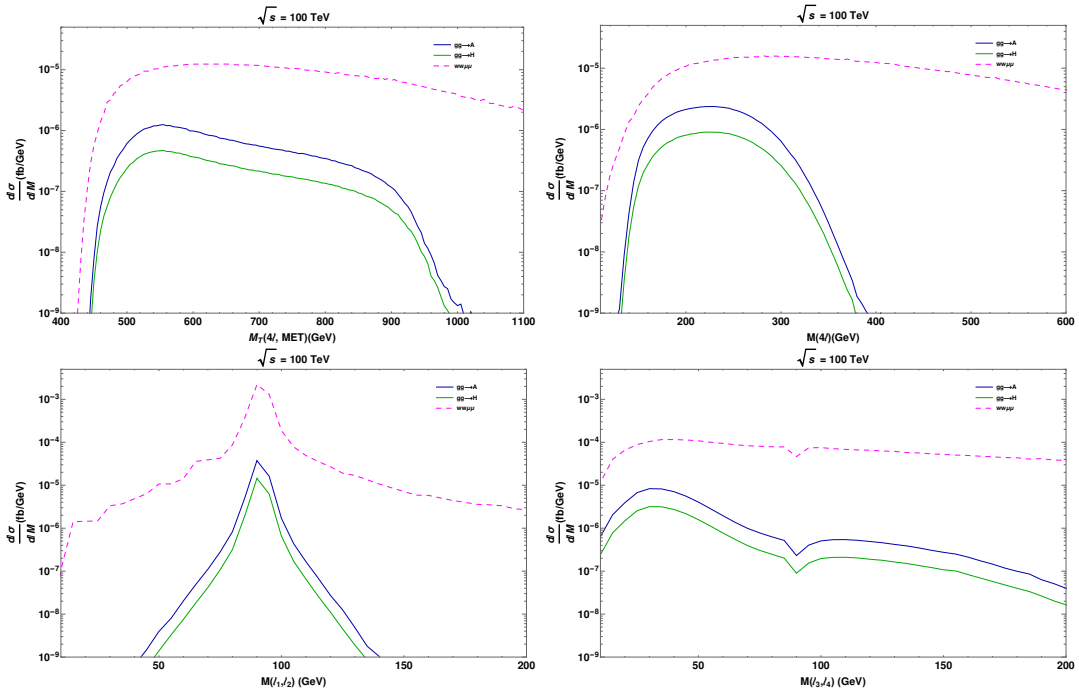

Figure 2.4: Mass distributions for $pp \to H^0, A^0 \to 4\ell + 2\tilde{Z}_1^0$ and the most dominant backgrounds.

In this case study we have set $m_A = m_H = 1000$ GeV. Table. **2.1** shows the effect of the above cuts on the signal and the most dominant background at

Process	Before Mass cuts	After mass cuts
$pp \to w^+w^-\ell^+\ell^-$	46704	203
signal	148	101

Table 2.1: Cut based optimization.

$\sqrt{s} = 100$ TeV, with $\mathcal{L} = 15000 fb^{-1}$. Our cuts work well in reducing more than 99% of the dominant background, while still keeping 70% of the signal. These results are for a particular benchmark point. We have also done a parameter scan for this signal, so stay tuned for the paper.

The traditional cut-based optimization works very well, but we have also used machine learning techniques to see if we can further improve the signal to background ratio.

2.2.4 Machine Learning with Advantages and Improvements

Machine learning is a set of algorithms that allows us to build computer programs that learn from the data, evolve, and make predictions or decisions. Machine learning helps in improving the computer's capability to learn and improve without further programming. Machine learning methods are often categorized as [78]:

- Supervised machine learning algorithms,
- Unsupervised machine learning algorithms,
- Reinforcement machine learning algorithms.

In the supervised machine learning method, the job of learning is done from well-classified training data. This means we provide a data sample that has labeled samples for the signal of interest and the associated backgrounds. These algorithms try to infer a function by analyzing the training data and determine

separate functions for the signal and the background. This is further used to classify or predict signal-like and background-like events from another sample to test the learning. In this dissertation, our approach can be broadly categorized as supervised learning.

In unsupervised machine learning, we don't have any labeled data. This type of machine learning is used to identify patterns, look for probability densities, or cluster data into groups. Reinforcement machine learning algorithms are out of the scope of this dissertation, and you can find more details at [a] .

Our main task here is to identify the signal from event samples with SM backgrounds; this can also be viewed as a problem of classifying and clustering signal events from background events. Our approach follows supervised learning, as mentioned below:

- We generate MC samples for the signal and the backgrounds. Each sample contains variables like the invariant masses, transverse momentum's of the outgoing particles, missing transverse energy, transverse masses, and angular separation variables. Each of these samples has the topology of either the signal or the background.

- We then use the boosted decision tree (BDT) [79] algorithm to make a forest of decisions that improves $N_S/\sqrt{N_S + N_B}$ ratio, where $N_S(N_B)$ are the number of signal (background) events. Here, these decisions are cuts on different variables.(Training)

- We apply all those decisions on a different sample containing both the signal and background.(Testing)

For simplicity, we randomly split each sample into two subsets and then use

[a] https://towardsdatascience.com/introduction-to-various-reinforcement-learning-algorithms-i-q-learning-sarsa-dqn-ddpg-72a5e0cb6287

one for training and other for testing. This combined operation allows us to validate the BDT. Luckily for us, TMVA (Toolkit for MultiVariate Analysis) [80] automatically performs all of those steps. The advantage of this approach over the previous cut-based analysis is that now the machine is performing all the multiple cut optimization steps and uses a more sophisticated approach towards understanding the samples. We have performed this analysis on the same process discussed in the previous section. In Table. **2.2** below, we present a comparison between the cut based analysis and a BDT optimization,

Process	Before Mass cuts	After mass cuts	BDT-cut
$pp \to w^+w^-\ell^+\ell^-$	46704	203	17
signal	148	101	56

Table 2.2: Cut Based optimization vs BDT.

The effect here is quite drastic, but here we are using parton-level events. A more sophisticated detector smearing of the momenta can reduce the gap between traditional cut based and ML techniques, but even then the BDT performs better, as we will see in Chapter 4.

Chapter 3

Probing Flavor Changing Neutral Current with Leptons

In this chapter, we present our results for the $pp \to \phi^0 \to \tau\mu + X$, $\phi^0 = H^0, A^0$. Our study includes, $\tau \to e\nu_e\nu_\tau$ (leptonic) and $\tau \to j_\tau v_\tau$ (hadronic), where $j_\tau = \pi^\pm, \rho$ and a_1 are mesons. To simplify things, we study $pp \to A^0 \to \tau\mu$ and $pp \to H^0 \to \tau\mu$ separately. In Sec 3.1, we present an elaborate study to constrain our parameter space using the experimental data. Section 3.2 discusses the properties of our signal, the favored parameter space, and the impact of different parameters on the branching fraction of $\phi^0 \to \tau\mu$. We also discuss our cuts and backgrounds associated with the leptonic and hadronic τ-lepton decay channels. The final cross-sections for the backgrounds after all the cuts are calculated at $\sqrt{s}$ =14, 27, and 100 TeV. In Sec 3.3, we present our estimates of the discovery potential for both H^0 and A^0 separately. In this study, we have used a simple cut-based analysis, as discussed in Sec 2.2.3. The results of this study are published in Ref. [81].

3.1 Constraints on Relevant Parameters

Our signal cross-section depends directly on $\rho_{\tau\mu}$ and $\rho_{\mu\tau}$, which are responsible for the decay $H^0/A^0 \to \tau\mu$, and ρ_{tt} for the production $gg \to H^0/A^0$ via the triangle-top loop. Indirectly, $\rho_{tc} \sim \mathcal{O}(1)$ can enhance $H^0/A^0 \to t\bar{c},\ c\bar{t}$, which can suppress the $H^0/A^0 \to \tau\mu$ branching ratio. On the other hand, ρ_{ct} is tightly constrained from B physics data [50]. LHC data [82, 83] for the 125 GeV h^0 boson favors the decoupling limit, i.e. $|\cos(\beta-\alpha)| \ll 1$ for a THDM with NFC [84]. As a case study,

we take $\cos(\beta-\alpha) = 0.1$, although larger values are allowed in the gTHDM [50, 85]. We choose other diagonal ρ matrix elements to be $\rho_{ff} = \kappa_f = \sqrt{2}m_f/v$ except for ρ_{tt}, and ignore off-diagonal ones except $\rho_{\tau\mu}$, $\rho_{\mu\tau}$ and ρ_{tc}. We have set the masses of the additional scalars to be degenerate, i.e. $M_H = M_A = M_{H^\pm}$. In this section, we consider phenomenological constraints on $\rho_{\tau\mu}$, $\rho_{\mu\tau}$, ρ_{tt}, and ρ_{tc} under these assumptions. Our choice of $\cos(\beta - \alpha) = 0.1$ leads to cross-sections of $pp \to H^0 \to W^+W^- + X$ below the current ATLAS limits [86] and it is consistent with recent LHC measurements of a light Higgs boson(h^0) [87, 88]. In Table. **3.1**, we present cross-sections of heavier Higgs boson (H^0) decaying into a pair of W bosons in the gTHDM at $\sqrt{s} = 13$ TeV with the experimental limits from ATLAS for $\sqrt{s} = 13$ TeV.

$pp \to H^0 \to WW + X$			
M_H (GeV)	$\lambda_5 = 0$ (fb)	λ_5 = -1 (fb)	ATLAS limit (fb)
300	1.23×10^3	1.98×10^3	$\leq 8.000\times10^3$
400	7.17×10^2	9.49×10^2	$\leq 1.3\times10^3$
500	2.17×10^2	2.47×10^2	$\leq 4.00\times10^2$

Table 3.1: Cross section of p p $\to H^0 \to W^+W^- + X$ at $\sqrt{s} = 13$ TeV and ATLAS limits at $\sqrt{s} = 13$ TeV.

Following the modified Yukawa Lagrangian from Eq 2.1, the branching ratio for $h^0 \to \tau\mu$ is,

$$\mathcal{B}(h^0 \to \tau\mu) = \frac{M_{h^0} c^2_{\beta-\alpha}}{16\pi\Gamma_{h^0}}(|\rho_{\tau\mu}|^2 + |\rho_{\mu\tau}|^2), \qquad (\mathbf{3.1})$$

where $M_{h^0} \simeq 125$ GeV, including both $\tau^+\mu^-$ and $\mu^+\tau^-$ modes. We evaluate the total width, Γ_{h^0} by adding $h^0 \to WW^*, ZZ^*, gg, b\bar{b}, c\bar{c}$ and $\tau^+\tau^-$ partial widths obtained by rescaling the SM values [89] with $\Gamma(h^0 \to \tau\mu)$ added. We constrain

the branching fraction, $\mathcal{B}(h^0 \to \tau\mu) < 0.25\%$ by CMS [90] at 95% C.L. Using the above constraint we require $\rho_{\tau\mu} \leq 0.01$, assuming $\rho_{\tau\mu} = \rho_{\mu\tau}$. We can put further constraints on $\rho_{\tau\mu}$ and $\rho_{\mu\tau}$ through various low-energy processes containing the tau-lepton and muon as discussed in the literature (see e.g. Ref. [91–94]). The most relevant constraints come from $\tau \to \mu\gamma$. This branching ratio is given by [94]

$$\mathcal{B}(\tau \to \mu\gamma) = \frac{48\pi^3\alpha}{G_F^2}(|A_L|^2 + |A_R|^2)\mathcal{B}(\tau \to \mu\bar{\nu}_\mu\nu_\tau), \qquad (\mathbf{3.2})$$

where we take $\mathcal{B}(\tau \to \mu\bar{\nu}_\mu\nu_\tau) = (17.39 \pm 0.04)\%$ [95], and $A_{L,R}$ gives the strength of the $\tau \to \mu\gamma$ amplitude with different chiral structure. To calculate the branching fraction $\mathcal{B}(\tau \to \mu\gamma)$, we have included the one-loop contributions from the neutral ($H^0,\ A^0$) and charged Higgs ($H^\pm$) as well as two-loop Barr-Zee type contributions in $A_{L,R}$, following Ref. [94]. The latter contribution can also be obtained by the obvious translation of the expression for $\mu \to e\gamma$ [96]. To bring in the ρ_{tt} dependence via top-loop, we also include the dominant contribution from the effective $\phi^0\gamma\gamma$ ($\phi^0 = h^0,\ H^0,\ A^0$) vertex. We use the direct constraints on $\tau \to \mu\gamma$ branching ratio by BELLE [97] which are $\mathcal{B}(\tau \to \mu\gamma) < 4.5 \times 10^{-8}$ at 90% C.L and 4.4×10^{-8} by BABAR [98]. BELLE II may improve the BELLE limit by a factor of 100 [99]. We set $\mathcal{B}(\tau \to \mu\gamma) = 10^{-9}$ to illustrate the future sensitivity.

ρ_{tt} is also constrained by B physics, in particular, by the B_q ($q = d, s$) meson mixing and $b \to s\gamma$ [50]. We update the results of Ref. [50] using the latest experimental and theoretical values from the Summer 2018 result by UTfit [100]. for the CKM parameters and constraints on the B_q-$\bar{B}_q$ mixing amplitude (M_{12}^q):

$$\begin{aligned} &C_{B_d} \in [0.83,\ 1.29], \quad \phi_{B_d} \in [-6.0^\circ,\ 1.5^\circ], \\ &C_{B_s} \in [0.942,\ 1.288], \quad \phi_{B_s} \in [-1.35^\circ,\ 2.21^\circ] \quad \text{at 95\% probability}, \end{aligned} \qquad (\mathbf{3.3})$$

where $C_{B_q}e^{2i\phi_{B_q}} \equiv M_{12}^q/[M_{12}^q]_{\rm SM}$. As for $b \to s\gamma$, we adopt a recent world average $B(\bar{B} \to X_s\gamma)_{\rm exp} = (3.32 \pm 0.15) \times 10^{-4}$ [101], which includes the recent BELLE result [102] and the updated SM prediction $B(\bar{B} \to X_s\gamma)_{\rm SM} = (3.36 \pm 0.23) \times 10^{-4}$ [103, 104] for the photon energy $E_\gamma > 1.6$ GeV. We then use the ratio [105] $R_{\rm exp}^{b\to s\gamma} = \mathcal{B}(\bar{B} \to X_s\gamma)_{\rm exp}/\mathcal{B}(\bar{B} \to X_s\gamma)_{\rm SM}$ to constrain $R_{\rm theory}^{b\to s\gamma} = \mathcal{B}(\bar{B} \to X_s\gamma)_{\rm THDM}/\mathcal{B}(\bar{B} \to X_s\gamma)_{\rm SM}$ based on our LO calculation,
allowing the 2σ experimental uncertainty of $R_{\rm exp}^{b\to s\gamma}$ with the theoretical uncertainty linearly added. We have ignored the effects from ρ_{tc} coupling on the B_q mixing and $b \to s\gamma$ as it enters via the charm loop, making its impact minor [105] in comparison with ρ_{tt} and ρ_{ct} entering via the top loop. We constrain ρ_{tc} coupling using the recent 95% C.L limit on $\mathcal{B}(t \to ch^0) < 1.1 \times 10^{-3}$ by the ATLAS [106]. The $\mathcal{B}(t \to ch^0)$ is nonzero if $\cos(\beta-\alpha)$ is nonzero, as shown below. Using Eq 1.48, we can evaluate the $t \to ch^0$ decay width in terms of ρ_{tc} and $\cos(\beta-\alpha)$ as,

$$\Gamma(t \to ch^0) \simeq \frac{M_t \cos^2(\beta-\alpha)}{32\pi}\lambda^{1/2}(1, x_c, x_h)\left[(1 + x_c - x_h)\frac{|\rho_{tc}|^2 + |\rho_{ct}|^2}{2}\right], \quad \textbf{(3.4)}$$

where $\lambda(x, y, z) = x^2+y^2+z^2-2xy-2yz-2zx$, $x_c = M_c^2/M_t^2$ and $x_h = M_h^2/M_t^2$. We add this to the LO width of $\Gamma(t \to bW)$ to estimate the total width of the top quark. Using that, we constrain the $\lambda_{tch} = |\tilde{\rho}_{tc}\cos(\beta-\alpha)| = |\rho_{tc}\cos(\beta-\alpha)/\sqrt{2}| \lesssim 0.064$ from the ATLAS limits for $\rho_{ct} = 0$. For the numerical calculation performed in this section, we use updated mass values of particles from the PDG [95], especially the top quark pole mass, $M_t = (173.1 \pm 0.9)$ GeV and bottom quark $\overline{\rm MS}$ mass, $M_b(M_b) = 4.18^{+0.04}_{-0.03}$ GeV as input. Figure. **3.1** summarizes the constraints on the $(\rho_{tt},\ \rho_{\tau\mu})$ plane with $\rho_{\mu\tau} = \rho_{\tau\mu}$ for (a) $M_{H^0} = M_{A^0} = M_{H^\pm} = 150$ GeV and (b) 300 GeV: exclusions are shown by the blue-hatched regions for $h^0 \to \tau\mu$ by CMS, gray-shaded regions for $\tau \to \mu\gamma$ by BABAR, pink-shaded regions for B_s mixing (C_{B_s}) and green-hatched regions for $b \to s\gamma$. The other three observables

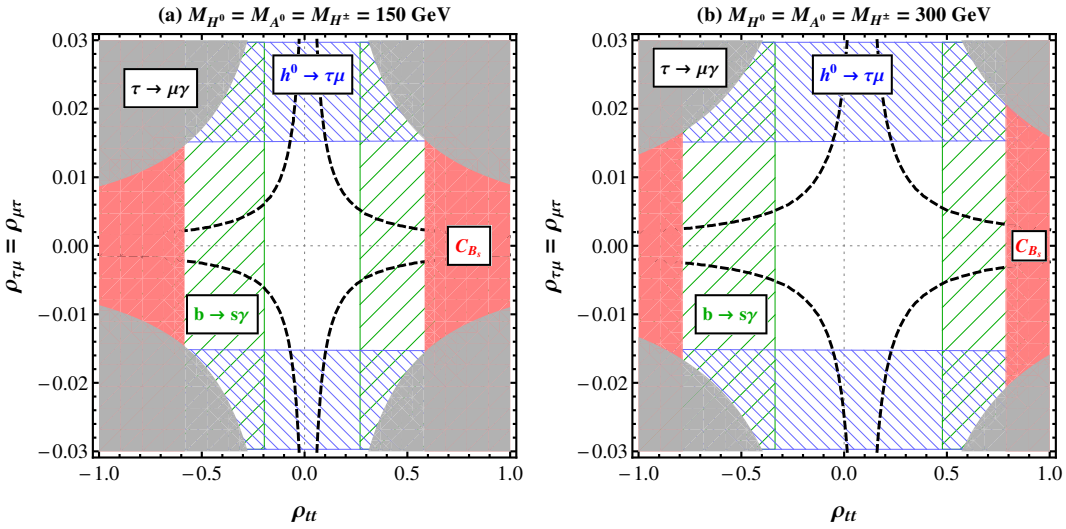

Figure 3.1: Constraints on the $(\rho_{tt}, \rho_{\tau\mu})$ plane with $\rho_{\mu\tau} = \rho_{\tau\mu}$ for (a) $M_{H^0} = M_{A^0} = M_{H^\pm} = 150$ GeV and (b) 300 GeV, both assuming $\cos(\beta - \alpha) = 0.1$, $\rho_{\tau\tau} = \kappa_\tau$ and $\rho_{bb} = \kappa_b$. Dashed lines indicate $\mathcal{B}(\tau \to \mu\gamma) = 1 \times 10^{-9}$ for a future sensitivity. See the main text for details.

in Eqs (**3.3**) give weaker limit than C_{B_s} and are not shown in the figures. The dashed contours with $\mathcal{B}(\tau \to \mu\gamma) = 10^{-9}$ are shown as the BELLE II sensitivity. An important thing to note here is that the constraints on $\rho_{\tau\mu}$ and ρ_{tt} coming from $h^0 \to \tau\mu$ and $b \to s\gamma$ are very sensitive to the choice of the parameters. For $\rho_{\tau\mu}$, constraints coming from $h^0 \to \tau\mu$ gets weaker for smaller values of $\cos(\beta - \alpha)$ and eventually loses sensitivity if $\cos(\beta - \alpha) = 0$. In case of ρ_{tt}, the $b \to s\gamma$ constraint is relaxed for a smaller $|\rho_{bb}|$, and becomes weaker than the B_s mixing constraint if $\rho_{bb} = 0$.

Combining experimental limits from LHC Higgs data and B physics and assuming perturbativity, we consider $\rho_{\tau\mu} < 0.01$, and $|\tilde{\rho_{tc}} c_{\beta-\alpha}| < 0.064$ [107]. To be consistent with the B-physics constraints, we choose

$$\rho_{tt} = 0.2 \times (M_\phi / 150, \text{GeV}) \tag{3.5}$$

for $\phi^0 = H^0$ or A^0, which satisfies the $b \to s\gamma$ constraints for the heavy Higgs

scalar masses considered in this study.

3.2 Higgs Signal and Physics Background

In this section, we discuss the prospect of discovering the FCNH interaction, from $H^0, A^0 \to \tau\mu$. Several parameters can affect the signal cross-section in the gTHDM. We use the experimental results and constraints to optimize our parameter space. Current data from LHC, both 7-8 TeV, and 13 TeV [55, 108], points toward a Higgs sector, in which the light scalar Higgs state is SM-like and follows the decoupling limit. Hence, for our analysis, we set $\cos(\beta - \alpha) = 0.1$.

We take the heavy Higgs states (H^0, A^0, and $H^\pm$) to be degenerate and choose $\lambda_{6,7} = 0$ for simplicity. We choose two values of $\lambda_5 = -1$ and 0 to satisfy tree-level unitarity, perturbativity and vacuum stability of the Higgs potential in the gTHDM. A more detailed discussion is presented in Appendix A. For the Yukawa couplings, we set the diagonal terms $\rho_{ii} = \kappa_i$, except $\rho_{tt} = 0.2(M_H/150)$. For off-diagonal terms, ρ_{ij} [50], we perform case studies for $\tilde{\rho_{tc}}$= 0.1 and 0.5, and scan over $0.001 \leq \rho_{\tau\mu} \leq 0.01$, ignoring the remaining off-diagonal terms. Despite being degenerate and neutral, we study $pp \to A^0 \to \tau\mu$ and $pp \to H^0 \to \tau\mu$ separately.

For H^0, tanβ and λ_5 play a crucial role in affecting the $H^0 \to \tau\mu$ branching ratios, alongside $\tilde{\rho_{tc}}$. We have used 2HDMC [109], to scan over $150 \leq M_H, M_A \leq 500$ GeV and $1 \leq \tan\beta \leq 10$ for $\lambda_5 = 0$; the results are presented in Fig. **3.2**. We see that for $M_H > 2m_t$, $H^0 \to t\bar{t}$, $H^0 \to h^0h^0$ and $H^0 \to tc$ channels become dominant. This suggests that $M_H > 2m_t$ may not be discoverable for this channel, so we limit our case study to $M_H < 500$ GeV.

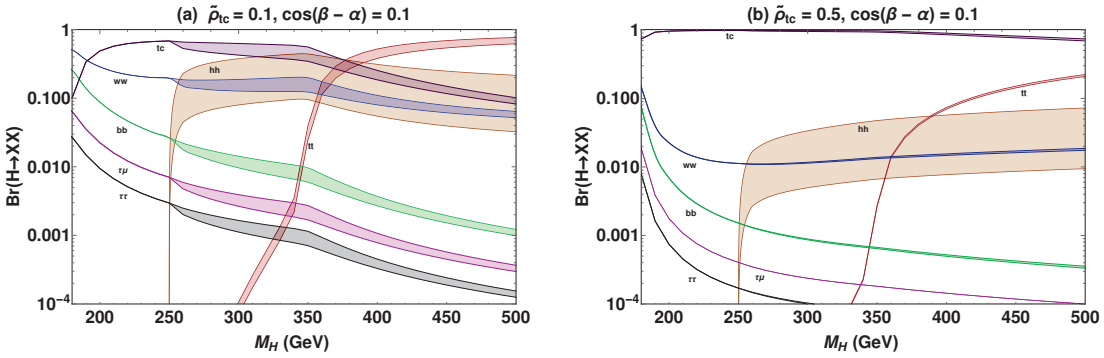

Figure 3.2: Branching ratios for $H^0 \to XX$ w.r.t M_H. Including all the dominant two body decays, with $\rho_{\tau\mu} = 0.01$. We have set $\lambda_5 = 0$ and $1 \leq \tan\beta \leq 10$.

On the other hand, $A^0 \to h^0 h^0$ is forbidden, hence its decay is independent of $\tan\beta$ and λ_5, as shown in Fig. **3.3**. Only $\tilde{\rho_{tc}}$ has an impact on the branching fractions of $A^0 \to \tau\mu$. When $M_A > 220$ GeV, $A^0 \to Zh$ also has a significant branching ratio and for $M_A > 2M_t$, $A^0 \to t\bar{t}$ channel starts to dominate. Hence we limit our study to $M_A < 500$ GeV as well.

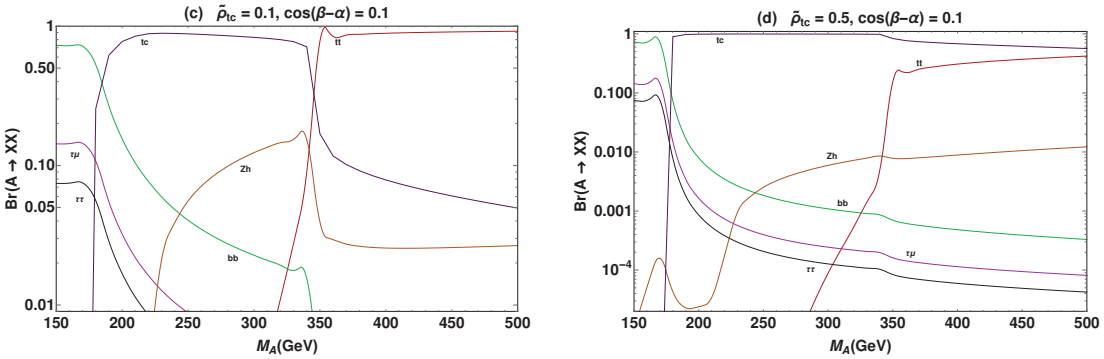

Figure 3.3: Branching Ratios for A $\to$ all dominant two body decays w.r.t M_A, setting $\rho_{\tau\mu} = 0.01$.

3.2.1 Higgs Signal

The dominant production channel for $\phi^0 = H^0,\ A^0$ is gluon-gluon fusion (GGF), $gg \to \phi^0 \to \tau\mu + X$ [110]. When τ-lepton decays leptonically to electrons, the

final state consists of two opposite sign, different flavor leptons with the missing transverse energy. For a hadronically decaying τ-lepton, our final state has a j_τ, an oppositely charged muon, and the missing transverse energy. In Table. **3.2**, we show the branching fractions of different τ-lepton decays we have considered from Ref. [5].

Decay mode	Branching Fraction
$\tau^+ \to \pi^+ \bar{\nu_\tau}$	10.82%
$\tau^+ \to \pi^+ \pi^0(\rho) \bar{\nu_\tau}$	25.49%
$\tau^+ \to (\pi^+\pi^+\pi^- + \pi^+\pi^0\pi^0)(a_1) \bar{\nu_\tau}$	18.29%
$\tau^+ \to e^+ \nu_e \bar{\nu_\tau}$	17.8%
$\tau^+ \to \mu^+ \nu_\mu \bar{\nu_\tau}$	17.4 %

Table 3.2: Branching fractions for different τ-lepton decays considered.

We have performed an analytic calculation to compute the matrix element and computed the signal cross-section using the parton distribution function CT14PDFs [111, 112] for leading order (LO) calculations. To scale our LO estimates to NNLO, we have calculated the K factors using Higlu [113, 114] for $pp \to \phi^0 + X$. In Table. **3.3**, we present our estimates for the production cross-sections at NNLO for $pp \to H^0,\ A^0 + X$ as a function of their masses for $\sqrt{s} = 13$ TeV.

M_ϕ	σ for H^0	σ for A^0
150	31.75	81.02
200	18.77	47.07
300	9.99	31.23
350	10.28	62.24
400	9.57	28.4
500	4.54	8.62

Table 3.3: Cross section at NNLO in pb for $pp \to \phi^0 + X$ from gluon fusion at the LHC with $\sqrt{s} = 13$ TeV.

In Appendix B, we present our estimates of the K factors for different center of mass energies $\sqrt{s}$ as a function of the scalar mass for both the H^0 and A^0.

3.2.2 Standard Model Backgrounds

The dominant background for the leptonic final states comes from $pp \to \tau^+\tau^- \to e^\pm\mu^\mp + \not{E}_T + X$, $pp \to W^+W^- \to e^\pm\mu^\mp + \not{E}_T + X$ and $pp \to h^0 \to \tau^+\tau^- \to e^\pm\mu^\mp + \not{E}_T + X$. As stated in Ref. [115], fake leptons also play a part in the total backgrounds, but their modeling is beyond the scope of this study. For the hadronic channel, we have $pp \to W^\pm j \to \mu j + \not{E}_T + X$ as the most dominant background along with the $pp \to \tau^+\tau^- \to j_\tau\mu^\pm + X$ channel. For the hadronic channel, the contribution from $t\bar{t}$ is highly suppressed when we veto any event with more than 0 b-jets, with $p_T > 20$ GeV and $|\eta| < 4.7$.

We have used Madgraph [71] and HELAS [72], to generate tree level matrix elements for the backgrounds. We have calculated the tree-level cross sections for the backgrounds using CT14PDFs [111, 112]. To scale the backgrounds to NLO, we have calculated the K Factors using MCFM 8.0 [116].

3.2.3 Realistic Acceptance Cuts

To study the discovery potential for our signal, we apply realistic acceptance cuts proposed by CMS [54, 55] at 13 TeV as shown in Table. **3.4**.

Parameters	$\phi^0 \to e\mu + X$	$\phi^0 \to j_\tau\mu + X$
$P_T(e)$	> 10 GeV	
$P_T(\mu)$	> 26 GeV	> 26 GeV
$P_T(j_\tau)$		> 30 GeV
$\lvert\eta_e\rvert$	< 2.3	
$\lvert\eta_\mu\rvert$	< 2.4	< 2.4
$\lvert\eta_{j_\tau}\rvert$		< 2.3
$\Delta R(e, \mu)$	> 0.3	
$\Delta R(j_\tau, \mu)$		> 0.5
$\Delta\phi(P_T(e), \not{E}_T)$	< 0.7	
$\Delta\phi(P_T(e), P_T(\mu)$	> 2.5	
$M_T(\mu)$	< 60 GeV	
$M_T(e)$	> 50 GeV	
$M_T(j_\tau)$		< 105 GeV
$\lvert M_{col} - M_{\phi^0}\rvert$	$< 0.2 \times M_{\phi^0}$	$< 0.2 \times M_{\phi^0}$

Table 3.4: Cuts.

Here, M_{col} is the reconstructed scalar mass using the collinear approximation [117]. In the collinear approximation, we reconstruct the τ-lepton momentum as $P_\tau = P_{e,or,j_\tau}/x$, where x is the fraction of τ-lepton momentum carried by electron or j_τ. The underlying assumption is that the τ-leptons are highly boosted because $M_H \gg m_\tau$ as a result the decay products (e or j_τ) are collinear to the τ-lepton

momentum. With this assumption, we can write the missing transverse energy as:

$$\not{E}_T = (1-x)P_{T\tau}\,, \tag{3.6}$$

here, $P_{T\tau}$ is the transverse momentum of τ-lepton. Using the above equation with $P_\tau = P_{e,or,j_\tau}/x$, we get:

$$x = \frac{P_T}{P_T + \not{E}_T}\,. \tag{3.7}$$

Where P_T is the transverse momentum of the electron or j_τ. Using Eq 3.7, we can calculate the approximate invariant mass (M_{col}) of the scalar.

To simulate detector smearing, based on ATLAS [118] and CMS [119] specifications, we apply Gaussian smearing on our momenta [120, 121],

$$\frac{\Delta E}{E} = \frac{0.60}{\sqrt{E(GeV)}} \oplus 0.03\ (\text{jets})\,, \qquad \frac{\Delta E}{E} = \frac{0.25}{\sqrt{E(GeV)}} \oplus 0.01\ (\text{leptons}). \tag{3.8}$$

In Table. **3.5**, we present our estimates for the background cross-sections after applying cuts from Table. **3.4**. We have included the K factors along with the mis-tagging efficiency of light jets to be $\epsilon_j = 0.01$ [122, 123] and the tagging efficiencies of a j_τ, $\epsilon_{j_\tau} = 0.7$ [124, 125].

As we increase the mass of the scalar M_{col} cut becomes stronger and after $M_H > 180$ GeV $pp \to h^0 \to \tau\tau$ and $pp \to h^0 \to WW^*$ are completely vetoed. We also see that for the leptonic channel, $pp \to W^+W^-$ becomes more dominant than $pp \to \tau^+\tau^-$, as shown in Fig. **3.4**:

$\sqrt{s}$	14 TeV	27 TeV	100 TeV
Backgrounds for $\tau \to e + X$			
p p $\to \tau\tau$ + X	31.96	58.74	195.09
p p $\to W^+W^-$ + X	12.27	23.73	86.29
p p $\to h^0 \to \tau\tau$ + X	1.92	5.06	27.9
p p $\to h^0 \to WW^*$ + X	0.95	2.51	13.87
Total	47.1	90.04	323.15
Backgrounds for $\tau \to j_\tau + X$			
p p $\to W^{\pm} j$ + X	2895.7	6200.6	25748.4
p p $\to \tau\tau$ + X	109.8	202.3	676.9
p p $\to h \to \tau\tau$ + X	6.4	16.9	93.3
Total	3011.5	6419.8	26519

Table 3.5: Cross-sections of all the backgrounds for both leptonic and hadronic channel in fb at $\sqrt{s} = 14$, 27, and 100 TeV. With $M_{\phi^0} = 125.1$ GeV.

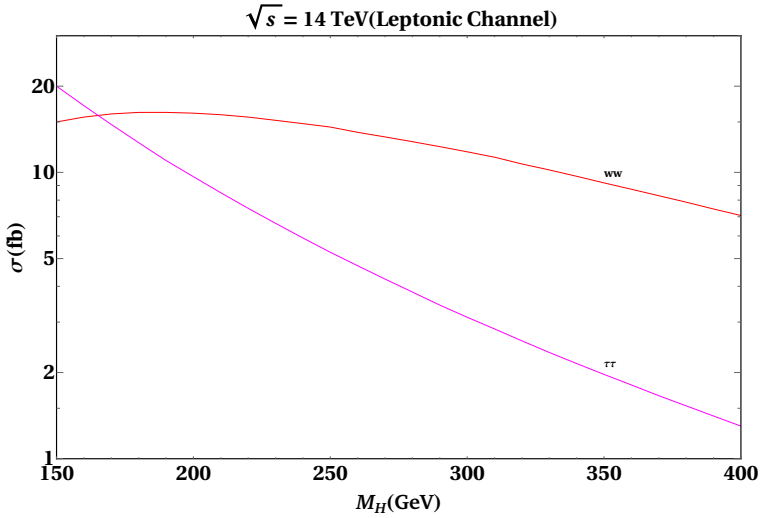

Figure 3.4: Cross-section of backgrounds as a function of M_H at $\sqrt{s} = 14$ TeV.

3.3 Discovery Potential

3.3.1 Discovery Reach for Pseudo-scalar

From Table. **3.3**, we find that the cross-section for $pp \to A^0 + X$ is greater than $pp \to H^0 + X$. The $A^0 \to h^0 h^0$ decays are forbidden, which makes $A^0 \to \tau\mu$

more promising channel than the heavy scalar $H^0 \to \tau\mu$.

In Fig. **3.5** we present the discovery regions for $pp \to A^0 \to \tau\mu$ in the [M_A, $\rho_{\tau\mu}$] plane, for $\tilde{\rho_{tc}} = 0.1$ and 0.5, including both leptonically decaying τ-lepton (top row) and hadronically decaying τ-lepton (bottom row). The high QCD backgrounds for the hadronic case makes it be harder to probe A^0 for the masses above 200 GeV.

We have shown the results for $\sqrt{s}$ = 14, 27, and 100 TeV. At low masses, M_A <180 GeV, the entire range of $\rho_{\tau\mu}$ is detectable at 3000 fb^{-1}. For an intermediate range, e.g. $200 < M_A < 260$ GeV, we observe that our discovery region starts shrinking as $A^0 \to Zh$ starts dominating. The additional contribution from $A^0 \to t\bar{t}$ further suppresses our signal as we explore values above $M_A > 260$ GeV. For the higher mass range, e.g. $M_A > 300$ GeV, for both $\tilde{\rho_{tc}} = 0.1$ and 0.5, we see a slight increase in the 5σ region, around $M_A \sim 2M_t$, it is due to the rise in the production cross-section for $pp \to A^0 + X$, as shown in Table. **3.3**, this compensates for the decreasing branching ratio of $A^0 \to \tau\mu$, as shown in Fig. **3.3**.

To define the discovery potential, we use [50],

$$\sigma_S = \frac{N}{\mathcal{L}}[N + 2\sqrt{\mathcal{L}\sigma_B}]. \tag{3.9}$$

Where $\sigma_{S(B)}$ is the signal(background) cross-section and $\mathcal{L}$ is the integrated luminosity. Choosing $N = 2.5(1.5)$ for $5\sigma(3\sigma)$ significance. For a large number of background events, Eq 3.9 simplifies to

$$\sigma_S = \frac{2N\sqrt{\mathcal{L}\sigma_B}}{\mathcal{L}}. \tag{3.10}$$

Using Eq 2.21, we can write $N_S(N_B) = \mathcal{L}\sigma_S(\mathcal{L}\sigma_B)$, substituting this back into

Eq 3.10,

$$N_S = 2N\sqrt{N_B}, \tag{3.11}$$

$$N_{SS} = \frac{N_S}{\sqrt{N_B}}\,. \tag{3.12}$$

Here $N_{SS} = 2$ N, and "SS" refers to the statistical significance.

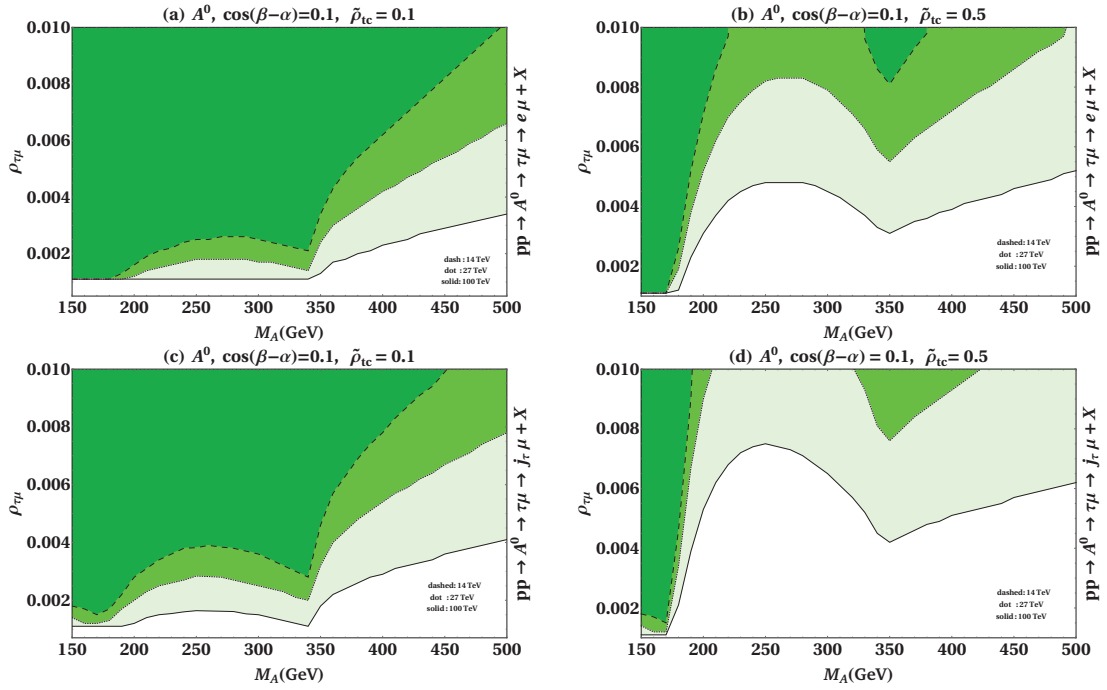

Figure 3.5: Discovery range at the LHC and future hadron colliders with $\sqrt{s} =$ 14 TeV (green dark shading), 27 TeV (intermediate shading) and 100 TeV (light shading) for $pp \to A^0 \to \tau\mu + X$ in the $(M_A, \tilde{\rho}_{\tau\mu})$ plane. We require 5σ significance for 3000fb^{-1}. Top (bottom) row is for leptonic (hadronic) τ-lepton decay for $\tilde{\rho}_{tc} = 0.1$[(a) and (c)] and $\tilde{\rho}_{tc} = 0.5$[(b)and(d)].

3.3.2 Discovery Reach for Heavy Scalar

For H^0, the situation is quite different, as we saw in Fig. **3.2**. The branching ratios for the $H^0 \to \tau\mu$ are also affected by changing tanβ and λ_5, in addition to the suppression coming from the $H^0 \to t\bar{c}$, $\bar{t}c$ through $\tilde{\rho_{tc}}$. In order to understand the

effect of λ_5, we perform an analysis by fixing $M_H = 300$ GeV [126] and $\rho_{\tau\mu} = 0.01$. We vary $-1 \leq \lambda_5 \leq 1$, for a fixed $\tan\beta = 1$. The results are shown in Fig. **3.7**, with $\sqrt{s}$ =14 TeV, 27 TeV and 100 TeV, for the leptonic channel. The hadronic channel should behave the same way, except it will have a higher QCD background.

We observe that for a fixed $\tan\beta$, increasing λ_5 from -1 to 1 decreases the cross-

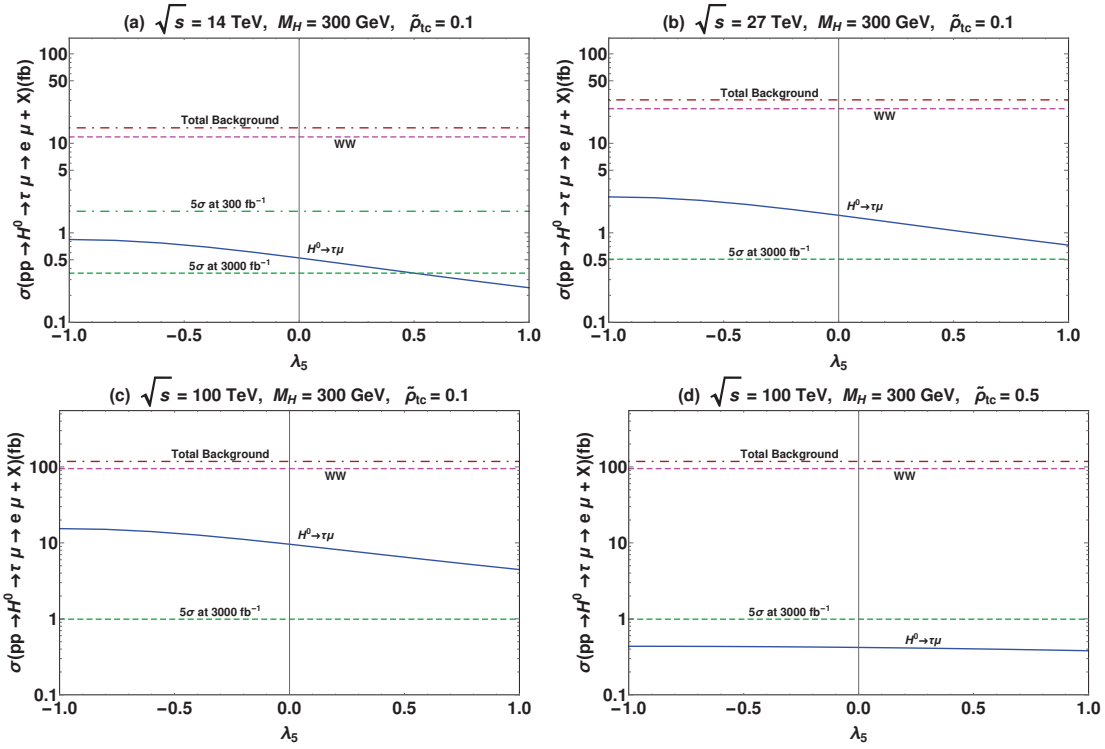

Figure 3.6: Cross-section (in fb) of $pp \to H^0 \to \tau\mu \to e\mu + X$ (blue solid) at (a) $\sqrt{s} = 14$ TeV, (b) 27 TeV and (c) 100 TeV, as a function of λ_5 with $M_H = 300$ GeV, $\rho_{\tau\mu} = 0.01$, $\tan\beta = 1$, $\cos(\beta - \alpha)$, and $\tilde{\rho}_{tc} = 0.1$. Also shown are the total background (maroon dotdash), the predominant background from $pp \to W^+W^- + X$ (magenta dash), and the 5σ signal significance (green dash) with integrated luminosity $\mathcal{L} = 3000\ fb^{-1}$ or $300\ fb^{-1}$. We also present results for (d) $\tilde{\rho}_{tc} = 0.5$ at $\sqrt{s} = 100$ TeV.

section of $pp \to H^0 \to \tau\mu + X$. This is because of the increasing tri-linear Higgs coupling, g_{Hhh} [127], which enhances the $H^0 \to h^0h^0$ decay,

$$
\begin{aligned}
g_{Hhh} &\simeq -\frac{\cos(\beta-\alpha)}{v}\Big[4m_A^2 - 2m_h^2 - m_H^2 + 4\lambda_5 v^2 \\
&+ \frac{2v^2}{\tan(2\beta)}(\lambda_6-\lambda_7) + \frac{2v^2}{\sin(2\beta)}(\lambda_6+\lambda_7) + \mathcal{O}(\cos(\beta-\alpha))\Big].
\end{aligned}
$$

As a case study, we choose two values of λ_5 = -1 and 0. We have fixed tan$\beta = 1$ to preserve tree-level unitarity and stability of the gTHDM in 2HDMC [109]. We perform a scan for $0.001 \leq \rho_{\tau\mu} \leq 0.01$ and $150 \leq M_H \leq 500$ GeV. Our results are shown in Fig. **3.7**. We see a large discoverable region in the low mass regime ($M_H < 180$ GeV). But as $M_H > 180$ GeV first $H^0 \to tc$ decay dominates and then after $M_H > 260$ GeV, $H^0 \to h^0h^0$ followed by $H^0 \to t\bar{t}$ channels become dominant. The discovery potential continues to decrease as we increase the scalar mass, but we again see a slight improvement as $M_H \sim 2M_t$, that we observed for $A^0 \to \tau\mu$. Beyond that region, we still have some probable parameter space, and a 100 TeV high energy collider can probe to an even lower $\rho_{\tau\mu}$ coupling. The likelihood of detection further increases as we reduce λ_5, from 0 to -1.

To show the sensitivity of possible systematic uncertainties on the Higgs signal of $H^0 \to \tau\mu$, we present the ratio N_S/N_B, as well as the statistical significance $N_{SS} = N_S/\sqrt{N_B}$ in Table. **3.6** for $pp \to H^0 \to \tau\mu \to e\mu + X$, and $pp \to H^0 \to \tau\mu \to j_\tau\mu + X$ in Table. **3.7**. We choose $\rho_{\tau\mu} = 0.005$, $\lambda_5 = 0$, and an integrated luminosity $\mathcal{L} = 3000\ fb^{-1}$. We show the number of signal events and background events at $\sqrt{s} = 14$ TeV, 27 TeV, and 100 TeV. These data give the totality of the relevant information pertaining to the strength of the signal versus background. Note that the cross-section of pseudoscalar (A^0) will be larger than that of (H^0).

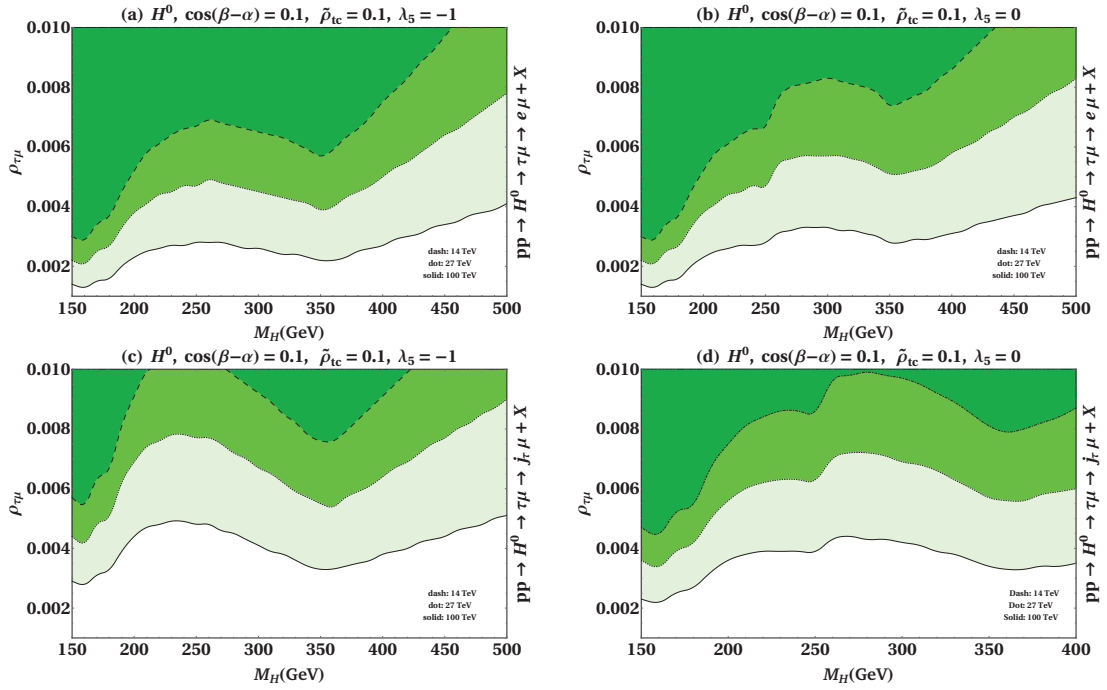

Figure 3.7: Discovery regions at the LHC and future hadron colliders with the $\sqrt{s} = 14$ TeV (green dark shading), 27 TeV (intermediate shading) and 100 TeV (light shading) for $pp \to H^0 \to \tau\mu + X$ in the $(M_H, \tilde{\rho}_{\tau\mu})$ plane. We require at least 5σ significance for 3000fb^{-1}. Top (bottom) row is for leptonic (hadronic) τ-lepton decay with $\lambda_5 = -1$[(a) and (c)] and $\lambda_5 = 0$[(b) and (d)].

$pp \to H^0 \to \tau\mu \to e\mu + \not{E}_T + X$					
$\sqrt{s} = 14$ TeV					
M_H(GeV)	Total Background	Signal	Min(for 5 σ)	N_S/N_B	$N_{SS} \equiv N_S/\sqrt{N_B}$
150	1.06×10^5	4.68×10^3	1.63×10^3	0.044	14.36
200	7.73×10^4	1.29×10^3	1.39×10^3	0.017	4.66
250	5.88×10^4	7.00×10^2	1.22×10^3	0.012	2.89
300	4.47×10^4	3.94×10^2	1.06×10^3	0.009	1.86
400	2.51×10^4	2.74×10^2	7.99×10^2	0.011	1.73
500	1.42×10^4	9.2×10^1	6.03×10^2	0.006	0.77
$\sqrt{s} = 27$ TeV					
150	2.03×10^5	1.18×10^4	2.26×10^3	0.06	26.18
200	1.52×10^5	3.48×10^3	1.95×10^3	0.023	8.92
250	1.19×10^5	1.99×10^3	1.73×10^3	0.017	5.77
300	9.19×10^4	1.18×10^3	1.52×10^3	0.013	3.89
400	5.39×10^4	8.98×10^2	1.17×10^3	0.017	3.87
500	3.2×10^4	3.3×10^2	9.0×10^2	0.01	1.84
$\sqrt{s} = 100$ TeV					
150	7.2×10^5	5.78×10^4	4.25×10^3	0.08	68.15
200	5.56×10^5	1.85×10^4	4.73×10^3	0.033	24.82
250	4.46×10^5	1.14×10^4	3.34×10^3	0.026	17.06
300	3.53×10^5	7.21×10^3	2.98×10^3	0.02	12.13
400	2.16×10^5	6.11×10^3	2.33×10^3	0.028	13.16
500	1.32×10^5	2.5×10^3	1.82×10^3	0.019	6.86

Table 3.6: Number of events for signal and backgrounds for different M_H at $\sqrt{s}$ = 14, 27, and 100 TeV for leptonic channel with $\rho_{\tau\mu} = 0.005$.

$pp \to H^0 \to \tau\mu \to j_\tau\mu + \not{E}_T + X$					
$\sqrt{s} = 14$ TeV					
M_H(GeV)	Total Background	Signal	Min(for 5 σ)	N_S/N_B	$N_{SS} \equiv N_S/\sqrt{N_B}$
150	1.51×10^7	1.54×10^4	1.94×10^4	0.001	3.95
200	7.5×10^6	4.2×10^3	1.37×10^4	0.0006	1.55
250	3.67×10^6	2.28×10^3	9.59×10^3	0.0006	1.19
300	1.9×10^6	1.29×10^3	6.89×10^3	0.0007	0.94
400	5.85×10^5	8.88×10^2	3.83×10^3	0.0015	1.16
500	2.13×10^5	2.94×10^2	2.31×10^3	0.0014	0.64
$\sqrt{s} = 27$ TeV					
150	3.53×10^7	3.87×10^4	2.97×10^4	0.0011	6.52
200	1.81×10^7	1.14×10^4	2.13×10^4	0.00063	2.67
250	9.18×10^6	6.51×10^3	1.15×10^4	0.0007	2.15
300	4.87×10^6	3.87×10^3	1.1×10^4	0.0008	1.75
400	1.57×10^6	2.92×10^3	6.27×10^3	0.0019	2.33
500	5.93×10^5	1.06×10^3	3.86×10^3	0.0018	1.37
$\sqrt{s} = 100$ TeV					
150	1.57×10^8	1.89×10^5	6.23×10^4	0.0012	15.07
200	8.5×10^7	6.05×10^4	4.61×10^4	0.0007	6.56
250	4.5×10^7	3.73×10^4	3.36×10^4	0.0008	5.56
300	2.48×10^7	2.36×10^4	2.49×10^4	0.00095	4.75
400	8.5×10^6	1.98×10^4	1.46×10^4	0.0023	6.8
500	3.4×10^6	8×10^3	9.22×10^4	0.0024	4.34

Table 3.7: Number of events for signal and backgrounds for different M_H at $\sqrt{s}$ = 14, 27, and 100 TeV for hadronic τ-lepton decays, with $\rho_{\tau\mu} = 0.005$.

Chapter 4

Probing Flavor Changing Neutral Current with Charm and Top

The ρ_{tc} coupling, which drives the $t \to ch^0$ decays, presents a very rich phenomenology as mentioned in Sec 2.1.1. This chapter presents a detailed collider study for this FCNH top (t) quark decay. In Sec 4.1, we show results for the $t \to ch^0 \to cW^+W^-$, where we have performed a parton level study with naive Gaussian smearing. The results of this study are published in Ref. [128]. In Sec 4.2, we present a study for $t \to ch^0 \to c\tau^+\tau^-$. Here we present a similar parton level study, but in addition to that, we model hadronization and parton showering with Pythia8 [74] and detector response with Delphes [75]. This is an ongoing project, and we expect to publish this study by the end of this year.

4.1 $h^0 \to W^+W^-$

4.1.1 The Higgs Signal and Physics Background

The main goal of this section is to understand the essential constituents of the FCNH Higgs signal, i.e, $t \to ch^0$ produced in pp collisions.

We choose $pp \to t\bar{t} + X$ as our production channel for the Higgs signal because of the high production cross-section for the $t\bar{t}$ channel at the LHC. At $\sqrt{s} = 13$ TeV, the cross-section for the top-antitop quark pair, $\sigma_{t\bar{t}} \simeq 820\ pb$ and with an integrated luminosity $\mathcal{L}$= 160 fb^{-1}, the LHC can produce $\sim 1.3 \times 10^8$ [129, 130] top pairs. The major contributions for the top-pair production comes from gluon-gluon fusion and quark-antiquark fusion. The Higgs signal is coming from the decay of

one top-quark into a charm quark and Higgs, while the other top quark decays hadronically via $t \to bW \to bjj$. After including all the decays discussed above, our full signal looks like, $pp \to t\bar{t} \to tch^0 \to bjj\, c\ell\ell\nu\nu + X, \ell = e, \mu$. Figure. **4.1** shows the Feynman diagram for our Higgs signal.

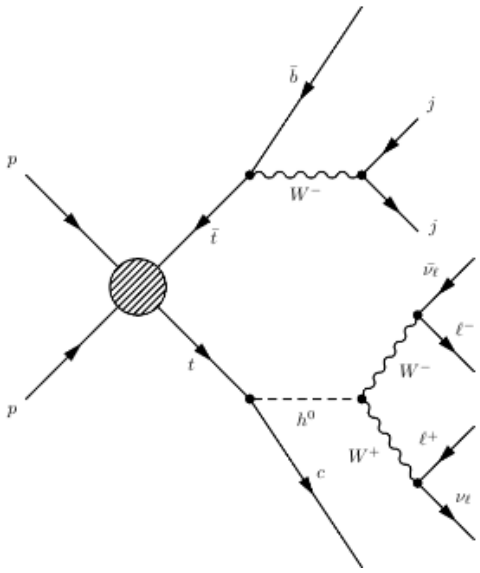

Figure 4.1: Feynman diagram for $pp \to t\bar{t} \to bjj\, ch^0 + X \to bjj\, c\ell^+\ell^-\nu\nu X$, where $\ell = e$ or μ.

4.1.2 The Higgs Signal in Top Decay

Following Eq 3.4 the decay width for $t \to ch^0$, can be written as,

$$\Gamma_{t\to ch^0} \simeq \frac{c^2_{\beta\alpha} m_t^2}{32\pi}\{(1 + r_c^2 - r_h^2)\frac{(|\rho_{ct}|^2 + |\rho_{tc}|^2)}{2}\}\lambda^{1/2}(1, r_c^2, r_h^2), \qquad (\mathbf{4.1})$$

where $c_{\beta\alpha} = \cos(\beta - \alpha)$, $r_h = M_h/m_t$, $r_c = m_c/m_t$, and,

$$\lambda(x, y, z) = x^2 + y^2 + z^2 - 2xy - 2xz - 2yz\,. \qquad (\mathbf{4.2})$$

We define,

$$\tilde{\rho}_{tc} = \sqrt{\frac{|\rho_{tc}|^2 + |\rho_{ct}|^2}{2}}. \tag{4.3}$$

Note that we have already placed constraints on $\tilde{\rho_{tc}}$, as seen in Sec 3.1, using LHC Higgs data and B physics measurements.

For typical values of parameters $\cos(\beta - \alpha) = 0.1$, $|\tilde{\rho_{tc}}| \sim 0.5$, with $m_t = 173.2$ GeV and $m_c = 1.42$ GeV, we estimate,

$$\Gamma_{t \to ch^0} \simeq 0.09(c^2_{\beta\alpha}|\tilde{\rho}_{tc}|^2) \simeq 2.3 \times 10^{-4}\ \text{GeV}\,. \tag{4.4}$$

The total decay width of the top quark is given as,

$$\Gamma_t = \Gamma(t \to bW) + \Gamma(t \to ch^0)\,. \tag{4.5}$$

We assume that $t \to ch^0$ is the only beyond SM decay channel for the top quark. The branching fraction of $t \to ch^0$ becomes:

$$\mathcal{B}(t \to ch^0) = \frac{\Gamma(t \to ch^0)}{\Gamma_t} \simeq 1.5 \times 10^{-4}\ . \tag{4.6}$$

Which is below the current limits from ATLAS [106], $\mathcal{B}(t \to ch^0) \leq 1.1 \times 10^{-3}$. When this project was getting ready for the publication, ATLAS limits were $\mathcal{B}(t \to ch^0) \leq 1.6 \times 10^{-3}$ [107].

We can also redefine the Lagrangian described in Eq 1.48, by replacing ρ^F and $(\beta - \alpha)$ with an effective coupling g_{htc}, to study the FCNH Higgs interaction with top (t) and charm (c) quark, as,

$$\mathcal{L} = -g_{htc}\bar{c}th^0 + \text{H.c.}. \tag{4.7}$$

The decay width for $t \to ch^0$, using the above effective Lagrangian [131] becomes:

$$\Gamma(t \to ch^0) = \frac{|g_{htc}|^2}{16\pi}(m_t)(1 + r_c^2 - r_h^2)\lambda^{1/2}(1, r_c^2, r_h^2)\,. \qquad (\mathbf{4.8})$$

Comparing the above results with Eq 4.1, we get:

$$g_{htc} = \frac{1}{\sqrt{2}}\tilde{\rho}_{tc}\cos(\beta - \alpha) = \frac{1}{\sqrt{2}}\sqrt{|\rho_{tc}|^2 + |\rho_{ct}|^2}\cos(\beta - \alpha) = \frac{1}{\sqrt{2}}\lambda_{tc}\,. \qquad (\mathbf{4.9})$$

Here we express λ_{tc} in terms of g_{htc} and $\tilde{\rho}_{tc}\cos(\beta - \alpha)$, following the ATLAS [106, 107] notation. Using the latest ATLAS-limits [106] and following Eq 4.4 and Eq 4.9, we require,

$$g_{htc} \precsim 0.045\,. \qquad (\mathbf{4.10})$$

Whereas from the older limits [107] $g_{htc} \precsim 0.064$. In 1987, T.P Cheng and Marc Sher [132], proposed a mass-matrix ansatz in which they defined the off-diagonal Yukawa couplings to be the geometric mean of the Yukawa couplings of the quarks; it is popularly known as the Cheng-Sher ansatz (CS).

$$g_{htc}(\mathrm{CS}) = \frac{\sqrt{m_t m_c}}{v} \simeq 0.0637, \qquad (\mathbf{4.11})$$

or

$$\lambda_{tc}(\mathrm{CS}) = \sqrt{2}\, g_{htc} = \frac{\sqrt{2m_t m_c}}{v} \simeq 0.0901\,, \qquad (\mathbf{4.12})$$

with $m_t = 173.2$ GeV and $m_c = 1.42$ GeV, the branching fraction of $t \to ch^0$ becomes $\mathcal{B}(t \to ch^0) = 2.2 \times 10^{-3}$ for $M_h = 125.1$ GeV. This is well above the current ATLAS limits and hence the CS approximation is ruled out. We have used $\sqrt{2}g_{htc} = \tilde{\rho}_{tc}\cos(\beta - \alpha)$ with $\tilde{\rho}_{tc}$ and $\cos(\beta - \alpha)$ as free parameters for our collider study.

Now, the next step is evaluating the cross-section and event generation. To make sure we don't miss any tree-level Feynman diagrams, we have used MadGraph [71], and, HELAS [72] to evaluate the tree level matrix elements for the FCNH signal in top decays from gluon-gluon fusion and quark-antiquark annihilation,

$$\begin{aligned} gg, q\bar{q} &\rightarrow t\bar{t} \rightarrow t\bar{c}h^0 \rightarrow bjj\bar{c}\ell^+\ell^-\nu\bar{\nu}\,, \quad \text{and}\,, \\ gg, q\bar{q} &\rightarrow \bar{t}t \rightarrow \bar{t}ch^0 \rightarrow \bar{b}jjc\ell^+\ell^-\nu\bar{\nu}\,, \end{aligned} \tag{4.13}$$

where $\ell = e$ or μ. We have modeled the $t \rightarrow ch^0$ decays using the Lagrangian in Eq 4.7 in Feynrules [133].

The cross-section of the Higgs signal in the FCNH top decays at the LHC and future hadron colliders for $pp \rightarrow t\bar{t} \rightarrow tch^0 \rightarrow bjj\, c\ell^+\ell^-\nu\bar{\nu} + X$ is evaluated with the parton distribution functions of CT14LO [111, 112]. We scale our cross-section to NNLO with the K factor, calculated with the renormalization scale (μ_R) and factorization scale (μ_F) set to $Q = M_{t\bar{t}}$ = the invariant mass of $t\bar{t}$.

These choices of scales leads to a K factor of approximately 1.8 for top-quark pair production. We have used the computer program Top++ [134] to evaluate the higher order corrections, with CT14NNLO pdfs [111, 112]. For consistency, we have compared our tree-level signal cross-section with the narrow width approximation.

That is, the cross-section $\sigma(pp \rightarrow t\bar{t} \rightarrow tch^0 \rightarrow bjj\, c\ell^+\ell^-\nu\bar{\nu} + X)$ is calculated as the product of cross-section times branching fractions:

$$\sigma(pp \rightarrow t\bar{t} \rightarrow bjj\bar{t} + X) \times \mathcal{B}(t \rightarrow ch^0) \times \mathcal{B}(h^0 \rightarrow W^+W^-) \times \mathcal{B}(W \rightarrow \ell\nu_\ell)^2\,. \tag{4.14}$$

Our Higgs signal comes from both $t \rightarrow ch^0$ and $\bar{t} \rightarrow \bar{c}h^0$, so we include both

$t\bar{t} \rightarrow t\bar{c}h^0 \rightarrow bjj\, \bar{c}\ell^+\ell^-\nu_\ell\bar{\nu}_\ell$ and $t\bar{t} \rightarrow ch^0\bar{t} \rightarrow \bar{b}jj\, c\ell^+\ell^-\nu_\ell\bar{\nu}_\ell$. We select all those events which consist of one b jet and three light jets ($j = u, d, s, c$ or g = gluons

in case of physics backgrounds). In addition, we require two opposite charged leptons coming from the Higgs decays, along with neutrinos, which leads to the missing transverse energy. That means our FCNH signal leads to the final state of $bjj\, c\ell^+\ell^-\nu_\ell\bar{\nu_\ell}$ or $bjjj\ell^+\ell^- + \not{E}_T$.

4.1.3 The Physics Background

The dominant SM background corresponding to the final state of $bjjc\ell^+\ell^-\nu\bar{\nu}$ comes from top quark pair production along with two light jets ($t\bar{t}jj$), $pp \to t\bar{t}jj \to b\bar{b}jjWW \to b\bar{b}jj\ell^+\ell^-\nu\bar{\nu} + X$, where every top quark decays into a b-quark as well as a W boson ($W \to \ell\nu$) and a b-jet is mis-identified as a c-jet or a light jet. The other subdominant SM backgrounds we have considered are:

- $pp \to t\bar{t}W \to b\bar{b}jjWW \to b\bar{b}jj\ell^+\ell^-\nu\bar{\nu} + X$ with one W boson decaying into jj,
- $pp \to b\bar{b}jjW^+W^- \to b\bar{b}jj\ell^+\ell^-\nu\bar{\nu} + X$, excluding the contribution from $t\bar{t}jj$,
- $pp \to b\bar{b}jj\tau^+\tau^- \to b\bar{b}jj\ell^+\ell^-\nu\bar{\nu}\nu_\tau\bar{\nu_\tau}$,
- $pp \to c\bar{c}jjW^+W^- \to c\bar{c}jj\ell^+\ell^-\nu\bar{\nu}+X$ and $pp \to jjjjW^+W^- \to jjjj\ell^+\ell^-\nu\bar{\nu}+X$ where $j = u, d, s$, or g.

In the high energy colliders, identifying different flavors of quarks is very difficult, especially, the light jets (u, d, s, and c). As for the b-quarks, they travel a few millimeters before decaying; this is used to isolate the b-jet from the other light jets. This method of b-jet identification doesn't guarantee a 100% identification rate, and for a few events a highly boosted light jet j can be misidentified as a b-jet [122, 135]. So we evaluate the cross-section of physics backgrounds in pp collisions by multiplying the cross-section with the tagging and mis-tagging

efficiencies associated with the b-jet identification. In our analysis, we adopt ATLAS tagging efficiencies [122, 135]: the b tagging efficiency is $\sim 70\%$, the probability that a c-jet is mis-tagged as a b-jet (ϵ_c) is approximately 14%, while the probability that any other jet is mis-tagged as a b-jet (ϵ_j) is 1%.

4.1.4 Mass Reconstruction

In this section, we discuss the topology of the Higgs signal, which is coming from top quark pair production with $t\bar{t} \to bjj\, ch^0 \to bjj\, c\ell^+\ell^- + \not{E}_T$. Our main motive is to reconstruct the two top quarks and the Higgs boson. We have two stumbling blocks, one to find the mother of light jets and the other, how to reconstruct the Higgs boson from the missing transverse energy. To determine the reconstructed top mass as the invariant mass of $b + j_1 + j_2$ coming from $t \to bW \to bj_1j_2$, we select those pair of light jets that minimizes $|M_{jj} - m_W| + |M_{bjj} - m_t|$ as j_1 and j_2 and label the other jet as $j_3 \simeq c$. This means, for a correctly reconstructed event, j_1 and j_2 are the products of a W decay such that their invariant mass distribution peaks at $M_{j_1j_2} \simeq m_W$.

For $t \to ch^0 \to c\ell^+\ell^- + \not{E}_T$, we cannot reconstruct the invariant mass of the Higgs boson due to the missing transverse energy from the neutrinos. But, we can reconstruct the cluster transverse mass distributions $d\sigma/dM_T(\ell\ell, \not{E}_T)$ and $d\sigma/dM_T(c\ell\ell, \not{E}_T)$ with the missing transverse energy ($\not{E}_T$) from the neutrinos [30, 136], defined below:

$$M_T^2(\ell\ell, \not{E}_T) = (\sqrt{p_T^2(\ell\ell) + M_{\ell\ell}^2} + \not{E}_T)^2 - (\vec{p}_T(\ell\ell) + \vec{\not{E}}_T)^2 \qquad \textbf{(4.15)}$$

and

$$M_T^2(c\ell\ell, \not{E}_T) = (\sqrt{p_T^2(c\ell\ell) + M_{c\ell\ell}^2} + \not{E}_T)^2 - (\vec{p}_T(c\ell\ell) + \vec{\not{E}}_T)^2\,, \qquad \textbf{(4.16)}$$

where $p_T(\ell\ell)$ or $p_T(c\ell\ell)$ is the total transverse momentum of the visible particles and $M_{\ell\ell}$ and $M_{c\ell\ell}$ are the invariant mass of two leptons and the invariant mass of two leptons + charm, respectively. We expect these distributions to have a sharp end points near $M_T(\ell\ell, \not{E}_T) \sim m_h$ and $M_T(c\ell\ell, \not{E}_T) \sim m_t$.

In every event, we require one tagged b-jet and three light jets. For a background event, one b is likely coming from the top decay $t \to bW \to bjj$ while the other is either a mis-tagged c or a light quark jet coming from W decay.

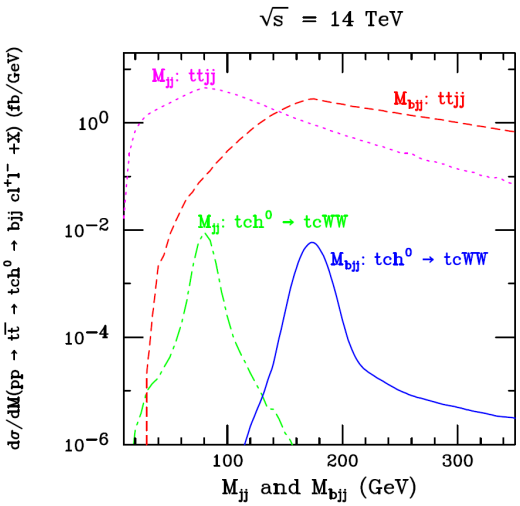

Figure 4.2: Invariant mass distributions ($d\sigma/dM$) of $j_1 j_2$ (green dotdash), and $bj_1 j_2$ (blue solid), for the Higgs signal in pp collisions, $d\sigma/dM(pp \to t\bar{t} \to tch^0 \to tcWW \to bjjc\ell^+\ell^- + \not{E}_T + X$ (fb/GeV), with basic cuts defined in Eq 4.17. Also shown are the invariant mass distributions $d\sigma/dM_{j_1 j_2}$ (magenta dot) and $d\sigma/dM_{bj_1 j_2}$ (red dash) for the dominant physics background from $t\bar{t}jj$.

We present the invariant mass distributions for $M_{j_1 j_2}$ and $M_{bj_1 j_2}$ in Fig. **4.2** for the Higgs signal ($t\bar{t} \to tch^0$) and the dominant background ($t\bar{t}jj$) with basic

cuts from CMS [137]:

$$
\begin{aligned}
&\text{(a) } p_T(b,j) > 25 \text{ GeV}\,, \\
&\text{(b) } p_T(\ell_1) > 25 \text{ GeV}\,, p_T(\ell_2) > 15 \text{ GeV}\,, \\
&\text{(c) } \not{E}_T > 25 \text{ GeV}\,, \\
&\text{(d) } |\eta(j,\ell)| < 2.4\,, \quad \text{and} \\
&\text{(e) } |\Delta R(jj,\ell\ell,j\ell)| > 0.4\,,
\end{aligned}
\tag{4.17}
$$

where $p_T(\ell_1) \geq p_T(\ell_2)$. It is clearly evident that the $M_{j_1 j_2}$ distribution peaks at m_W while $d\sigma/dM_{bjj}$ has a peak at m_t.

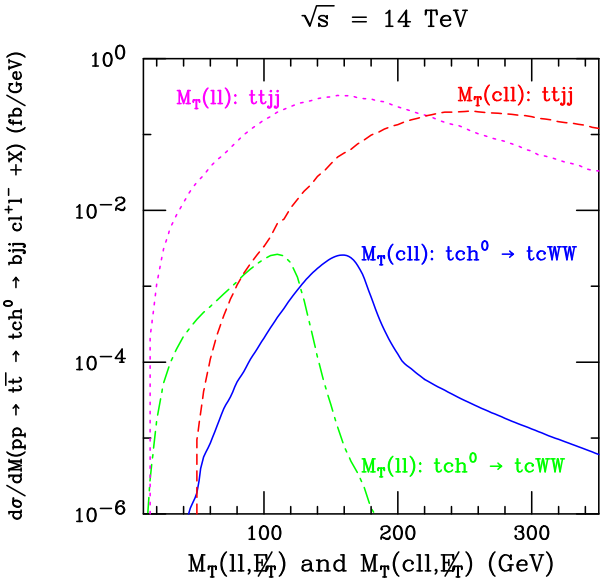

Figure 4.3: Cluster transverse mass distributions ($d\sigma/dM_T$) of $\ell^+\ell^-$ (green dotdash) and $c\ell^+\ell^-$ (blue solid) for the Higgs signal in pp collisions, $d\sigma/dM_T(pp \to t\bar{t} \to tch^0 \to tcWW \to bjjc\ell^+\ell^- + \not{E}_T + X$ (fb/GeV), with basic cuts defined in Eq 4.17, as well as $|M_{jj} - m_W| \leq 0.15 \times m_W$ and $|M_{bjj} - m_t| \leq 0.20 \times m_t$. Also shown are the cluster transverse mass distributions $d\sigma/dM_T(\ell\ell, \not{E}_T)$ (magenta dot) and $d\sigma/dM_T(c\ell\ell, \not{E}_T)$ (red dash) for the dominant physics background from $t\bar{t}jj$.

Figure. **4.3** presents the cluster transverse mass distributions $(d\sigma/dM_T(\ell\ell, \not{E}_T))$ and $(d\sigma/dM_T(c\ell\ell, \not{E}_T))$ for the Higgs signal in pp collisions, $d\sigma/dM_T(pp \to t\bar{t} \to$

$tch^0 \to tcWW \to bjjc\ell^+\ell^- + \not{E}_T + X$ (fb/GeV), with basic cuts defined in Eq 4.17, as well as $|M_{jj} - m_W| \leq 0.15 \times m_W$ and $|M_{bjj} - m_t| \leq 0.20 \times m_t$ and the dominant background ($t\bar{t}jj$). Note that for the signal, $d\sigma/dM_T(\ell\ell, \not{E}_T)$ peaks near m_h while $d\sigma/dM_T(c\ell\ell, \not{E}_T)$ has a peak near m_t. The invariant mass distributions of jets shows pronounced peaks at m_W and m_t as shown in Fig. **4.2** and the cluster transverse mass distributions gives us sharp end points near m_h and m_t. By looking carefully at all four distributions, we can clearly distinguish signal from the dominant SM backgrounds. We can use these distributions to define powerful selection rules to remove the SM backgrounds while preserving most of the signal.

4.1.5 Realistic Acceptance Cuts

To study the discovery potential for the signal, we have applied realistic basic cuts listed in Eq 4.17 and tagging efficiencies for the b-jets. In addition to the basic cuts, we apply cuts on (a) invariant mass of jets $|M_{jj} - m_W| \leq 0.15 \times m_W$ and $|M_{bjj} - m_t| \leq 0.20 \times m_t$, as well as (b) cluster transverse mass of $\ell\ell$ and $c\ell\ell$, 50 GeV $\leq M_T(\ell\ell, \not{E}_T) \leq$ 150 GeV, and 100 GeV $\leq M_T(c\ell\ell, \not{E}_T) \leq$ 210 GeV respectively to veto the background events.

Measurement uncertainties in the jet and lepton momenta as well as missing transverse momentum give rise to a spread in the reconstructed masses about the true values of m_t and M_{h^0}. We use the same Gaussian smearing for leptons and jets as shown in Eq 3.5.

4.1.6 Discovery Potential at the LHC

In this section we present our estimates for the discovery potential of the Higgs signal at the hadron colliders. We first apply all of the basic cuts and realistic mass cuts to remove much of the SM backgrounds. Our cross-section after applying all

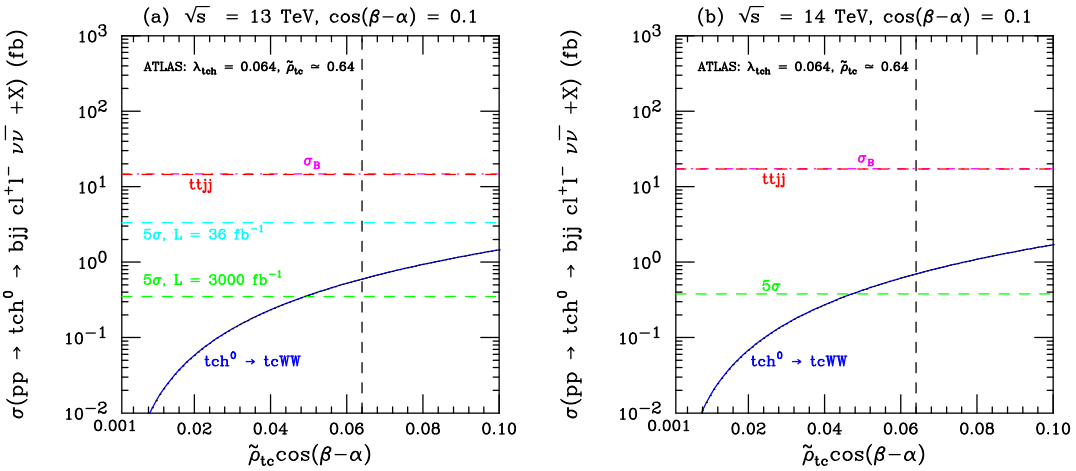

Figure 4.4: The cross-section in fb of $pp \to t\bar{t} \to tch^0 \to bjjc\ell^+\ell^- + \not{E}_T + X$ at $\sqrt{s} = 13$ TeV and 14 TeV as a function of $\tilde{\rho}_{tc}$, along with total (magenta dotdash) and most dominant (red dash) background after applying all the cuts, tagging and mistagging efficiencies, and higher order QCD corrections. The blue dash line and green dash line shows the minimum cross-section needed for 5σ significance at $\mathcal{L} = 36 fb^{-1}$ and $3000 fb^{-1}$ respectively for the center of mass energy of 13 TeV. Where as for 14 TeV, we present $\mathcal{L} = 3ab^{-1}$ (green dash) only. The ATLAS-Limit-2019 is shown as a black dash vertical line.

the cuts for the Higgs signal at the LHC with $\sqrt{s} = 13$ TeV and $\sqrt{s} = 14$ TeV as well as cross-sections for future hadron colliders with $\sqrt{s} = 27$ TeV and $\sqrt{s} = 100$ TeV are shown in Table. **4.1**. Cross-sections for the dominant background processes are presented in Table. **4.2**.

$\tilde{\rho}_{tc}$	13 TeV	14 TeV	27 TeV	100 TeV
0.1	0.015	0.017	0.06	0.54
0.5	0.364	0.425	1.53	13.6
1	1.46	1.70	6.15	54.4

Table 4.1: Cross-section of Higgs signal in fb.

Here we have kept $\cos(\beta - \alpha) = 0.1$. Later for the contours, we will vary $\cos(\beta - \alpha)$ from 0.01 to 0.2. The next thing is to estimate the discovery potential of the Higgs signal at the current and future high energy pp colliders. We have calculated the statistical significance following the same criteria as described in

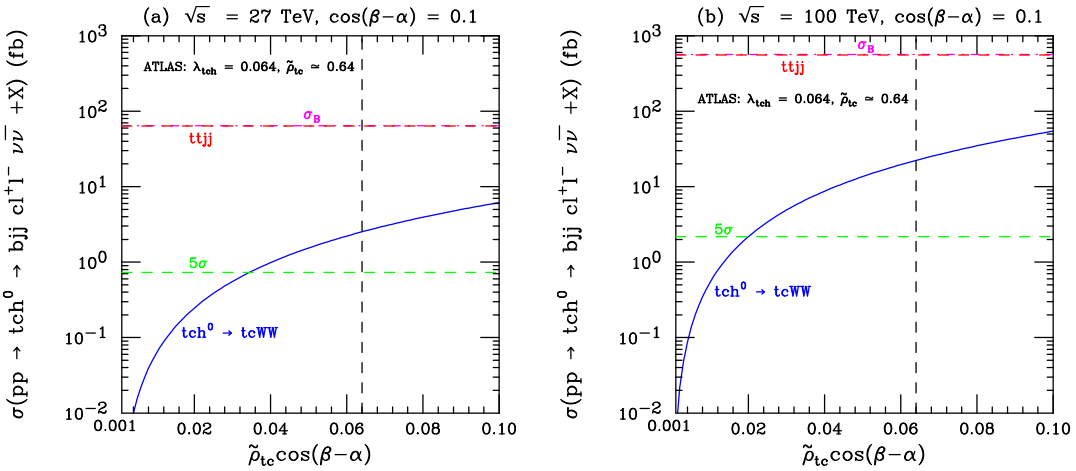

Figure 4.5: Similar to Fig. **4.4**, but for (a) $\sqrt{s} = 27$ TeV, and (b) 100 TeV.

Background	13 TeV	14 TeV	27 TeV	100 TeV
$t\bar{t}jj$	14.6	17.1	63.6	557
$t\bar{t}W$	0.16	0.17	0.36	1.41
$b\bar{b}jj\tau\tau$	0.035	0.039	0.13	0.95
$b\bar{b}jjWW$	0.003	0.0035	0.011	0.09
$c\bar{c}jjWW$	0.0017	0.0019	0.006	0.05
$WWjjjj$	9.96E-06	1.12E-05	2.48E-05	0.0002
Total Background	14.8	17.3	64.1	559.5

Table 4.2: Cross-section in fb for dominant physics background processes with K factors and tagging efficiencies.

Sec 3.3.1. Figure. **4.4** shows the Higgs signal cross-section as a function of $\tilde{\rho}_{tc}$, along with the cross-section of the total background and the most dominant background process ($t\bar{t}jj$) for the LHC with $\sqrt{s}$ =13 and 14 TeV. We have also shown the minimum cross-section required for 5σ significance, which from Eq 3.6, can be written as:

$$\sigma_S \geq \frac{2.5}{\mathcal{L}}[2.5 + 2\sqrt{\mathcal{L}\sigma_B}], \tag{4.18}$$

at an integrated luminosity of $\mathcal{L} = 36.1 fb^{-1}$ and higher luminosities (HL) for the future HL-LHC [138, 139](High Luminosity-Large Hadron Colliders), i.e. $\mathcal{L}$ = 300 and 3000 fb^{-1}. All tagging efficiencies and the K factors discussed above

are included. We have also included the 2019 ATLAS-limit [88], shown as a vertical black-dashed line. Our analysis suggests an improvement in the reach of ATLAS [88] at an integrated luminosity of 3000 fb^{-1}, the sensitivity improves at higher energies(HE-LHC), i.e $\sqrt{s}$ =27 and 100 TeV, as shown in Fig. **4.5**.

We also present the 5σ discovery reach at the LHC for (a) $\sqrt{s} = 13$ TeV , (b) $\sqrt{s} = 14$ TeV in Fig. **4.6**, in the parameter plane of $[\cos(\beta - \alpha), \tilde{\rho}_{tc}]$. We have chosen $\mathcal{L} = 300$ and 3000 fb^{-1}. For the future high energy colliders with $\sqrt{s}$ =27 and 100 TeV, High energy LHC with integrated luminosity, $\mathcal{L} = 300$ and 3000 fb^{-1}, we can probe a large parameter space that we have used in our analysis as shown in Fig. **4.6**. However, with the new limits [88], the region of probable parameter space shrinks, but by including more Higgs decay channel we can improve our discovery reach for the Higgs signal. New contours are shown in Fig. **4.7**.

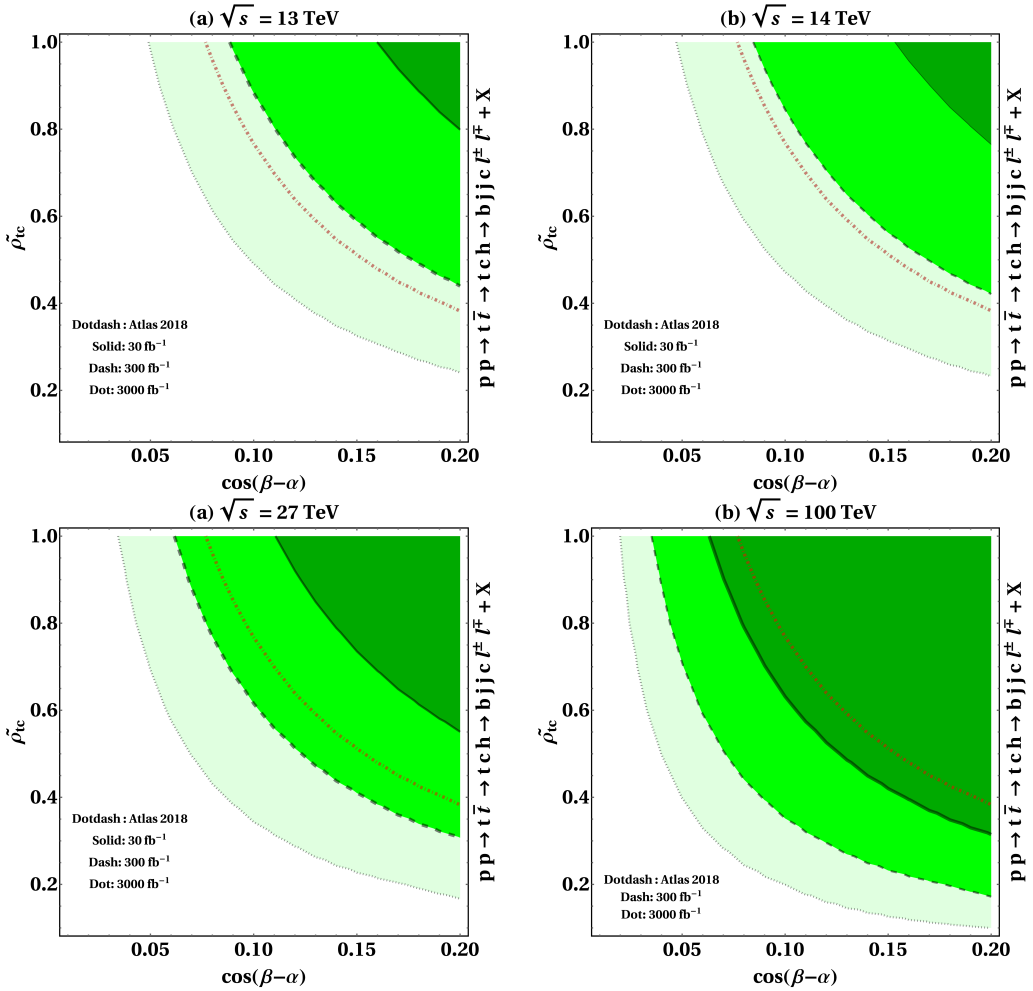

Figure 4.6: The 5σ discovery contours at the LHC in the plane of $[\cos(\beta-\alpha), \tilde{\rho}_{tc}]$ for (a) $\sqrt{s} = 13$ TeV and (b) $\sqrt{s} = 14$ TeV. (c) $\sqrt{s} = 27$ TeV and (d) $\sqrt{s} = 100$ TeV. For $\mathcal{L} = 300 fb^{-1}$ (dash) and $\mathcal{L} = 3000 fb^{-1}$ (dot). Also shown is the ATLAS-2018 limits on $\lambda_{tc} = \tilde{\rho}_{tc} \cos(\beta-\alpha)$ (dotdash) set the shaded region above this curve is excluded at 95% CL.

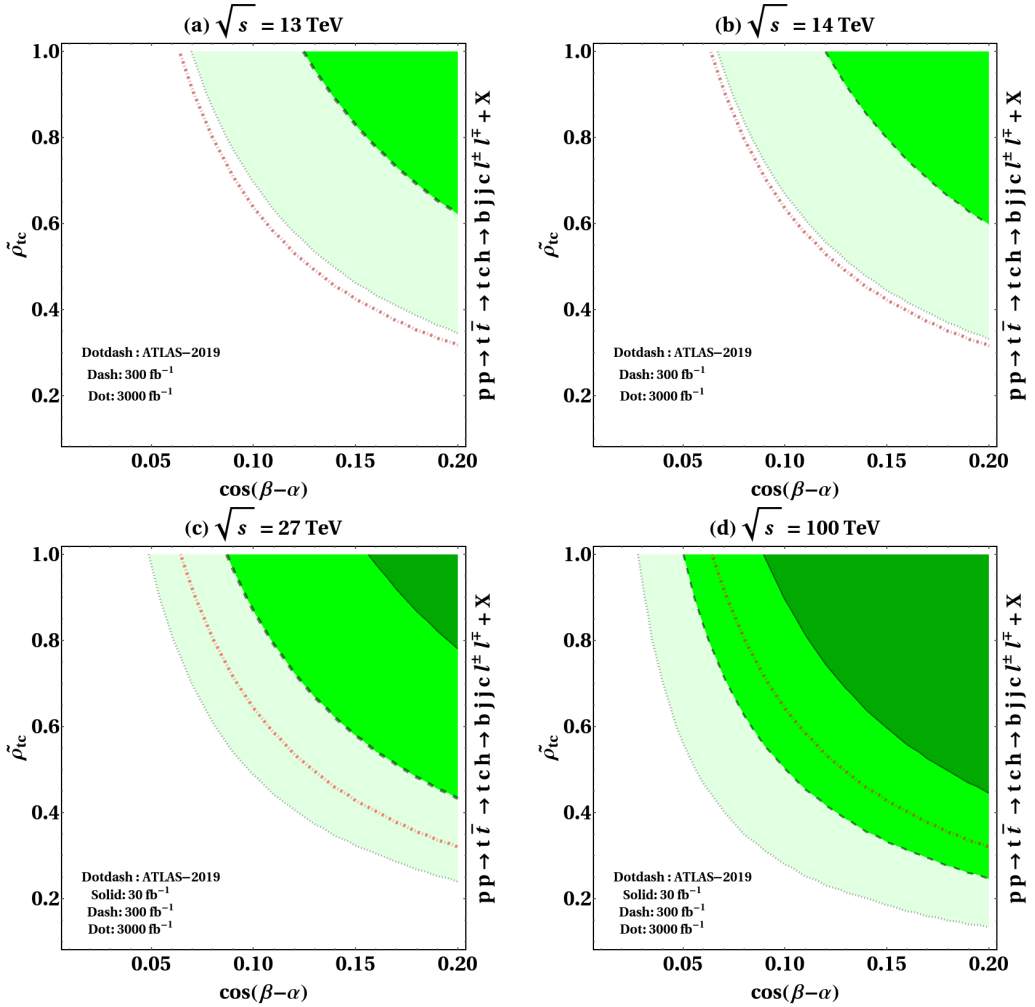

Figure 4.7: The 5σ discovery contours at the LHC in the plane of $[\cos(\beta-\alpha), \tilde{\rho}_{tc}]$ for (a) $\sqrt{s} = 13$ TeV and (b) $\sqrt{s} = 14$ TeV. (c) $\sqrt{s} = 27$ TeV and (d) $\sqrt{s} = 100$ TeV. For $\mathcal{L} = 300 fb^{-1}$ (dash) and $\mathcal{L} = 3000 fb^{-1}$ (dot). Also shown is the new ATLAS-2019 limits. $\lambda_{tc} = \tilde{\rho}_{tc} \cos(\beta - \alpha)$ (dotdash) set the shaded region above this curve is excluded at 95% CL.

4.2 $h^0 \to \tau^+\tau^-$

4.2.1 Higgs Signal

In this section, we present the discovery reach for $pp \to t\bar{t} \to bjj\bar{c}h^0 \to bjj\bar{c}\tau^+\tau^- + X$ with both the τ-lepton decaying leptonically to either an electron or a muon, along with a τ-lepton neutrino and electron/muon neutrino. In our final state, we have two leptons coming from the Higgs with missing transverse energy from the neutrinos. We again require the other top to decay hadronically to a b-jet and two light jets. Which makes our final state consisting of 4 jets (including a b-jet) and two leptons, similar to $h^0 \to WW^*$ case. One major difference here is, since $m_\tau/m_h^0 \ll 1$, the τ-lepton's are highly boosted, which can be used to reconstruct the Higgs invariant mass, as we will see in Sec 4.2.4. Figure. **4.8** shows the Feynman diagram for the process.

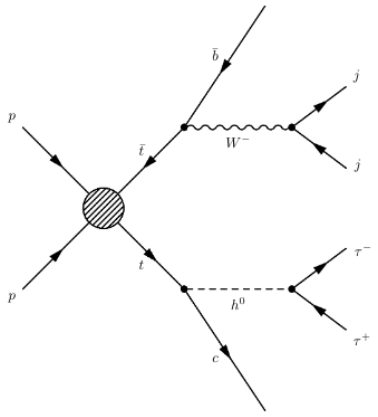

Figure 4.8: Feynman diagram for the signal.

We have calculated the tree level cross-section for the complete signal with Madgraph using CT14LO parton distribution functions [111, 112]. τ-lepton decays are modeled with the taudecay-UFO [140] model. We have generated parton level samples from Madgraph and then passed the sample to Pythia8 [74] and Delphes [75]

to generate events for detector simulations. We have used MLM-matching [141] to match the hadronized jets with the hard partons. As a supplement, we have also performed a naive parton level study to compare this channel with $h^0 \to WW^*$.

We have used the K Factor of ~ 1.8 to scale our tree level cross-section to NNLO, as stated in Sec 4.1.2. In addition, we have checked the tree-level signal cross-section with the narrow width approximation. That is, the cross-section $\sigma(pp \to t\bar{t} \to tch^0 \to bjj\, c\ell^+\ell^-\nu_\tau\bar{\nu}_\tau\nu_\ell\bar{\nu}_\ell + X)$ is calculated as the product of cross-section times branching fractions, following the Table. **3.2** for τ-lepton decay:

$$\sigma(pp \to t\bar{t} \to bjj\bar{t} + X) \times \mathcal{B}(t \to ch^0) \times \mathcal{B}(h^0 \to \tau^+\tau^-)$$
$$\times \mathcal{B}(\tau^+ \to \ell^+\nu_\ell\bar{\nu_\tau}) \times \mathcal{B}(\tau^- \to \ell^-\bar{\nu}_\ell\nu_\tau)\,.$$

We have considered the FCNH signal from both $t\bar{t} \to t\bar{c}h^0 \to bjj\,\bar{c}\ell^+\ell^-\nu_\ell\bar{\nu}_\ell\nu_\tau\bar{\nu_\tau}$, and, $t\bar{t} \to ch^0\bar{t} \to \bar{b}jj\,c\ell^+\ell^-\nu_\ell\bar{\nu}_\ell\nu_\tau\bar{\nu_\tau}$.

We select all those events which consist of one b-jet and three light jets. In addition we require two oppositely charged leptons coming from Higgs decays, along with the neutrinos, which leads to the missing transverse energy. So our FCNH signal leads to the final state of $bjj\,c\ell^+\ell^-\nu_\ell\bar{\nu}_\ell$ or $bjjj\ell^+\ell^- + \not{E}_T$.

4.2.2 The Physics Background

For the above final state our most dominant SM backgrounds comes from,

- $pp \to t\bar{t}jj \to b\ell^+\nu\bar{b}\ell^-\nu jj + X$ $(t\bar{t}jj)$,
- $pp \to b\bar{b}jj\tau^+\tau^- \to b\bar{b}jj\ell^+\ell^-\nu\bar{\nu}\nu_\tau\bar{\nu}_\tau$, $(b\bar{b}jj\tau\tau)$
- $pp \to t\bar{t}W^\pm \to bW^+\bar{b}W^-W^\pm \to b\bar{b}jj\ell^+\ell^-\nu\bar{\nu} + X$ $(t\bar{t}W)$,
- $pp \to t\bar{t}Z \to bW^+\bar{b}W^-Z \to b\bar{b}jj\ell^+\ell^-\nu\bar{\nu} + X$ $(t\bar{t}Z)$, and

- $pp \to b\bar{b}jjW^+W^- \to b\bar{b}jj\ell^+\ell^-\nu\bar{\nu} + X$ (without $t\bar{t}jj$ contribution).

Following Table. **4.2**, we neglect the contribution from the $c\bar{c}jjW^+W^-$, and $jjjjW^+W^-$ backgrounds. For all of the backgrounds, discussed above, we have applied a b-veto to reject events with more than one b jet with $p_T > 20$ GeV and $|\eta| < 4.7$. We evaluated the cross-section for each of the backgrounds using Madgraph, and followed the same procedure to generate events for the detector simulations, as we did for the signal.

We scale our background cross-sections to NNLO using K factor of 1.8 for $t\bar{t}jj$, $b\bar{b}jj\tau\tau$, and $b\bar{b}jjW^+W^-$ same as $t\bar{t}$ for simplicity. For $t\bar{t}W$ and $t\bar{t}Z$, we use 1.64 and 1.46 respectively as the K factors, calculated using Madgraph.

4.2.3 Realistic Acceptance Cuts

We take motivation from the ATLAS studies [142] for $h^0 \to \tau^+\tau^-$, to choose the following basic cuts:

- $P_T(b, j) \geq 20$ GeV
- $|\eta(b)| \leq 4.7$, $|\eta(j)| \leq 2.5$
- Two Opposite sign leptons with $P_T(\ell) \geq 10$ GeV, and $|\eta(\ell)| \leq 2.5$,
- $\not{E}_T \geq 25$ GeV, $\Delta R(\ell\ell, jj, bj, bb, \ell j, \ell b) \geq 0.4$
- $P_T(leading\ell) \geq 20$ GeV
- We also apply a b veto. Rejecting all the events having more than one b-jet with $P_T \geq 20$ GeV and $|\eta| < 4.7$.

4.2.4 Mass Reconstruction

In this section, we present our strategy to reconstruct the Higgs signal coming from $pp \to t\bar{t} \to bjj\bar{t} + X \to bjj\bar{c}h^0 + X \to bjj\bar{c}\tau^+\tau^- \to bjj\bar{c}\ell^+\ell^- + \not{E}_T + X$. Taking motivation from Sec 4.1.4, we reconstruct the top mass for $t \to bW, W \to jj$ by choosing those jets which minimizes $|m_{bjj} - m_t| + |m_{jj} - m_w|$ as j_1 and j_2, and the remaining jet (j_3) is identified as a charm jet. The reconstructed mass distributions for m_{b,j_1,j_2} and m_{j_1,j_2} from parton level events as well from the detector simulations are in Fig. **4.9** for the signal and the most dominant background $t\bar{t}jj$.

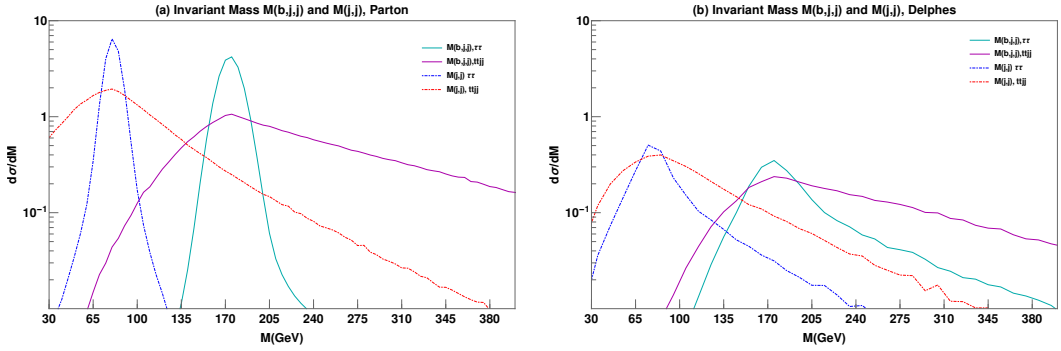

Figure 4.9: Invariant mass distributions for $m_{bj_1j_2}$ and $m_{j_1j_2}$ from parton level events (left) and detector level events (right).

Next is the reconstruction of the FCNH signal, $t \to ch^0 \to c\tau^+\tau^- \to c\ell^+\ell^- + \not{E}_T$. We perform this reconstruction in the following ways:

- (a) Since $m_\tau/m_h \ll 1$, τ-leptons coming from the Higgs decays are highly boosted, as a result, we can make an assumption that all the decay products of τ-lepton, i.e. leptons and neutrinos, are collinear to τ-lepton. This is called the collinear approximation [117]. Under this assumption, we can reconstruct the τ-lepton momentum using the following equation,

$$P_{\tau_i} = \frac{P_{\ell_i}}{x_i}, \tag{4.19}$$

here, i = 1, or 2 and x_i denotes the fraction of the momentum carried by leptons and we require $0 \leq x_i \leq 1$. The remaining fraction of the momentum will be carried by the neutrinos. We can use the missing transverse energy to estimate the momentum fraction, as shown below,

$$\not{E}_x = (1-x_1)P_{\tau_1 x} + (1-x_2)P_{\tau_2 x} \quad \textbf{(4.20)}$$

$$\not{E}_y = (1-x_1)P_{\tau_1 y} + (1-x_2)P_{\tau_2 y}\,. \quad \textbf{(4.21)}$$

Here $\not{E}_x(\not{E}_y)$ is the x-component (y-component) of the missing transverse energy. From Eq 4.19, Eq 4.20 and Eq 4.21, we get

$$x_1 = \frac{(P_{\ell_2 x}P_{\ell_1 y} - P_{\ell_1 x}P_{\ell_2 y})}{(P_{\ell_2 x}P_{\ell_1 y} - P_{\ell_1 x}P_{\ell_2 y} + \not{E}_y P_{\ell_2} x - \not{E}_x P_{\ell_2} y)}) \quad \textbf{(4.22)}$$

$$x_2 = \frac{(P_{\ell_2 x}P_{\ell_1 y} - P_{\ell_1 x}P_{\ell_2 y})}{(P_{\ell_2 x}P_{\ell_1 y} - P_{\ell_1 x}P_{\ell_2 y} - \not{E}_y P_{\ell_1 x} + \not{E}_x P_{\ell_2 y})}\,. \quad \textbf{(4.23)}$$

Using Eq 4.22 and Eq 4.23, we have calculated the τ-lepton momenta and then reconstructed the invariant mass of τ-leptons, i.e., $M_{col}(\tau\tau)$. With the j_3 as a charm-jet, we have also reconstructed the invariant mass of the charm and the τ-leptons $M_{col}(c(j_3)\tau\tau)$. Our distributions are shown in Fig. **4.10**:

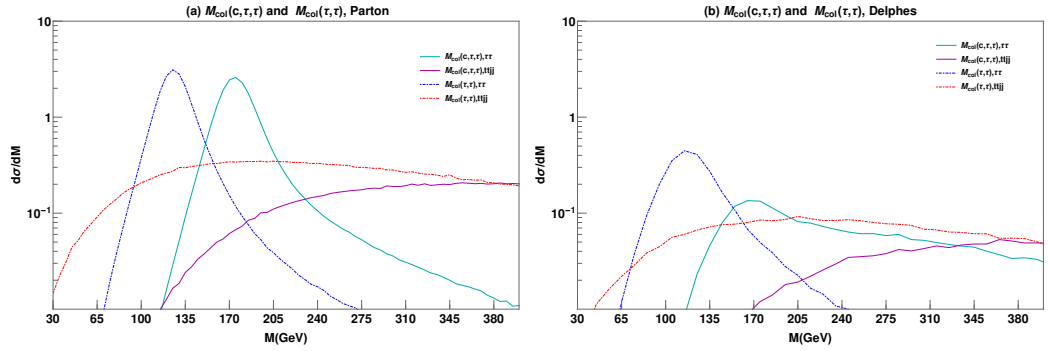

Figure 4.10: Invariant mass distribution for $M_{col}(\tau\tau)$ and $M_{col}(c\tau\tau)$ with the collinear approximation, from parton level events (a) and detector simulations (b).

- (b) We also reconstruct the cluster transverse mass using Eq 4.15 for two leptons + missing transverse energy ($M_T(\ell\ell, \not{E}_T)$) and Eq 4.16 for two leptons + charm jet + missing transverse energy ($M_T(c\ell\ell, \not{E}_T)$). We have shown these distributions again for both the parton level events and detector simulations in Fig. **4.11**.

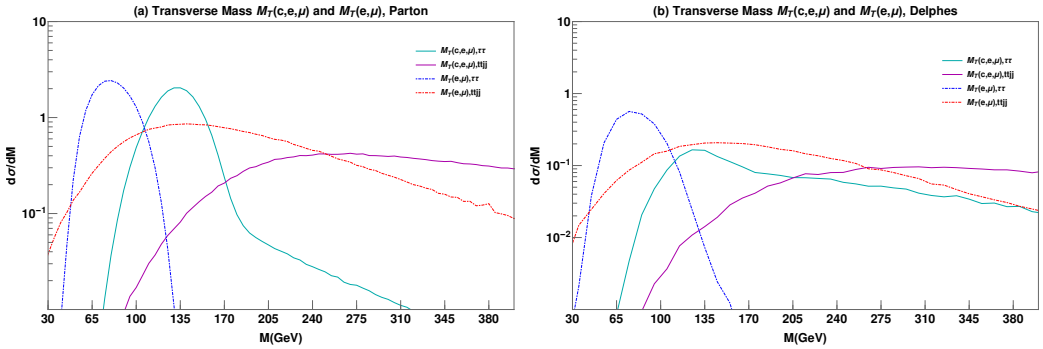

Figure 4.11: Cluster transverse mass distributions from parton level events (a) and detector simulations (b).

- (c) We also reconstruct the invariant mass of the two leptons. It doesn't correspond to any specific resonance, but it carries a unique topology, as shown in Fig. **4.12**:

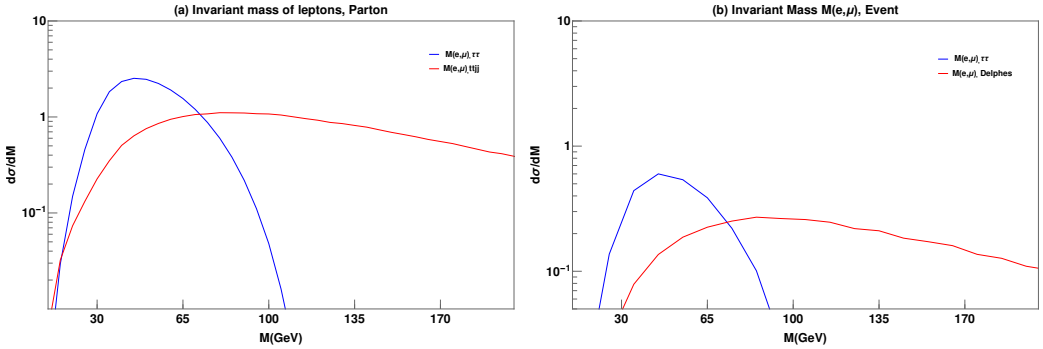

Figure 4.12: Invariant mass of two leptons,from parton level events (a) and detector simulations (b).

In the case of m_{bjj} and m_{jj}, we observe distinct peaks at m_t and m_W, respectively, from both parton level analysis and detector simulation. For $M_{col}(\tau\tau)$ and

$M_{col}(c\tau\tau)$, we observe broad peaks close to m_t and m_h for parton level events. From detector simulations, for $M_{col}(c\tau\tau)$ our curve pretty much flatten after m_t, which is mainly due to higher uncertainty in the charm identification, and the detector resolution effects. We observe similar effects on the transverse mass distribution, $M_T(c\ell\ell, \not{E}_T)$, from detector simulations as well.

The combination of the collinear mass distributions and cluster transverse mass distributions, along with the momentum fraction requirements serves as powerful selection tools in removing the SM backgrounds.

4.2.5 Important Mass Cuts

In addition, to the above reconstructed mass variables, we have also reconstructed another important variable which proves to be quite effective in vetoing the SM background. The energy of the charm quark in the top rest frame has a distinct peak at ~ 41 GeV:

$$E_c^R = \frac{m_t}{2}\left\{1 + \frac{m_c^2}{m_t^2} - \frac{m_h^2}{m_t^2}\right\} \sim 41.43 GeV, \qquad (\mathbf{4.24})$$

as shown Fig. **4.13**.

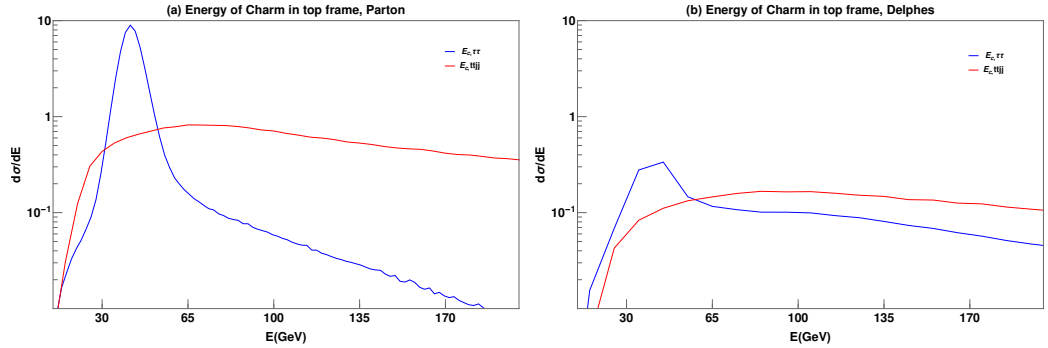

Figure 4.13: Energy of the charm in the top rest frame from parton level events (a) and detector simulations (b).

After careful observation of the mass distributions along with the energy of

charm quark on parton level events, we propose the following cuts:

Variable	Cut
$M(j_1, j_2)$	$\lvert M(j_1, j_2) - m_W \rvert \leq 0.15 \times m_W$
$M(b, j_1, j_2)$	$\lvert M(b, j_1, j_2) - m_t \rvert \leq 0.20 \times m_t$
$M_{col}(\tau\tau)$	$\lvert M_{col}(\tau\tau) \rvert \leq 0.35 \times m_h$
$M_{col}(c\tau\tau)$	$\lvert M_{col}(c\tau\tau) \rvert \leq 0.45 \times m_t$
$M_T(\ell\ell, \not{E}_T)$	40 GeV $\leq M_T(\ell\ell, \not{E}_T) \leq$ 140 GeV
$M_T(c\ell\ell, \not{E}_T)$	80 GeV $\leq M_T(c\ell\ell, \not{E}_T) \leq$ 180 GeV
E_c	32 GeV $\leq E_c \leq$ 52 GeV

Table 4.3: Selection rules for parton level events.

For detector simulations, our mass resolution is not as good as the parton level events because of a more sophisticated detector smearing along with parton showering and hadronization effects, so we relax our mass cuts, as shown in Table. **4.4**.

Variable	Cut
$M(j_1, j_2)$	$\lvert M(j_1, j_2) - m_W \rvert \leq 0.30 \times m_W$
$M(b, j_1, j_2)$	$\lvert M(b, j_1, j_2) - m_t \rvert \leq 0.35 \times m_t$
$M_{col}(\tau\tau)$	$\lvert M_{col}(\tau\tau) \rvert \leq 0.35 \times m_h$
$M_{col}(c\tau\tau)$	$\lvert M_{col}(c\tau\tau) \rvert \leq 0.35 \times m_t$
$M_T(\ell\ell, \not{E}_T)$	40 GeV $\leq M_T(\ell\ell, \not{E}_T) \leq$ 140 GeV
$M_T(c\ell\ell, \not{E}_T)$	80 GeV $\leq M_T(c\ell\ell, \not{E}_T) \leq$ 240 GeV
E_c	20 GeV $\leq E_c \leq$ 60 GeV

Table 4.4: Selection rules for detector simulations.

.

4.2.6 Discovery Potential

Parton Level estimates

After applying all the cuts from Table. **4.3** on parton level events, we show our cross-section estimates for the signal and SM backgrounds at $\sqrt{s} = 13$ TeV in Table. **4.5**. In Fig. **4.14** we present our estimates for statistical significance(N_{SS}) as

Process	Cross-section (fb)
$t\bar{t}$ jj	0.96
$b\bar{b}jj\tau\tau$	0.06
$t\bar{t}W$	0.006
$b\bar{b}jjWW$	4.03×10^{-4}
$t\bar{t}Z$	3.3×10^{-4}
Total	1.03
Signal ($\lambda_{tc} = 0.064$)	0.39

Table 4.5: Cross-section of background and signal in fb after applying cuts defined in Table **4.3**.

a function of $\lambda_{tc}/\sqrt{2}$ from our parton level analysis. We calculate N_{SS} using [143],

$$N_{SS} = \sqrt{2 \times (N_S + N_B)\ln(1 + N_S/N_B) - 2 \times N_S}\,. \qquad (\mathbf{4.25})$$

Here $N_S(N_B)$ are the number of signal (background) events.

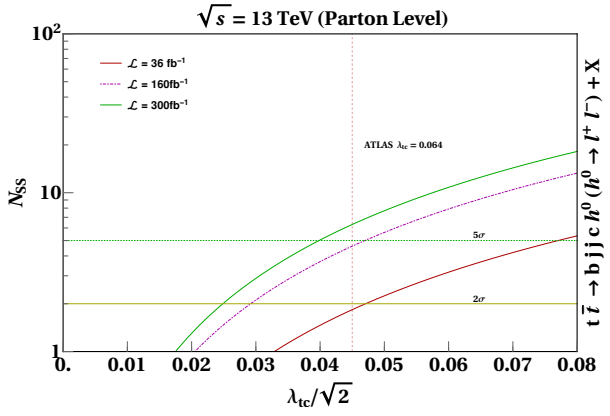

Figure 4.14: N_{SS} as a function of λ_{tc} for parton level events at $\sqrt{s} = 13$ TeV.

Detector Level results

After applying all the cuts described in Table. **4.4**, our cross-section from the detector simulations is shown in Table. **4.6**

Process	Cross-section
$t\bar{t}jj$	~ 1.3
$b\bar{b}jj\tau\tau$	~ 0.07
$t\bar{t}W$	~ 0.008
$t\bar{t}Z$	~ 0.001
$b\bar{b}jjWW$	~ 0.001
Total	~ 1.4
Signal($\rho_{tc} = 0.064$)	~ 0.04

Table 4.6: Cross section of signal and backgrounds in fb.

From Table. **4.6** we estimate the statistical significance using Eq 4.26, for three different integrated luminosities $\mathcal{L} = 36.1$, 160 and 300 fb^{-1}. Our estimates are shown in Table. **4.7**.

Method	$\mathcal{L} = 36.1 fb^{-1}$	$\mathcal{L} = 160 fb^{-1}$	$\mathcal{L} = 300 fb^{-1}$
Cut-based	0.2	0.43	0.58

Table 4.7: Statistical significance for three values of integrated luminosities, with the current limits ATLAS limit on $\lambda_{tc} = 0.064$.

In addition to the above analysis, we have also used a BDT to further improve our statistical significance. Now after applying the cuts, mentioned in the Table. **4.4**, very few of the background events survives from our delphes samples. Which makes it harder for the BDT to train the background samples. This can result in overtraining, which means the prediction of the BDT from the training

sample does not match (to an acceptable uncertainty) with predictions from the testing sample. In order to increase our sample size, we further relax our cuts before training. As a case study we choose two sets of relaxed cuts, for Set-1:

- $M(b, j_1, j_2) \leq 300$ GeV and $M(j_1, j_2) \leq 150$ GeV
- $M(\ell, \ell) \leq 120$ GeV and $M_T(\ell, \ell, \not{E}_T) \leq 180$ GeV
- $M_{col}(\tau, \tau) \leq$300 GeV and $M_{col}(c, \tau, \tau) \leq 400$ GeV
- Ec ≤ 120 GeV.

Set-2 remains the same, except for $M(\ell, \ell) \leq 100$ GeV and $M_{j_1 j_2} \leq 120$ GeV. Table. **4.8** shows the cross-sections after applying the above set of cuts.

Process	Set 1 Cuts	Set 2 Cuts
$t\bar{t}jj$	13.6	9.9
$b\bar{b}jj\tau\tau$	0.51	0.47
$t\bar{t}W$	0.07	0.05
$b\bar{b}jjWW$	0.009	0.007
$t\bar{t}Z$	0.025	0.02
Total	14.3	10.5
Signal ($\lambda_{tc} = 0.064$)	9.5×10^{-2}	9×10^{-2}

Table 4.8: Cross-section for signal and background in fb, after applying Set-1 and Set-2 cuts.

We create two samples after applying the two sets of cuts and then pass them separately for BDT analysis. We have used TMVA [80] (ToolKit for Multivariate Analysis) package inbuilt in ROOT [144] to perform this analysis. The BDT-response from both the sets is shown in Fig. **4.15**.

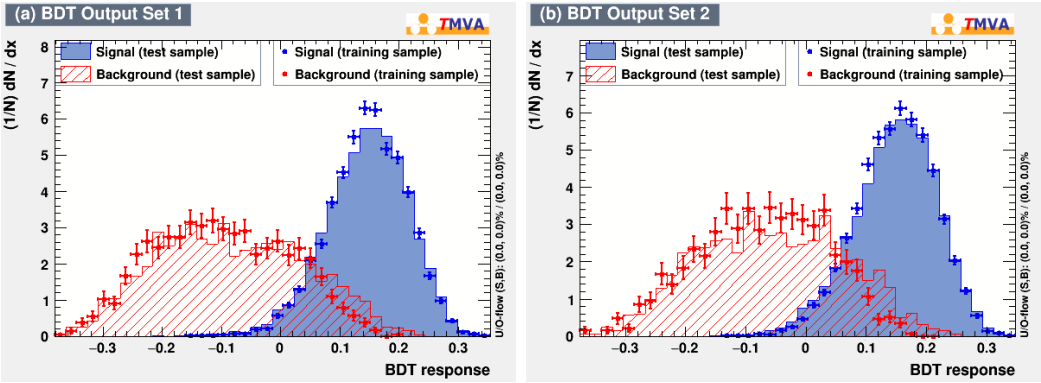

Figure 4.15: BDT response from samples after (a) Set1, and, (b) Set2 pre-selection cuts.

From the above BDT-response for both the sets, we choose a point where we get the best $N_S/\sqrt{(N_S+N_B)}$. The cut-efficiencies for the signal and background from the BDT-response are:

- Set-1: $\epsilon_{signal} = 0.53, \quad \epsilon_{background} = 0.023,$
- Set-2: $\epsilon_{signal} = 0.35, \quad \epsilon_{background} = 0.013.$

Based on the above estimates of cut-efficiencies from the two different BDT runs, in Table. **4.9**, we present the statistical significance of the signal at $\mathcal{L} = 36.1$, 160, and 300 fb^{-1} with $\sqrt{s} = 13$ TeV for λ_{tc} =0.064.

Cuts	$\mathcal{L} = 36.1\ fb^{-1}$	$\mathcal{L}$ =160fb^{-1}	$\mathcal{L} = 300 fb^{-1}$
Set-1	0.51	1.07	1.48
Set-2	0.51	1.05	1.47

Table 4.9: Statistical significance at the current ATLAS limits for λ_{tc} =0.064 from the two samples.

In Fig. **4.16**, we present the statistical significance N_{SS} as a function of $\lambda_{tc}/\sqrt{2}$ with the current ATLAS-limits [88] shown as a vertical red-dashed line.

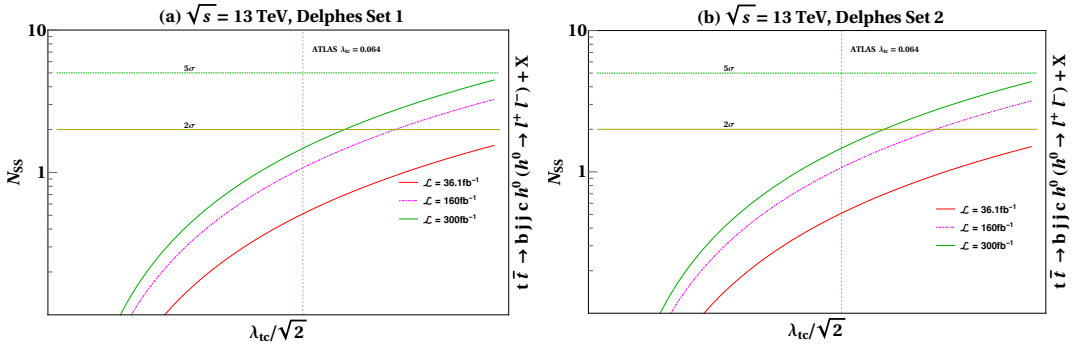

Figure 4.16: Statistical significance estimate as a function of $\lambda_{tc}/\sqrt{2}$ for the two set of pre selection cuts at $\sqrt{s} = 13$ TeV for integrated luminosity $\mathcal{L} = 36.1$, 160 and 300 fb^{-1}, Here red (dashed) vertical line is the current limits set by ATLAS-2019.

In Table. **4.10**, we show the comparison of the statistical significance for the cut-based and BDT.

Method	$\mathcal{L} = 36.1 fb^{-1}$	$\mathcal{L} = 160 fb^{-1}$	$\mathcal{L} = 300 fb^{-1}$
Cut-based	0.2	0.43	0.58
BDT	0.51	1.07	1.48

Table 4.10: Comparison between traditional cut-based vs BDT.

4.3 Combined Estimates at Parton Level

In this section, we present our estimate of the discovery potential for the $t \to ch^0$ Higgs signal by combining $h^0 \to WW^*$ and $h^0 \to \tau^+\tau^-$ at $\sqrt{s}$= 13 TeV for integrated luminosities $\mathcal{L} = 36.1$, 160 and 300 fb^{-1} at parton level. In Table. **4.11**, we present our estimates of the statistical significance for λ_{tc} =0.064,

Process	$\mathcal{L} = 36.1 fb^{-1}$	$\mathcal{L} = 160 fb^{-1}$	$\mathcal{L} = 300 fb^{-1}$
$h^0 \to WW$	0.93	1.96	2.7
$h^0 \to \tau^+\tau^-$	2.2	4.6	6.3
Combined	2.4	5.0	6.85

Table 4.11: Statistical significance for $h^0 \to WW^*$ and $h^0 \to \tau\tau$ at $\sqrt{s} = 13$ TeV for $\lambda_{tc} = 0.064$. We have also shown the combined estimates of both the channels.

In Fig. **4.17**, we present the statistical significance as a function of λ_{tc} at $\mathcal{L} = 160 fb^{-1}$.

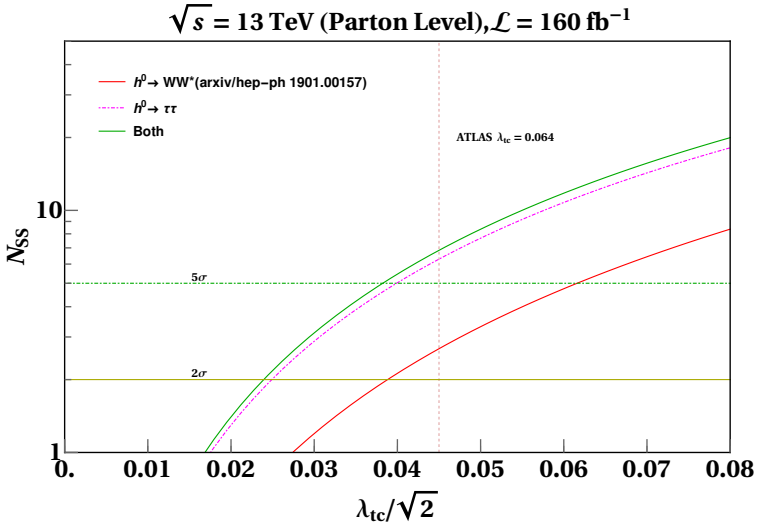

Figure 4.17: Combined estimates of N_{SS} for $t \to ch^0$ decay channel, after including both $h^0 \to \tau^+\tau^-$ and $h^0 \to WW^*$ at parton level.

We see that the $h^0 \to \tau^+\tau^-$ gives a higher statistical significance than the $h^0 \to WW^*$, despite having a lower branching fraction ($\mathcal{B}(h^0 \to WW^*) \sim 21\%$, $\mathcal{B}(h^0 \to \tau\tau) \sim 6\%$). What works in the favor of $h^0 \to \tau^+\tau^-$ channel is:

- (a) Full reconstruction of the invariant Higgs mass from the collinear approximation.

- (b) We can calculate the energy of charm in the top rest frame with the help

of the reconstructed τ-lepton momentum. Which in turn has a very sharp peak at ~ 41.43 GeV for the Higgs signal.

- (c) Momentum fraction requirements, .i.e., $0 \leq x_i \leq 1$.

The above three variables help us to remove a much larger chunk of the SM backgrounds for the $\tau^+\tau^-$ channel in comparison with the WW^*. When we compare Table. **4.2** with Table. **4.5**, it is quite evident that for $h^0 \to \tau\tau$ our total background cross section at $\sqrt{s} = 13$ TeV is about 1 fb, whereas for $h^0 \to WW^*$ it is 15 fb.

Chapter 5

Conclusion and Future Work

The discovery of the Higgs-like scalar at ATLAS and CMS in 2012 completes the SM's particle spectrum. Although the Higgs mechanism, which provides mass to fermions and weak gauge bosons by spontaneously breaking the electroweak symmetry, is still unclear. To understand the Higgs mechanism, we need to know how the Higgs sector interacts with the fermions and gauge bosons. In Chapter 1, we mentioned that the flavor symmetry in the SM is accidental, and the Higgs boson from the SM also respects this flavor symmetry. It is essential to test this flavor symmetry of the SM experimentally and phenomenologically as well. Section 1.1.9 shows that the experimental measurement of the observables $R(D)$ and $R(D^*)$ [44–46] deviates from the SM predictions quite significantly, which means that the SM flavor symmetry is not an exact symmetry of nature. One explanation comes from the gTHDM, with no symmetry to restrict the Higgs couplings to the fermions. As a result, gTHDM can predict the existence of flavor changing neutral Higgs interaction at tree level. In the decoupling limit, the light Higgs boson (h^0) resembles the standard Higgs boson, and is less massive than the top quark; this could make the rare decay $t \to ch^0$ feasible. For the case of leptonic FCNH signal, the decoupling limit could potentially explain the fading signal for $h^0 \to \tau\mu$ at LHC, as this coupling is proportional to $\cos(\beta - \alpha) \to 0$. Where as for the $H^0 \to \tau\mu$, the interaction is proportional to $\sin(\beta - \alpha) \to 1$ and $A^0 \to \tau\mu$ is independent of the mixing angle $(\beta - \alpha)$.

As shown in Chapter 3, we have investigated the prospects of discovering $H^0,\ A^0 \to \tau\mu$ for current and future high energy (HE) and high luminosity (HL) collider at the LHC. With gluon-gluon fusion being the most dominant mode of

production for both the scalar and the pseudoscalar, we have found promising results for LHC with the parameter $\cos(\beta - \alpha) = 0.1$, with $\tilde{\rho_{tc}} = 0.1$ for M_H up to 300 GeV. It should be noted that the $pp \to A^0 \to \tau\mu$ is more promising than the $pp \to H^0 \to \tau\mu$ because of its higher production cross-section and fewer parameters affecting $\phi^0 \to \tau\mu$ decay. Recently CMS [145] performed their first dedicated study towards looking for $pp \to H^0 \to \tau\mu$ with $200 < M_H < 900$ GeV. Although there was no excess in the signal region, their limits on the cross-section, as shown in the Fig. **5.1**, can help us improve our parameter space. This will provide a baseline for future studies.

Now for the FCNH involving quarks (charm and top quarks), as presented in Chapter 4, we investigated the prospects for discovering $t \to ch^0$ decay at the LHC, focusing on the channel where $t\bar{t}$ are pair produced and subsequently decay, one hadronically and the other through the FCNH mode. We have considered two different decay modes for the h^0, namely WW^* and $\tau^+\tau^-$, with the same final states. The primary background for this signal is $t\bar{t}jj$ with both the top quarks decaying leptonically to $t \to b\ell\nu_\ell$. This background involves one b-jet mis-tagged either as a c jet or a light jet. In addition, we have two other light jets, two opposite-charged leptons, and neutrinos, presenting as missing transverse energy. With the help of kinematic information, we have reconstructed important resonances for the signal and removed much of the SM backgrounds.

We have shown two different analyses for $\tau^+\tau^-$, one being a parton level study (similar to WW^*), and the other using detector simulations.

We find that the $h^0 \to \tau^+\tau^-$ performs better than $h^0 \to WW^*$, because of two reasons:

- $m_\tau/m_h \ll 1$, so τ are highly boosted such that the neutrinos, leptons, or j_τ move in the same direction of τ. This allows us to use the collinear

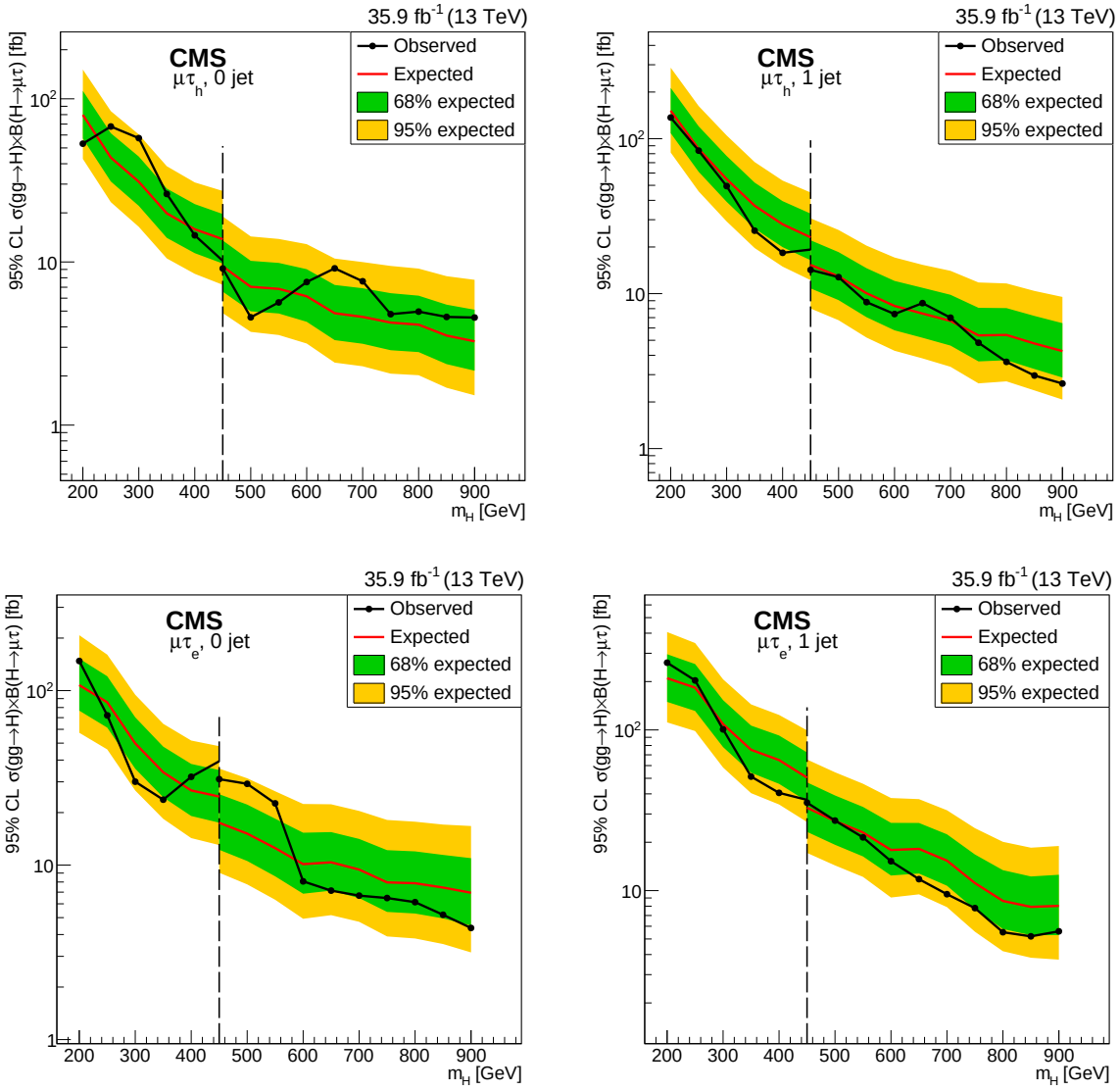

Figure 5.1: The observed and median expected 95% CL upper limits on $\sigma(gg \to H^0) \times (H^0 \to \mu\tau)$, for the $\mu\tau_h$ (upper) and $\mu\tau_e$ (lower) channels, for 0-jet (left) and 1-jet (right) categories. The dashed line shows the transition between the two investigated mass ranges, Sirunyan. et. al (CMS-HIG-18-017).

approximation to reconstruct τ-lepton momentum, and hence invariant Higgs mass.

- With the help of reconstructed τ-lepton, we can also reconstruct the top momentum, in the $t \to ch^0$. We used that to calculate the charm energy in the top rest frame, which, as shown in Fig. **4.13**, has a sharp peak at 41.43 GeV.

With the selection rules defined in Table **4.3** on the above variables, we can reduce the SM backgrounds in the $h^0 \to \tau^+\tau^-$ much more efficiently than $h^0 \to WW^*$, hence making $\tau^+\tau^-$ much more cleaner channel. Based on our analysis, we find that for $h^0 \to WW^*$ at $\sqrt{s} = 14$ TeV, with $\mathcal{L} = 3000 fb^{-1}$, LHC can probe to as low as $\mathcal{B}(t \to ch^0) \simeq 1.17 \times 10^{-3}$,$\lambda_{tc} \simeq 0.069$.
The sensitivity increases with $\sqrt{s} = 27$ TeV and $\sqrt{s} = 100$ TeV, which can reach upto $\mathcal{B}(t \to ch^0) \simeq 6.1 \times 10^{-4}$, $\lambda_{tc} \simeq 0.048$ and $\mathcal{B}(t \to ch^0) \simeq 2 \times 10^{-4}$, $\lambda_{tc} \simeq 0.028$ respectively. Now for $\sqrt{s} = 13$ TeV, with the current limits we cannot find any region with 5σ or better for WW^*. Whereas, including the $\tau^+\tau^-$ channel at parton level, we have shown that we can reach 5σ, even at a $\mathcal{L} = 160 fb^{-1}$. With $\mathcal{L} = 3000 fb^{-1}$ by combining both the channels we can probe λ_{tc} as low as 3.12×10^{-2} and $\mathcal{B}(t \to ch^0) \simeq 2.4 \times 10^{-4}$, a significant improvement to our previous parton level analysis.

A more realistic analysis comes from the detector simulations for $h^0 \to \tau^+\tau^-$, which suggests that we need $\mathcal{L} \simeq 3439 fb^{-1}$ to reach a statistical significance of 5 σ at $\sqrt{s} = 13$ TeV for $\lambda_{tc} = 0.064$. We can reach a statistical significance of about $\sim 4.6\ \sigma$ for $\lambda_{tc} = 0.064$, with $\mathcal{L} = 3000 fb^{-1}$. With the upcoming high energy and high luminosity hadron colliders, more light will be shed on the properties of SM Higgs boson. With new data, we can learn a lot more about the EWSB and FCNH. A more dedicated search for $t \to ch^0$ can perhaps open up doors for more new

physics, and help us to understand more about nature and its underlying flavor structure.

The FCNH signals we have searched in the framework of the gTHDM can provide more insight on the mechanism and the scalar fields responsible for EWSB to generate mass terms for the vector bosons and the fermions. With the $\tau\mu$ channel, we can also prove the existence of the new Higgs scalar, which will point towards an extended Higgs sector with more than one doublet; this means that SM-Higgs doublet is not the only player driving the Higgs mechanism. For the case of $t \to ch^0$, its discovery can link towards the existence of the new sources of CP-violation coming from the Yukawa sector if there is any complex phase associated with the $\tilde{\rho_{tc}}$ coupling. This additional source of CP-violation along with complex ρ_{tt} coupling, which is associated with the production of H^0 and A^0, can potentially explain the matter-antimatter asymmetry of the Universe as discussed in Ref. [64].

References

[1] Tian Yu Cao. *Conceptual developments of 20 century field theories*. Cambridge University Press, Cambridge, 1998.

[2] Paul A.M. Dirac. On the Theory of quantum mechanics. *Proc. Roy. Soc. Lond. A*, A112:661–677, 1926.

[3] Enrico Fermi. On the Quantization of the Monoatomic Ideal Gas. 12 1999.

[4] K.B. Davis, M.-O. Mewes, M.R. Andrews, N.J. van Druten, D.S. Durfee, D.M. Kurn, and W. Ketterle. Bose-Einstein condensation in a gas of sodium atoms. *Phys. Rev. Lett.*, 75:3969–3973, 1995.

[5] Sergey Sukhoruchkin. Analysis of the particle mass spectrum PDG-2016. *PoS*, EPS-HEP2017:746, 2017.

[6] J.J. Thomson. Cathode rays. *Phil. Mag. Ser. 5*, 44:293–316, 1897.

[7] George Johnstone Stoney. Concept of the electron.

[8] Carl D. Anderson and Seth H. Neddermeyer. Cloud Chamber Observations of Cosmic Rays at 4300 Meters Elevation and Near Sea-Level. *Phys. Rev.*, 50:263–271, 1936.

[9] David J Griffiths. *Introduction to elementary particles; 2nd rev. version*. Physics textbook. Wiley, New York, NY, 2008.

[10] Yung-Su Tsai. Decay Correlations of Heavy Leptons in e+ e- —¿ Lepton+ Lepton-. *Phys. Rev. D*, 4:2821, 1971. [Erratum: Phys.Rev.D 13, 771 (1976)].

[11] Martin L. Perl et al. Evidence for Anomalous Lepton Production in e+ - e- Annihilation. *Phys. Rev. Lett.*, 35:1489–1492, 1975.

[12] J. Burmester et al. Anomalous Muon Production in e+ e- Annihilation as Evidence for Heavy Leptons. *Phys. Lett. B*, 68:297, 1977.

[13] Frederick Reines and Clyde L. Cowan. The neutrino. *Nature*, 178:446–449, 1956.

[14] P.A.M. Dirac. A Theory of Electrons and Protons. *Proc. Roy. Soc. Lond. A*, A126(801):360–365, 1930.

[15] Carl D. Anderson. Cosmic-Ray Positive and Negative Electrons. *Phys. Rev.*, 44:406–416, 1933.

[16] R.P. Feynman. Space-time approach to nonrelativistic quantum mechanics. *Rev. Mod. Phys.*, 20:367–387, 1948.

[17] L.P. Horwitz and I. Aharonovich. Neutrino oscillations in Stueckelberg semiclassical relativistic dynamics. *J. Phys. Conf. Ser.*, 437:012021, 2013.

[18] Murray Gell-Mann. A Schematic Model of Baryons and Mesons. *Phys. Lett.*, 8:214–215, 1964.

[19] G. Zweig. *An SU(3) model for strong interaction symmetry and its breaking. Version 2*, pages 22–101. 2 1964.

[20] F. Halzen and Alan D. Martin. *QUARKS AND LEPTONS: AN INTRODUCTORY COURSE IN MODERN PARTICLE PHYSICS*. 1 1984.

[21] J.J. Aubert et al. Experimental Observation of a Heavy Particle J. *Phys. Rev. Lett.*, 33:1404–1406, 1974.

[22] J.E. Augustin et al. Discovery of a Narrow Resonance in e^+e^- Annihilation. *Phys. Rev. Lett.*, 33:1406–1408, 1974.

[23] T.G. Trippe et al. New Particle Searches and Discoveries. A Supplement to the 1976 Edition Review of Particle Properties. *Phys. Lett. B*, 68:1–30, 1977.

[24] S. Abachi et al. Observation of the top quark. *Phys. Rev. Lett.*, 74:2632–2637, 1995.

[25] Max Planck. Ueber das gesetz der energieverteilung im normalspectrum. *Annalen der Physik*, 309(3):553–563, 1901.

[26] Matthew D. Schwartz. *Quantum Field Theory and the Standard Model*. Cambridge University Press, 3 2014.

[27] Albert Einstein. Concerning an heuristic point of view toward the emission and transformation of light. *Annalen Phys.*, 17:132–148, 1905.

[28] M.O. Scully and M. Sargent. The concept of the photon. *Phys. Today*, 25N3:38–47, 1972.

[29] Arthur H. Compton. A Quantum Theory of the Scattering of X-rays by Light Elements. *Phys. Rev.*, 21:483–502, 1923.

[30] Vernon D. Barger and R.J.N. Phillips. *COLLIDER PHYSICS*. 1987.

[31] G. Arnison et al. Experimental Observation of Isolated Large Transverse Energy Electrons with Associated Missing Energy at s**(1/2) = 540-GeV. *Phys. Lett. B*, 122:103–116, 1983.

[32] G. Arnison et al. Experimental Observation of Lepton Pairs of Invariant Mass Around 95-GeV/c**2 at the CERN SPS Collider. *Phys. Lett. B*, 126:398–410, 1983.

[33] Peter W. Higgs. Broken symmetries, massless particles and gauge fields. *Phys. Lett.*, 12:132–133, 1964.

[34] Michael E. Peskin and Daniel V. Schroeder. *An Introduction to quantum field theory*. Addison-Wesley, Reading, USA, 1995.

[35] Luciano Maiani. The GIM Mechanism: origin, predictions and recent uses. In *48th Rencontres de Moriond on Electroweak Interactions and Unified Theories*, pages 3–16, 2013.

[36] G. Dattoli, E. Sabia, and A. Torre. Exponential and Wolfenstein parametrizations of the CKM matrix. *Nuovo Cim. A*, 109:1425–1437, 1996.

[37] D. Abbaneo et al. The CKM matrix and the unitarity triangle. Workshop, CERN, Geneva, Switzerland, 13-16 Feb 2002: Proceedings. 4 2003.

[38] J.A. Aguilar-Saavedra. Top flavor-changing neutral interactions: Theoretical expectations and experimental detection. *Acta Phys. Polon. B*, 35:2695–2710, 2004.

[39] B. Mele, S. Petrarca, and A. Soddu. A New evaluation of the t —¿ cH decay width in the standard model. *Phys. Lett. B*, 435:401–406, 1998.

[40] G. Eilam, J. L. Hewett, and A. Soni. Rare decays of the top quark in the standard and two-higgs-doublet models. *Phys. Rev. D*, 44:1473–1484, Sep 1991.

[41] Marzia Bordone, Gino Isidori, and Andrea Pattori. On the Standard Model predictions for R_K and R_{K^*}. *Eur. Phys. J. C*, 76(8):440, 2016.

[42] Roel Aaij et al. Test of lepton universality using $B^+ \to K^+\ell^+\ell^-$ decays. *Phys. Rev. Lett.*, 113:151601, 2014.

[43] R. Aaij et al. Test of lepton universality with $B^0 \to K^{*0}\ell^+\ell^-$ decays. *JHEP*, 08:055, 2017.

[44] Jon A. Bailey et al. B→Dν form factors at nonzero recoil and —V_{cb}— from 2+1-flavor lattice QCD. *Phys. Rev. D*, 92(3):034506, 2015.

[45] Syuhei Iguro and Kazuhiro Tobe. $R(D^{(*)})$ in a general two Higgs doublet model. *Nucl. Phys. B*, 925:560–606, 2017.

[46] Andreas Crivellin, Christoph Greub, and Ahmet Kokulu. Explaining $B \to D\tau\nu$, $B \to D^*\tau\nu$ and $B \to \tau\nu$ in a 2HDM of type III. *Phys. Rev. D*, 86:054014, 2012.

[47] John F. Gunion and Howard E. Haber. The CP conserving two Higgs doublet model: The Approach to the decoupling limit. *Phys. Rev. D*, 67:075019, 2003.

[48] Wei-Shu Hou, Masaya Kohda, and Tanmoy Modak. Top-assisted di-Higgs boson production motivated by baryogenesis. *Phys. Rev. D*, 99(5):055046, 2019.

[49] Sacha Davidson and Howard E. Haber. Basis-independent methods for the two-Higgs-doublet model. *Phys. Rev. D*, 72:035004, 2005. [Erratum: Phys.Rev.D 72, 099902 (2005)].

[50] Baris Altunkaynak, Wei-Shu Hou, Chung Kao, Masaya Kohda, and Brent McCoy. Flavor Changing Heavy Higgs Interactions at the LHC. *Phys. Lett. B*, 751:135–142, 2015.

[51] E.A. Paschos. Diagonal Neutral Currents. *Phys. Rev. D*, 15:1966, 1977.

[52] G.C. Branco, P.M. Ferreira, L. Lavoura, M.N. Rebelo, Marc Sher, and Joao P. Silva. Theory and phenomenology of two-Higgs-doublet models. *Phys. Rept.*, 516:1–102, 2012.

[53] Syuhei Iguro and Kazuhiro Tobe. $R(D^{(*)})$ in a general two Higgs doublet model. *Nucl. Phys. B*, 925:560–606, 2017.

[54] Search for lepton-flavour-violating decays of the Higgs boson to etau and emu at sqrt(s)=8 TeV. 8 2015.

[55] Search for lepton flavour violating decays of the Higgs boson to $\mu\tau$ and eτ in proton-proton collisions at $\sqrt{s} = 13$ TeV. 5 2017.

[56] Morad Aaboud et al. Search for top-quark decays $t \to Hq$ with 36 fb^{-1} of pp collision data at $\sqrt{s} = 13$ TeV with the ATLAS detector. *JHEP*, 05:123, 2019.

[57] J.P. Lees et al. Evidence for an excess of $\bar{B} \to D^{(*)}\tau^-\bar{\nu}_\tau$ decays. *Phys. Rev. Lett.*, 109:101802, 2012.

[58] A.D. Sakharov. Violation of CP Invariance, C asymmetry, and baryon asymmetry of the universe. *Sov. Phys. Usp.*, 34(5):392–393, 1991.

[59] Patrick Huet and Eric Sather. Electroweak baryogenesis and standard model CP violation. *Phys. Rev. D*, 51:379–394, 1995.

[60] M.B. Gavela, P. Hernandez, J. Orloff, and O. Pene. Standard model CP violation and baryon asymmetry. *Mod. Phys. Lett. A*, 9:795–810, 1994.

[61] J.H. Christenson, J.W. Cronin, V.L. Fitch, and R. Turlay. Evidence for the 2π Decay of the K_2^0 Meson. *Phys. Rev. Lett.*, 13:138–140, 1964.

[62] M. Gell-Mann and A. Pais. Behavior of neutral particles under charge conjugation. *Phys. Rev.*, 97:1387–1389, Mar 1955.

[63] K. Lande, E.T. Booth, J. Impeduglia, L.M. Lederman, and W. Chinowsky. Observation of Long-Lived Neutral V Particles. *Phys. Rev.*, 103:1901–1904, 1956.

[64] Kaori Fuyuto, Wei-Shu Hou, and Eibun Senaha. Electroweak baryogenesis driven by extra top Yukawa couplings. *Phys. Lett. B*, 776:402–406, 2018.

[65] N. Aghanim et al. Planck 2018 results. VI. Cosmological parameters. 7 2018.

[66] Stefan Weinzierl. Introduction to Monte Carlo methods. 6 2000.

[67] Michael B. Cohen, Yin Tat Lee, Cameron Musco, Christopher Musco, Richard Peng, and Aaron Sidford. Uniform sampling for matrix approximation. *CoRR*, abs/1408.5099, 2014.

[68] Jan Wretman Carl-Erik Särndal, Bengt Swensson and. *Model Assisted Survey Sampling*. Springer-Verlag New York, 1992.

[69] Art Owen and Yi Zhou Associate. Safe and effective importance sampling. *Journal of the American Statistical Association*, 95(449):135–143, 2000.

[70] G [Peter Lepage]. A new algorithm for adaptive multidimensional integration. *Journal of Computational Physics*, 27(2):192 – 203, 1978.

[71] Johan Alwall, Michel Herquet, Fabio Maltoni, Olivier Mattelaer, and Tim Stelzer. MadGraph 5 : Going Beyond. *JHEP*, 06:128, 2011.

[72] Kaoru Hagiwara, Junichi Kanzaki, Qiang Li, and Kentarou Mawatari. HELAS and MadGraph/MadEvent with spin-2 particles. *Eur. Phys. J. C*, 56:435–447, 2008.

[73] W. Herr and B. Muratori. Concept of luminosity. In *CERN Accelerator School and DESY Zeuthen: Accelerator Physics*, pages 361–377, 9 2003.

[74] Torbjorn Sjostrand, Stephen Mrenna, and Peter Z. Skands. A Brief Introduction to PYTHIA 8.1. *Comput. Phys. Commun.*, 178:852–867, 2008.

[75] J. de Favereau, C. Delaere, P. Demin, A. Giammanco, V. Lemaître, A. Mertens, and M. Selvaggi. DELPHES 3, A modular framework for fast simulation of a generic collider experiment. *JHEP*, 02:057, 2014.

[76] Morad Aaboud et al. Measurement of the Higgs boson mass in the $H \to ZZ^* \to 4\ell$ and $H \to \gamma\gamma$ channels with $\sqrt{s} = 13$ TeV pp collisions using the ATLAS detector. *Phys. Lett. B*, 784:345–366, 2018.

[77] Chung Kao Dibyashree Sengupta and Xerxes Tata Howard Baer, Vernon Barger. Detecting heavy higgs bosons with charginos in radiatively-driven natural susy at hadron colliders.

[78] Shai Shalev-Shwartz and Shai Ben-David. *Understanding Machine Learning: From Theory to Algorithms*. Cambridge University Press, USA, 2014.

[79] Yann Coadou. Boosted Decision Trees and Applications. *EPJ Web Conf.*, 55:02004, 2013.

[80] Andreas Hocker et al. TMVA - Toolkit for Multivariate Data Analysis. 3 2007.

[81] Wei-Shu Hou, Rishabh Jain, Chung Kao, Masaya Kohda, Brent McCoy, and Amarjit Soni. Flavor Changing Heavy Higgs Interactions with Leptons at Hadron Colliders. *Phys. Lett. B*, 795:371–378, 2019.

[82] Combined measurements of Higgs boson production and decay using up to 80 fb^{-1} of proton–proton collision data at $\sqrt{s} = 13$ TeV collected with the ATLAS experiment. 7 2018.

[83] Combined measurements of the Higgs boson's couplings at $\sqrt{s} = 13$ TeV. 3 2018.

[84] Sheldon L. Glashow and Steven Weinberg. Natural Conservation Laws for Neutral Currents. *Phys. Rev. D*, 15:1958, 1977.

[85] Wei-Shu Hou, Masaya Kohda, and Tanmoy Modak. Probing for extra top Yukawa couplings in light of $t\bar{t}h(125)$ observation. *Phys. Rev. D*, 98(7):075007, 2018.

[86] Morad Aaboud et al. Search for WW/WZ resonance production in $\ell\nu qq$ final states in pp collisions at $\sqrt{s} = 13$ TeV with the ATLAS detector. *JHEP*, 03:042, 2018.

[87] Albert M. Sirunyan et al. Search for the Higgs boson decaying to two muons in proton-proton collisions at $\sqrt{s} = 13$ TeV. *Phys. Rev. Lett.*, 122(2):021801, 2019.

[88] Combined measurements of Higgs boson production and decay using up to 80 fb^{-1} of proton–proton collision data at $\sqrt{s} = 13$ TeV collected with the ATLAS experiment. 3 2019.

[89] D. de Florian et al. Handbook of LHC Higgs Cross Sections: 4. Deciphering the Nature of the Higgs Sector. 10 2016.

[90] Albert M Sirunyan et al. Search for lepton flavour violating decays of the Higgs boson to $\mu\tau$ and eτ in proton-proton collisions at $\sqrt{s} = 13$ TeV. *JHEP*, 06:001, 2018.

[91] Sacha Davidson and Gerald Jean Grenier. Lepton flavour violating Higgs and tau to mu gamma. *Phys. Rev. D*, 81:095016, 2010.

[92] D. Aristizabal Sierra and A. Vicente. Explaining the CMS Higgs flavor violating decay excess. *Phys. Rev. D*, 90(11):115004, 2014.

[93] Ilja Dor˘ sner, Svjetlana Fajfer, Admir Greljo, Jernej F. Kamenik, Nejc Ko˘ snik, and Ivan Ni˘ sandžic. New Physics Models Facing Lepton Flavor Violating Higgs Decays at the Percent Level. *JHEP*, 06:108, 2015.

[94] Yuji Omura, Eibun Senaha, and Kazuhiro Tobe. τ- and μ-physics in a general two Higgs doublet model with $\mu - \tau$ flavor violation. *Phys. Rev. D*, 94(5):055019, 2016.

[95] M. Tanabashi et al. Review of Particle Physics. *Phys. Rev. D*, 98(3):030001, 2018.

[96] D. Chang, W.S. Hou, and Wai-Yee Keung. Two loop contributions of flavor changing neutral Higgs bosons to mu —¿ e gamma. *Phys. Rev. D*, 48:217–224, 1993.

[97] K. Hayasaka et al. New Search for tau -¿ mu gamma and tau -¿ e gamma Decays at Belle. *Phys. Lett. B*, 666:16–22, 2008.

[98] Bernard Aubert et al. Searches for Lepton Flavor Violation in the Decays tau+- —¿ e+- gamma and tau+- —¿ mu+- gamma. *Phys. Rev. Lett.*, 104:021802, 2010.

[99] W. Altmannshofer et al. The Belle II Physics Book. *PTEP*, 2019(12):123C01, 2019. [Erratum: PTEP 2020, 029201 (2020)].

[100] M. Bona et al. Constraints on new physics from the quark mixing unitarity triangle. *Phys. Rev. Lett.*, 97:151803, 2006.

[101] Y. Amhis et al. Averages of b-hadron, c-hadron, and τ-lepton properties as of summer 2016. *Eur. Phys. J. C*, 77(12):895, 2017.

[102] A. Abdesselam et al. Measurement of the inclusive $B \to X_{s+d}\gamma$ branching fraction, photon energy spectrum and HQE parameters. In *38th International Conference on High Energy Physics*, 8 2016.

[103] M. Misiak et al. Updated NNLO QCD predictions for the weak radiative B-meson decays. *Phys. Rev. Lett.*, 114(22):221801, 2015.

[104] Michał Czakon, Paul Fiedler, Tobias Huber, Mikoł aj Misiak, Thomas Schutzmeier, and Matthias Steinhauser. The $(Q_7, Q_{1,2})$ contribution to $\overline{B} \to X_s\gamma$ at $\mathcal{O}\left(\alpha_s^2\right)$. *JHEP*, 04:168, 2015.

[105] Andreas Crivellin, Ahmet Kokulu, and Christoph Greub. Flavor-phenomenology of two-Higgs-doublet models with generic Yukawa structure. *Phys. Rev. D*, 87(9):094031, 2013.

[106] Search for top quark decays twith 36 fb-1$of pp collision data at \sqrt{s}$ = $13 TeV with the ATLAS detector.$ 92018.

[107] Morad Aaboud et al. Search for top quark decays $t \to qH$, with $H \to \gamma\gamma$, in $\sqrt{s} = 13$ TeV pp collisions using the ATLAS detector. *JHEP*, 10:129, 2017.

[108] Georges Aad et al. Search for lepton-flavour-violating decays of the Higgs and Z bosons with the ATLAS detector. *Eur. Phys. J. C*, 77(2):70, 2017.

[109] David Eriksson, Johan Rathsman, and Oscar Stal. 2HDMC: Two-Higgs-Doublet Model Calculator Physics and Manual. *Comput. Phys. Commun.*, 181:189–205, 2010.

[110] Ketevi Adikle Assamagan, Aldo Deandrea, and Pierre-Antoine Delsart. Search for the lepton flavor violating decay A0 / H0 —¿ tau+- mu-+ at hadron colliders. *Phys. Rev. D*, 67:035001, 2003.

[111] Sayipjamal Dulat, Tie-Jiun Hou, Jun Gao, Marco Guzzi, Joey Huston, Pavel Nadolsky, Jon Pumplin, Carl Schmidt, Daniel Stump, and C.P. Yuan. New parton distribution functions from a global analysis of quantum chromodynamics. *Phys. Rev. D*, 93(3):033006, 2016.

[112] Jun Gao, Marco Guzzi, Joey Huston, Hung-Liang Lai, Zhao Li, Pavel Nadolsky, Jon Pumplin, Daniel Stump, and C.-P. Yuan. CT10 next-to-next-to-leading order global analysis of QCD. *Phys. Rev. D*, 89(3):033009, 2014.

[113] Michael Spira. HIGLU: A program for the calculation of the total Higgs production cross-section at hadron colliders via gluon fusion including QCD corrections. 10 1995.

[114] Michael Spira. HIGLU and HDECAY: Programs for Higgs boson production at the LHC and Higgs boson decay widths. *Nucl. Instrum. Meth. A*, 389:357–360, 1997.

[115] Vardan Khachatryan et al. Search for Lepton-Flavour-Violating Decays of the Higgs Boson. *Phys. Lett. B*, 749:337–362, 2015.

[116] John M. Campbell and R.K. Ellis. MCFM for the Tevatron and the LHC. *Nucl. Phys. B Proc. Suppl.*, 205-206:10–15, 2010.

[117] R.Keith Ellis, I. Hinchliffe, M. Soldate, and J.J. van der Bij. Higgs Decay to tau+ tau-: A Possible Signature of Intermediate Mass Higgs Bosons at the SSC. *Nucl. Phys. B*, 297:221–243, 1988.

[118] G. Aad et al. Expected Performance of the ATLAS Experiment - Detector, Trigger and Physics. 1 2009.

[119] M.A. Akl et al. CMS Technical Design Report for the Muon Endcap GEM Upgrade. 6 2015.

[120] Performance assumptions for an upgraded ATLAS detector at a High-Luminosity LHC. 2013.

[121] Vardan Khachatryan et al. Jet energy scale and resolution in the CMS experiment in pp collisions at 8 TeV. *JINST*, 12(02):P02014, 2017.

[122] Measurement of b-tagging Efficiency of c-jets in $t\bar{t}$ Events Using a Likelihood Approach with the ATLAS Detector. 3 2018.

[123] A.M. Sirunyan et al. Identification of heavy-flavour jets with the CMS detector in pp collisions at 13 TeV. *JINST*, 13(05):P05011, 2018.

[124] E.K. Friis. Tau reconstruction and identification at the compact muon solenoid. *Nucl. Phys. B Proc. Suppl.*, 218:256–261, 2011.

[125] Debra Lumb. *Investigation of the discovery potential for supersymmetry in Tau final states and measurement of the Tau identification efficiency for the ATLAS experiment.* PhD thesis, Freiburg U., 12 2010.

[126] Vardan Khachatryan et al. Searches for heavy Higgs bosons in two-Higgs-doublet models and for $t\ß ch$ decay using multilepton and diphoton final states in pp collisions at 8 TeV. *Phys. Rev. D*, 90:112013, 2014.

[127] Nathaniel Craig, Jamison Galloway, and Scott Thomas. Searching for Signs of the Second Higgs Doublet. 5 2013.

[128] Rishabh Jain and Chung Kao. Charming top decays with a flavor changing neutral Higgs boson and WW at hadron colliders. *Phys. Rev. D*, 99(5):055036, 2019.

[129] Michał Czakon, Paul Fiedler, and Alexander Mitov. Total Top-Quark Pair-Production Cross Section at Hadron Colliders Through $O(\alpha_S^4)$. *Phys. Rev. Lett.*, 110:252004, 2013.

[130] Matteo Cacciari, Michal Czakon, Michelangelo Mangano, Alexander Mitov, and Paolo Nason. Top-pair production at hadron colliders with next-to-next-to-leading logarithmic soft-gluon resummation. *Phys. Lett. B*, 710:612–622, 2012.

[131] Wei-Shu Hou. Tree level t —¿ c h or h —¿ t anti-c decays. *Phys. Lett. B*, 296:179–184, 1992.

[132] T.P. Cheng and Marc Sher. Mass Matrix Ansatz and Flavor Nonconservation in Models with Multiple Higgs Doublets. *Phys. Rev. D*, 35:3484, 1987.

[133] Stefan Ask et al. From Lagrangians to Events: Computer Tutorial at the MC4BSM-2012 Workshop. 9 2012.

[134] Michal Czakon and Alexander Mitov. Top++: A Program for the Calculation of the Top-Pair Cross-Section at Hadron Colliders. *Comput. Phys. Commun.*, 185:2930, 2014.

[135] Luca Scodellaro. b tagging in ATLAS and CMS. In *5th Large Hadron Collider Physics Conference*, 9 2017.

[136] Tao Han and Ren-Jie Zhang. Extending the Higgs boson reach at upgraded Tevatron. *Phys. Rev. Lett.*, 82:25–28, 1999.

[137] Search for ttH production in multilepton final states at sqrt(s) = 13 TeV. 3 2016.

[138] William Barletta, Marco Battaglia, Markus Klute, Michelangelo Mangano, Soren Prestemon, Lucio Rossi, and Peter Skands. Working Group Report: Hadron Colliders. In *Community Summer Study 2013: Snowmass on the Mississippi*, 10 2013.

[139] R. Tomás et al. FCC study: parameters and optics for hadron and lepton colliders. *Nucl. Part. Phys. Proc.*, 273-275:149–155, 2016.

[140] Kaoru Hagiwara, Tong Li, Kentarou Mawatari, and Junya Nakamura. TauDecay: a library to simulate polarized tau decays via FeynRules and MadGraph5. *Eur. Phys. J. C*, 73:2489, 2013.

[141] Stefan Hoeche, Frank Krauss, Nils Lavesson, Leif Lonnblad, Michelangelo Mangano, Andreas Schalicke, and Steffen Schumann. Matching parton showers and matrix elements. In *HERA and the LHC: A Workshop on the Implications of HERA for LHC Physics: CERN - DESY Workshop 2004/2005 (Midterm Meeting, CERN, 11-13 October 2004; Final Meeting, DESY, 17-21 January 2005)*, pages 288–289, 2005.

[142] Morad Aaboud et al. Cross-section measurements of the Higgs boson decaying into a pair of τ-leptons in proton-proton collisions at $\sqrt{s} = 13$ TeV with the ATLAS detector. *Phys. Rev. D*, 99:072001, 2019.

[143] Nilanjana Kumar and Stephen P. Martin. Vectorlike Leptons at the Large Hadron Collider. *Phys. Rev. D*, 92(11):115018, 2015.

[144] R. Brun and F. Rademakers. ROOT: An object oriented data analysis framework. *Nucl. Instrum. Meth. A*, 389:81–86, 1997.

[145] Albert M Sirunyan et al. Search for lepton flavour violating decays of a neutral heavy Higgs boson to $\mu\tau$ and eτ in proton-proton collisions at $\sqrt{s} = 13$ TeV. *JHEP*, 03:103, 2020.

[146] Chien-Yi Chen, Qi-Shu Yan, Xiaoran Zhao, Yi-Ming Zhong, and Zhijie Zhao. Probing triple-Higgs productions via 4b2γ decay channel at a 100 TeV hadron collider. *Phys. Rev. D*, 93(1):013007, 2016.

[147] Wolfram Research, Inc. Mathematica, Version 12.1.

Appendix A

The goal of this Appendix is to check our choice of $\lambda_5 \leq 0$. The Higgs potential in the gTHDM is given as [47],

$$\begin{aligned} V_{2HDM} &= m_{11}^2\phi_1^\dagger\phi_1 + m_{22}^2\phi_2^\dagger\phi_2 - (m_{12}^2\phi_1^\dagger\phi_2 + h.c) \\ &+ \frac{1}{2}\lambda_1(\phi_1^\dagger\phi_1)^2 + \frac{1}{2}\lambda_2(\phi_2^\dagger\phi_2)^2 + \lambda_3(\phi_1^\dagger\phi_1)(\phi_2^\dagger\phi_2) + \lambda_4|\phi_1^\dagger\phi_2|^2 \\ &+ \frac{1}{2}\lambda_5(\phi_1^\dagger\phi_2)^2 + \{\lambda_6\phi_1^\dagger\phi_1 + \lambda_7\phi_2^\dagger\phi_2\}\phi_1^\dagger\phi_2 + h.c \end{aligned}$$

The vacuum stability conditions from [47], are

$$\lambda_1, \lambda_2 > 0,\ \lambda_3 > -\sqrt{(\lambda_1\lambda_2)} \tag{A.1}$$

2HDMC [109] uses the above conditions along with

$$\lambda_3 + \lambda_4 - |\lambda_5| > -\sqrt{(\lambda_1\lambda_2)} \tag{A.2}$$

to check the unitarity and vacuum stability of the gTHDM Higgs potential. The above conditions serves as a powerful tools to restrict $\lambda' s$. We have set $\lambda_{6,7} = 0$ for simplicity and λ_{1-4} are set by the mass of the scalar particles and λ_5. We have set $M_H = M_A = M_{H^\pm}$ as a case study. In Fig. A.1 we present all of those points which breaks the unitarity and vacuum stability of the Higgs potential.

For perturbativity stability the Higgs quartic couplings λ_{hhhh} is required to be less than 4π, as required by 2HDMC. In Fig. A.2 we present the allowed regions in the [λ_5 - $\tan\beta$] plane. which suggests that, we should have:

- $\lambda_5 \leq 0$
- $\tan\beta \leq 2$

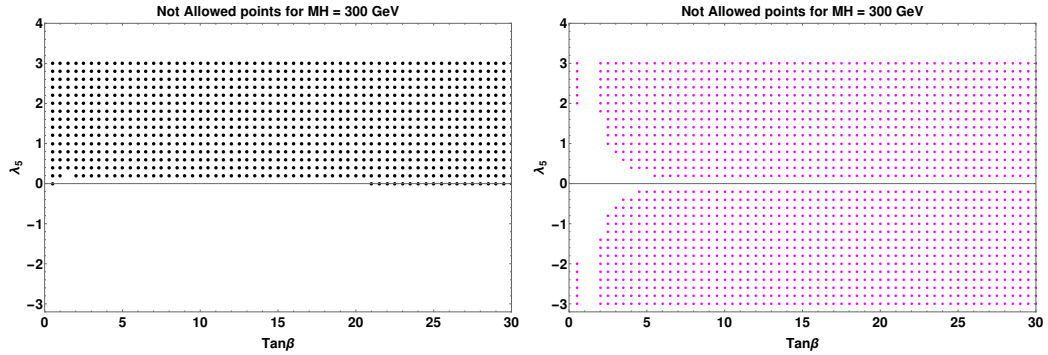

Figure A.1: Points showing the breaking of vacuum stability (left) and perturbativity (right) of the gTHDM Higgs potential in [λ_5 - $\tan\beta$] plane.

So that the Higgs potential follow unitarity, vacuum stability and perturbativity.

We have also checked allowed regions for $M_H = 150$, 250, 300 and 350 GeV.

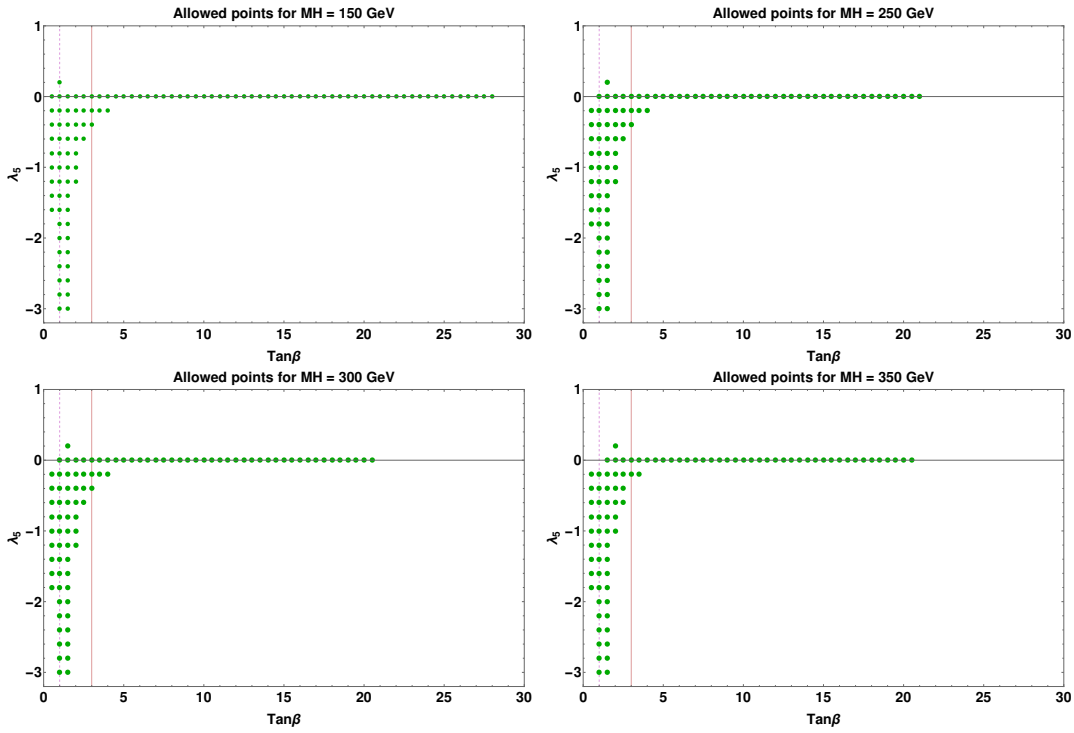

Figure A.2: Allowed region of parameter space for different M_H for $G_{hhhh} < 12.56(4\pi)$

Now following Ref. [146], the quartic coupling for λ_{hhhh} can be as high as 23.64,

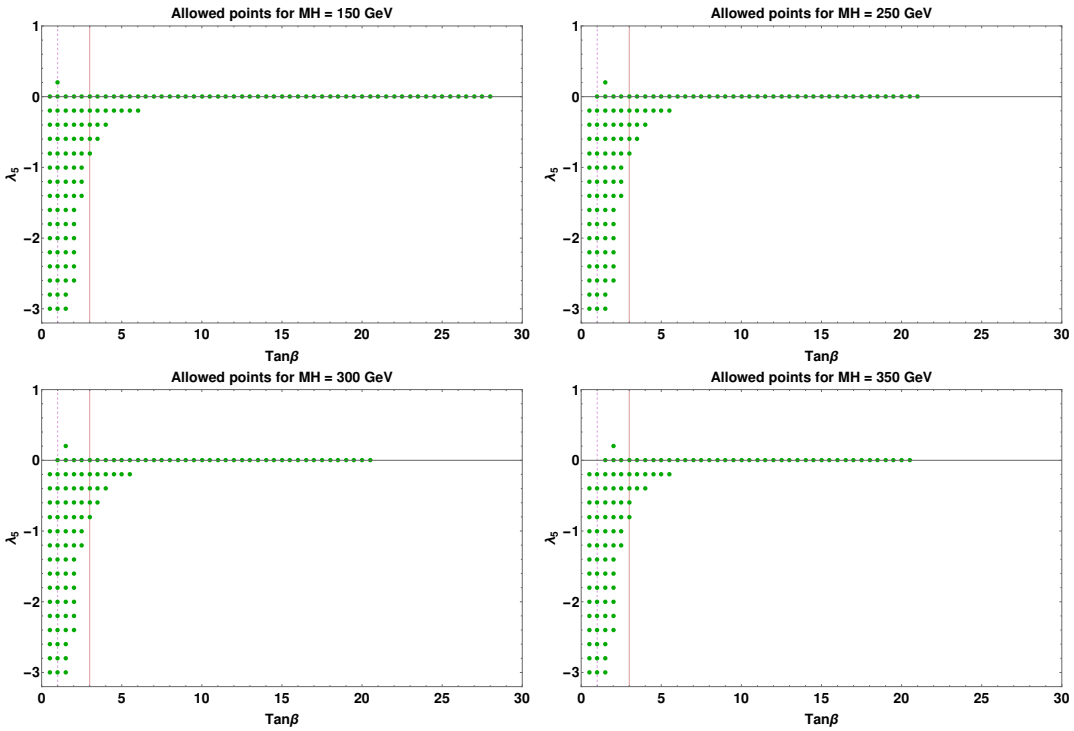

Figure A.3: Allowed region of parameter space for different M_H but for $G_{hhhh} < 23.64$

but this only provides us with a few more points in the allowed region for λ_5, as shown in Fig. A.3, This suggests that, for our parameter space to produce a stable tree level Higgs potential and follow perturbation theory, we should have

- $\lambda_5 \leq 0$
- $\tan\beta \leq 4$

Appendix B

For the $gg \to \phi^0 \to \tau\mu$ we scale our tree level estimates to NNLO by calculating the higher order corrections to $gg \to \phi^0$ using HIGLU [114]. We have included the interference effects from both the top-loop and bottom-loop. In addition, the next to next to leading order QCD corrections as well as radiative corrections are also included. We have calculated the K factors for H^0 and A^0 separately for different energies. In Fig. B.1 we present our estimates for the K-Factors,

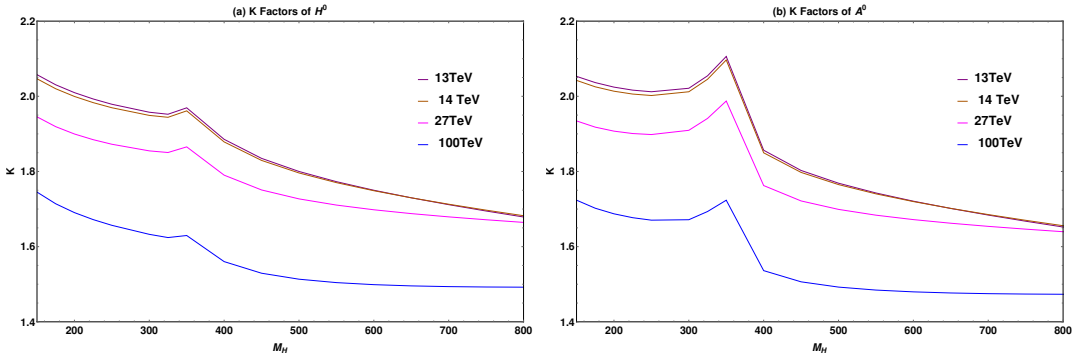

Figure B.1: K-factor as a function of $M^0_\phi\,, \phi^0 = H^0, A^0$ for (a) $pp \to H^0 + X$, and (b) $pp \to A^0 + X$, from $gg \to \phi^0$, with several values of collider energy ($\sqrt{s}$).

To simplifying our MC calculations, we have calculated fitting functions for K-factors calculated above, using Mathematica [147]. Our fitting function takes as an input the center of mass energies $\sqrt{s}$, and the mass of the scalar or pseudoscalar, to calculate the K factor. In Fig B.2, we present the performance of our fit for scalar and pseudoscalar at 13 TeV as a function of masses.

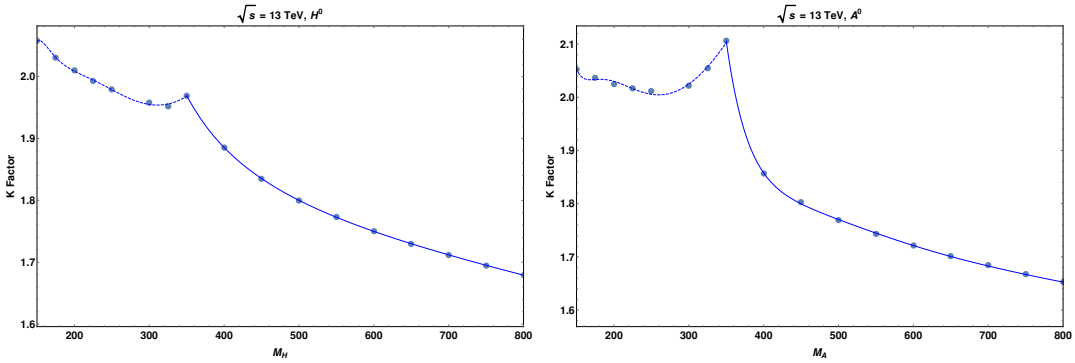

Figure B.2: Goodness of the fitting function for K-factors as function of scalar masses. On the right we present for heavy scalar and left for pseudo scalar